Signature Not Verified

Frank Vollmer

Digitally signed by Frank Vollmer
DN: cn=Frank Vollmer, c=US
Date: 2004.05.04 07:20:40 -07'00'

Resonant Detection of Nano to Microscopic Objects Using Whispering Gallery Modes

A thesis presented to the faculty of

The Rockefeller University

in partial fulfillment of the requirements for

the degree of doctor of Philosophy

by

Frank Vollmer

This work is dedicated to
my parents Dietmar and Silva
and my brother Carsten.

Acknowledgments

I believe in the vast potential of scientific and technological creation by combining unlike academic areas such as physics, chemistry and biology. It is the mind of the individual researcher that has to cross disciplines and conventional boundaries of wisdom to discover new and fertile grounds. During my Ph.D. thesis I was able to experience some of the requirements for such truly interdisciplinary work. Trained as a biochemist I explored part of the technological world of applied physics. It was not necessarily previous knowledge but more importantly a feel of mystery and adventure that overcame my fears and a sense for heuristics that helped me to succeed. This inspiring journey along the interfaces of science was in reality also a social enterprise of continuous interactions with researchers and friends of all areas and origins. The scientific results of this journey are summarized in the following chapters of this thesis. Here I would like to remind the reader of all the help, input and advice I received from many friends and colleagues without whom this thesis would not have been possible.

First of all I thank my advisor Albert. Without his unconventional mindset and feel for interesting ideas it would not have been possible to start, let alone succeed in this interdisciplinary project. Now at the end of my thesis I start to understand why a good advisor does not show his involvement in his student's project. Instead of being in the limelight, Albert guided, criticized and provided support from the back of the stage. It was also Albert who gave me the feel that science is still an adventurous journey just like in the ~ 18^{th} and 19^{th} century when pioneers such as Newton, Rayleigh, Huygens, Faraday and many others set first foot on truly unexplored terrain. I hope I can keep this scientific romanticism as a source for inspiration and creativity for my future endeavors since, in the end, it's emotion that moves people to do fantastic things.

I am equally grateful to Steve Arnold, my Ph.D. co-advisor. It was him who originally thought up the idea of using a microsphere for resonant detection of biomolecules. His lectures, which I attended at the Polytechnic University in Brooklyn, sparked my interest in physics and bio-optics in particular. Steve, you are one of the best teachers I have met and I deeply admire your ability to communicate science in your own fascinating way. We had many great discussions at places where only true New Yorkers would hang out: the Olive Tree Café in the Village, Burger King in Brooklyn or The Red Lion on Bleeker Street. Over the course of this thesis we became good friends and motorcycle buddies. I am very fortunate having been introduced by your former masters student Noel Goddard.

The four years in Albert's lab were intellectually very stimulating and I am grateful for the numerous discussions with students and postdocs: G.V.Shivashankar, Gregoire Bonnet, Roy Bar-Ziv, Vincent Noireaux, Zoher Gueroui, Alexander Feigel, Hanna Salman, Benoit Dubertret, Tsvi Tlusty and all the others. I want to especially thank Dieter Braun for his introduction to and help with the programming language Labview. Many thanks to Hai-Cang Ren who did incredible calculations and explanations concerning the pairing effect which I discovered at the end of my thesis work. Thank you Effie Asvestas for all your unconditional help.

My special thanks go to my good friend Zoher for many, many discussions over coffee. I also received a lot of help from researchers at the Polytechnic University in Brooklyn: many thanks to Iwao Teraoka who introduced me to quantum mechanics and Mazhiar Khoshsima for working with Steve on the theory. I especially thank Mayumi Noto for being such a great collaborator and partner. Without your love and support, especially towards the end of my thesis, it would surely not have been the same.

Many thanks to all the numerous friends I made and the great times we had in New York. Thank you for having been there for me when I most needed help after my motorcycle

accident. Thank you Noel and Perrin, Ben, Oliver, Andrea and everybody else I haven't forgotten.

New York is probably the most fascinating place to be and I am very grateful to Bob Roeder for originally giving me the chance to come to Rockefeller. Thanks also to the members of my thesis committee: Tarun Kapoor, Jim Hudspeth and Bob Austin. Special last thanks to Benjamin Alvarez Borda for correcting the manuscript.

Thesis Committee

Advisor	*Albert Libchaber*
Committee Chair	*Tarun Kapoor*
Committee Members	*Jim Hudspeth*
	Stephen Arnold
External Member	*Robert H. Austin*

Table of Contents

A Introduction

A1 Boundaries of Science

A2 Biodetection of Bottled Light: Perturbation of Photonic Atom Modes

B General Properties and Quality of Resonant Systems

B1 Resonant Systems in the History of Science

B2 The Mass-on-a-Spring

B3 Energy and Quality Factor Q of an Oscillator

B4 Mass Loading of an Oscillator: Resonance Frequency Shift

B5 Photonic Atom Sensor: A Simple Picture

C Experimental Approach: Coupled Microsphere-Waveguide System

C1 Excitation and Detection of Microsphere Resonances

C2 Light Guidance Principles

C2.1 Total Internal Reflection of Light: Snell's Law at a Critical Angle

C2.2 Optical Fibers: Application of Snell's Law.

C2.3 Modes of an Optical Fiber

C2.4 Evanescent Fields: The Imaginary Solutions of Snell's Law

C2.5 Mode Chart of a Flat Waveguide

C3 Distributed Feedback Laser: A Current-tunable Source

C4 Hydrofluoric Acid Erosion of the Optical Fiber

C5 Fabrication of Microsphere Resonators

C6 Experimental Results: Resonances in Air and Water

D Photonic Atom Model

D1 Hydrogen Atom Analogy: A Schrődinger-like Equation

D2 Consequences of Angular Momentum Quantization

E Molecular Perturbation of Microsphere Resonances

E1 Experimental Setup for Molecular Perturbation

E1.1 List of Materials in Chapter E

E2 Bovine Serum Albumin

E3 Silanization of Silica Microspheres
E3.1 Methods and Chemicals in Chapter E3
E4 Adsorption of Bovine Serum Albumin
F First Order Perturbation Theory
F1 Derivation of Perturbation Effect using Photonic Atom Analog
F2 Quantitative Analysis of BSA Frequency Shift
F3 System Calibration: Determination of Thermal Expansion Coefficient of Silica
G Biosensing: Protein Recognition and DNA Hybridization
G1 Molecular Recognition
G2 Biotin-Streptavidin Interaction
G3 Multiplexed Detection of DNA Hybridization: Single Nucleotide Mismatch Discrimination
G4 DNA Immobilization on Hydrogels
G4.1 Materials and Methods used in Chapter G2-4
G5 Two Sphere Multiplexing on a Single Fiber Waveguide
G6 Sequence Specific Detection of DNA Hybridization
G7 Differential Hybridization Measurement: Detection of a Single Nucleotide
G8 Discussion of Chapter G
H Fluorescent Imaging of Whispering Gallery Modes
I Bacterial Detection with Evanescent Fields: Leaving the Rayleigh Limit
I1 Surface Adsorption of *E.coli*
I2 Perturbation Theory for Bacteria and other Large, Biological Objects.
I3 Material and Methods in Chapter I
I4 Q-Spoiling with Bacterial Adsorption
J Pairing Effect with Dielectric Nanospheres
J1 Pairing Effect
J2 Material and Methods in Chapter J
K Comparison with Existing, Label-free Biosensing Techniques
L References

List of Symbols and Abbreviations

a	Sphere radius	B5
APD	Avalanche Photodiode	C3
APTES	Aminopropyltriethoxysilane	E3
BSA	Bovine Serum Albumin	E2
c	Speed of light	C1
C	Coupling constant in pairing effect	J1
D	Dalton	G1
DAQ	Data acquisition	E1
DFB	Distributed feedback laser	C3
DMF	Dimethylformamide	E3
E.Coli	Escherichia Coli	A1
Eq	Equation	B2
F	Force	B2
h	Planck constant	C2.2
HF	Hydrofluoric acid	C1
IR	Infrared	C3
k	Spring constant	B2
kD	Kilo-Dalton	E2
m	Mass	B2
n	Refractive index	C1
NA	Numerical aperture	E1
PBS	Phosphate buffered saline	E4
PIN	pn-junction design	C3
Q	Quality factor	B3
R	Sphere radius	F1
RT	Room temperature	E3
smf	Single mode fiber	C2.5

SNP	Single nucleotide polymorphism	G7
SPR	Surface plasmon resonance	A2
t	Layer thickness	B5
TE	Transverse electric mode	C2.5
TIR	Total Internal Reflection	C1
TM	Transverse magnetic mode	C2.5
TTL	Transistor transistor logic	E1
WDM	Wavelength division multiplexing	C1
WGM	Whispering gallery mode	A2
x	Amplitude	B2
γ	Damping coefficient	B2
λ	Wavelength	B5
Ψ	Wavefunction	D1
ω	Frequency (angular)	B2

List of Figures and Tables

Table A1.1	Optical Methods used to study biological systems with molecular resolution.
Figure A2.1	Residents of Schilda carrying bagged light into their newly constructed town hall
Figure A2.2	Ray optics (left) and wave optics (right) interpretation of a light ray orbiting inside a glass microsphere due to total internal reflection at the sphere boundary.
Figure B1.1	Illustration of the pendulum clock designed by Christiaan Huygens.
Figure B2.1	Mass on a spring.
Figure B2.2	Amplitude response of a damped mass-on-a-spring system.
Table B3.1	Quality factors in biological and physical resonant systems.
Figure B4.1	Mass loading on a mass-on-a-spring system.
Figure B4.2	Resonance frequency shift of a mass-on-a-spring system.
Figure B5.1	Increase of the effective microsphere radius by an additional molecular layer.
Figure C1.1	Minimal setup consisting of source, fiber, microsphere and detector.
Figure C2.1.1	Refraction and reflection of light at an air-water interface.
Figure C2.1.2	Early observation of total internal reflection described by Witelo
Figure C2.2.1	Schematics of light propagation through a typical optical fiber.
Figure C2.3.1	One translational period of a light ray launched in an optical fiber.
Figure C2.4.1	Light refraction at a boundary - the imaginary solution.
Figure C2.5.1	TIR of light at a boundary: electromagnetic field and wavevector.
Figure C2.5.2	Mode chart of a slab waveguide.
Figure C2.5.3	Evanescent field penetration depth of a flat waveguide.
Figure C3.1	Schematic of a laser cavity. Gain spectrum, resonances and output.
Figure C3.2	Setup to determine the tuning coefficient of a current-tunable laser diode.
Figure C3.3	Data showing current-tunability of the DFB laser diode used throughout this thesis.
Figure C4.1	Setup for hydrofluoric acid erosion of the optical fiber.
Figure C4.2	Hydrofluoric acid erosion of a smf-28 single mode optical fiber.
Figure C4.3	Mode chart and evanescent field decay length of flat waveguide in air.

Figure C5.1 Fabrication of microsphere resonator by melting of an optical fiber.
Figure C6.1 Experiment in air: microsphere-fiber coupling.
Figure C6.2 Microsphere resonance dip in air.
Figure C6.3 Microsphere transmission spectrum in water.
Figure D1.1 Analogy between photonic atom and Bohr atom: effective potential.
Table D1.1 Summary of mathematical analogy between photonic atom and Bohr atom.
Figure D2.1 Quantization of angular momentum in photonic atom.
Figure D2.2 L_z component of the angular momentum.
Figure D2.3 Legendre polynomial to describe prolate resonator shape.
Figure D2.4 Equatorial and polar diameters in prolate microsphere.
Figure D2.5 Radii associated with tilted light orbit in a prolate microsphere.
Figure D2.6 Image of fabricated, prolate microsphere resonator.
Figure E1.1 Setup for molecular perturbation of microsphere resonances.
Figure E1.2 Data acquisition with Labview. Flow chart schematic.
Figure E2.1 Crystal structure of bovine serum albumin.
Figure E3.1 Experimental setup for vapor phase silanization.
Figure E3.2 Surface chemistry of aminosilanization.
Figure E4.1 BSA adsorption causes red-shift of a microsphere-resonance wavelength.
Figure E4.2 Langmuir-like adsorption isotherm of a BSA monolayer.
Figure E4.3 Scatchard plot of BSA adsorption data indicates cooperativity.
Table F2.1 Experimentally determined BSA data (surface density, layer thickness, % coverage).
Figure F2.1 Artistic image of a dense BSA monolayer
Figure F2.2 Microsphere size dependence of BSA monolayer shift
Figure G1.1 DNA: chemical structure
Figure G2.1 Streptavidin-Biotin Interaction
Figure G2.2 Experimental data: specific streptavidin binding to biotinylated BSA.
Figure G4.1 DNA immobilization using a dextran hydrogel
Figure G4.2 Surface chemistry: physisorption of a dextran hydrogel using the hanging drop method
Figure G5.1 Sample cell for two microspheres

Figure G5.2 Transmission spectrum for two microspheres coupled to the same waveguide
Figure G6.1 Schematic of experiment for sequence specific DNA detection using two microspheres
Figure G6.2 Microsphere specific DNA hybridization
Figure G7.1 Experimental identification of a single nucleotide
Figure G7.2 Optimal salt concentration for single nucleotide detection
Figure H1.1 Fluorescent image of two microspheres coupled to the same optical fiber
Table H1.1 Materials used in chapter H.
Figure H1.2 Fluorescent image collection of various light orbits.
Table I.1 Biophysical properties of *E.coli.*
Figure I.1 Size chart of molecule, bacteria and wavelength.
Figure I.2 *E.coli* immersed in the evanescent field of a microsphere resonance.
Figure I1.1 Microsphere-surface adsorbed *E.coli.*
Figure I1.2 Polarization of a dielectric sphere (Purcell, 1985).
Figure I1.3 Wavelength shift and linewidth broadening after *E.coli* adsorption.
Figure I2.1 Form factor for correction of wavelength shift caused by large objects.
Figure I2.2 3D plot of wavelength shift as a function of surface density and particle size.
Figure I2.3 Experimental data: wavelength shift due to *E.coli* adsorption
Figure I2.4 Predicted wavelength shift (with evanescent field correction) as function of particle volume.
Figure I2.5 Wavelength shift predicted by theory with and without evanescent field correction.
Figure I4.1 Experimental data of *E.coli* linewidth broadening.
Figure J1.1 Pairing effect of 210 nm diameter nanospheres.
Figure J1.2 Phenomenological fit of pairing effect.
Figure J1.3 Linewidth spoiling due to nanospheres.

List of Publications

This thesis is a review of the author's work in the field of high-Q resonant sensing. It consists of a scholarly introduction and review of the subject. The work presented in this thesis has appeared in the following journal articles, conference presentations and non-refereed publications.

Journal articles

- **Vollmer F.,** Arnold S., Braun D., Teraoka I., Libchaber A., "Multiplexed DNA Quantification by Spectroscopic Shift of Two Microsphere Cavities", BIOPHYSICAL JOURNAL (85) 3: 1974-9 SEP 2003

- Teraoka I., Arnold S., **Vollmer F.**, "Perturbation Approach to Shift of Whispering-Gallery Modes in Microspheres by Protein Adsorption", JOURNAL OF THE OPTICAL SOCIETY OF AMERICA B 20 (9): 1937-1946 SEP 2003

- Arnold S., Khoshsima M., Teraoka I., Holler S., **Vollmer F**., "Shift of Whispering-Gallery Modes in Microspheres by Protein Adsorption", OPTICS LETTERS 28 (4): 272-274 FEB 15 2003

- **Vollmer F**., Braun D., Libchaber A., Khoshsima M., Teraoka I., Arnold S., "Protein Detection by Optical shift of a Resonant Microcavity", APPLIED PHYSICS LETTERS 80 (21): 4057-4059 MAY 27 2002

Journal articles in preparation

- **Vollmer F.**, Ren H.-C., Arnold S., Libchaber A., "Optical Pairing of Mie Particles Perturbing a Whispering Gallery Mode". To be submitted to PHYSICAL REVIEW LETTERS ~May 2004

- **Vollmer F.**, Ren, H.-C., Arnold, S., Libchaber A., "Detection of Bacteria and Viruses using a Whispering Gallery Mode Biosensor". To be submitted to BIOPHYSICAL JOURNAL ~May 2004

Non-refereed articles

- Arnold, S. Noto, M., **Vollmer, F.** "Consequences of Extreme Photon Confinements in Micro-Cavities: I. Ultra-Sensitive Detection of Perturbations by Bio-Molecules", PROCEEDINGS OF THE INTERNATIONAL SCHOOL OF ATOMIC AND MOLECULAR SPECTROSCOPY, Erice, Italy (in press 2004)

- "Silica Microspheres enable sensitive DNA Detection", BIOPHOTONICS INTERNATIONAL, October Issue, 2003 (Research News Article)

- "Whisper Detection of Proteins" Research Highlight NATURE PHYSICS PORTAL, May 2002

Conference papers

- **Vollmer F.**, Arnold S., Teraoka I., Libchaber A. "Whispering Gallery Mode Biosensor", Technical Digest 16th International Conference on Optical Fiber Sensors October 2003, Nara, Japan

- **Vollmer F.**, Arnold S, Braun D, et al. "DNA Detection from Shift of Whispering Gallery Modes in Microspheres" BIOPHYS J 84 (2): 295A-295A Part 2 Suppl. S FEB 2003, Annual Biophysical Society Meeting San Antonio, TX

- **Vollmer F.**, Arnold S., Libchaber A., "Novel, Fiber-optic Biosensor based on Morphology Dependent Resonances in Dielectric Micro-spheres", BIOPHYSICAL JOURNAL 82 (1): 789 Part 2 JAN 2002, Annual Biophysical Society Meeting San Francisco, CA

Patents

- Arnold S., Teraoka I., **Vollmer F.**, "Enhancing the Sensitivity of a Microsphere Sensor Using a Shift of Whispering Gallery Modes in the Microsphere Caused by Adsorption of target Entities" Reg. No. 36,242 (Poly-46/PROV) application submitted in October 2002

Abstract

A micron sized glass sphere is able to confine light to its interior volume. The trapped light describes an orbital trajectory circumnavigating just below the microsphere surface. Whenever the light ray tries to escape it is sent back on its circular path by total internal reflection. The light orbit closes in on itself several thousand times and thus creates an optical resonance. The unprecedented narrow linewidth of such a microsphere resonance (Q factors of up to 3×10^9) allows precise measurement of its frequency. Dielectric microspheres of very high Q are thus the ideal choice for a resonant molecular sensor.

Although the resonance is stealth, an evanescent field extends from the microsphere surface the distance of a wavelength into the surrounding medium. This thesis demonstrates how label-free molecules binding to the microsphere surface perturb the optical resonance by interaction with this evanescent field. The effect is demonstrated by surface adsorption of a protein (serum albumin). The general use as a biosensor is shown by specific detection of streptavidin binding to biotin. A first order perturbation theory describing the linear response of the sensor is presented. Molecular perturbation leads to a wavelength shift that can be measured with such high precision that single molecule detection seems theoretically possible. The experimental approach is extended to the multiplexed measurement of DNA hybridization using two microsphere resonators. This differential measurement allows the detection of a single nucleotide mismatch with a high signal to noise ratio.

The effect of larger Mie particles such as bacteria and polystytrene nanospheres perturbing the cavity resonance is examined experimentally and theoretically. For such larger objects it is necessary to include the decay length of the evanescent field in the theoretical analysis. The Q spoiling which occurs for such large Mie particles is described by an analytic formula. Furthermore, a pairing effect is observed for polystyrene nanospheres with diameters of ~ a quarter wavelength polarized in the evanescent field of the microsphere resonance. A novel mechanism might be involved since the coupling cannot be explained by simple dipole-dipole interactions.

A Introduction

A1 - Boundaries of Science

In search of untouched, fertile scientific grounds the trained eyes of physicists and engineers, looking beyond the traditional boundaries of their trade, have recently been exposed to the molecular nature of the biological world.

This fresh look, created at the crossing of unlike scientific areas in many interdisciplinary initiatives, is leading to the dawn of new scientific areas. One new field that has already set root is based on the ability of trained physicists and similar minds to dissect a complex system into its functional units connected by fundamental rules.

Biological systems are placed in the crown of the tree of complexity. This evolutionary diversity that exudes the beauty of life on our planet humbles researchers of all shades. For some time now, biologist have studied and catalogued the elementary functional units forming the complex biological world of organism and cell, giving them familiar names such as enzymes, molecular motors, membranes, DNA *etc*.

Only recently, fearless pioneers, not only biologists but increasingly also those trained in other scientific areas, set out to study complex biological components on the molecular level by utilizing the experimental and mental tools of applied physics, optics, computer science and other scientific disciplines. These endeavors inspire a modern field I call biological nanoscience. On the broad scale, biological nanoscience comprises areas such as single molecule research, electrophysiology, crystallography and biomaterial science. It also extends, however, to the boundary of biology and nanotechnology. It is one well known goal of nanotechnology to create and use molecular machines. In the special case of biological nanoscience there are the *natural* occurring molecular machines - designed by evolution over the time course of billions of years - that will be studied and used in modern technological devices.

This PhD thesis was created at the boundary of biology, nanotechnology and physics. In this case, however, it is the biochemist who believed that the cracks between biology, physics and technology lead to new worlds full of experimental treasures, adventures and brave new insights.

The aim of this thesis was inspired by the conviction that if biological material is ever to be utilized in nanotechnological devices of the future we first have to develop tools which allow us to manipulate and understand the properties of polymerases, surface self-assemblies and molecular motors on the nano – or single molecule level. Only the development of novel tools of molecular nanomanipulation will allow us to study these rules governing the nanoscopic, elementary world of biology. Once the fundamental rules are dissected, we can set out to re-engineer biorobotic devices (i.e. artificial bacteria, cells) with animated abilities such as self-replication, self-repair and self-improvement. Maybe one day we can design the ultimate nanodevice, a nano-assembler, which will directly utilize (genetic?) information to create any nanomachine of interest. In this respect it is comforting to know that an organism as complex as Escherichia Coli (*E .coli*) is built by self-replication from information which can be stored on a rather outdated, conventional floppy drive. This information content of a bacteria such as *E .coli*, however, is *naturally* not stored in bits and bites but rather in chemical form. For the special purpose of information storage, maintenance and manipulation nature has invented the DNA molecule. It is a long polymer made of a string of more than one million nucleic acid 'bases' in the case of *E. coli*.

Up to today, molecular biologists mostly studied biomolecules such as DNA using bulk properties of such molecules. When manipulation of a single molecule was needed they turned to the living bacteria or cell to help them manipulate e.g. a single DNA plasmid in cloning experiments. Thus far, only a few human tools exist that can reach the exquisite sensitivity to detect and/or manipulate a non-modified single biomolecule such as one DNA polymer. The optical tweezer is probably the most well known tool of single molecule manipulation – and even in this case it is necessary to tag the biomolecule with

a ‘handle’: typically a one micrometer diameter polystyrene-ball onto which the tweezer of focused light can grab, pull and push.

The proven power of photons (light) for detection and manipulation of single, nanometer sized biomolecules (i.e., optical tweezer and other examples listed in table 1) were the inspiration that made me decide to extend the limited nanoscientist’s toolbox for biodetection, manipulation and creation. My goal was to develop an optical detection system with highest sensitivity for molecular events such as biorecognition, DNA hybridization and enzymatic activities such as transcription. Guided from what I had learned from my own optical tweezer experiments I started to look for other optical, high sensitivity systems studied in areas usually unknown to the freshly minted biochemist such as microparticle photophysics (Arnold, 2001). I was hoping to find a novel optical system, which ultimately would allow the resolution of a single, unlabeled molecule. The following thesis recapitulates this path of discovery, creation and use of a novel biosensor which derives its sensitivity from optical resonances excited in micrometer sized glass spheres.

The first three chapters of this thesis are a basic introduction to my research. They are written in a style found in textbooks in the hope, that scientists and non-scientists from diverse areas might be intrigued by this work. I want to apologize to the reader who is already more familiar with this area of science, he might start reading Chapter D.

OPTICAL METHOD	EXAMPLE OF BIOLOGICAL SYSTEMS STUDIED
Optical Tweezer	Biopolymers (DNA, Protein), polymerases. Detection as well as manipulation.
Fluorescence Total Internal Reflection Microscopy	DNA, polymerases, microtubules
Fluorescence Correlation Spectroscopy	DNA hairpins.
Confocal Microscopy	Biomolecules such as DNA, microtubules, etc.
Scanning Near-Field Optical Microscopy	DNA, DNA binding proteins

Table A1.1: Optical Methods used to study biological systems with molecular resolution.

A2 - Biodetection with Bottled Light: Perturbation of Photonic Atom Modes

Researchers in the field of microparticle photophysics have long known the *most* sensitive optical system available: bottled light. To some it might come as a surprise that it is possible at all to bend a beam of light such that it can be trapped inside a transparent spherical object like a micrometer sized glass bead. This might sound like something from fiction literature such as the Swiss-German fairy tale of the "Schildbuerger". In order to illuminate their town hall, which unfortunately was rather foolishly designed without windows, the people of Shilda believed that they could trap light in bags, buckets and cans (fig. A2.1; Kaestner, 2004).

Figure A2.1: Residents of Schilda (called "Schildbuerger") carrying light into their newly constructed town hall which unfortunately lacked any kind of window. (From Kaestner, 2004).

A glass microsphere, however, is indeed able to confine light to its interior volume. Once a light ray is launched inside the microsphere, the trapped light describes an orbital trajectory circumnavigating just below the microsphere surface. Whenever the light ray tries to escape from the microsphere, it is sent back on its circular path by total internal reflection at the boundary of the sphere (Ching, 1996; Fig.A2.2 - left).

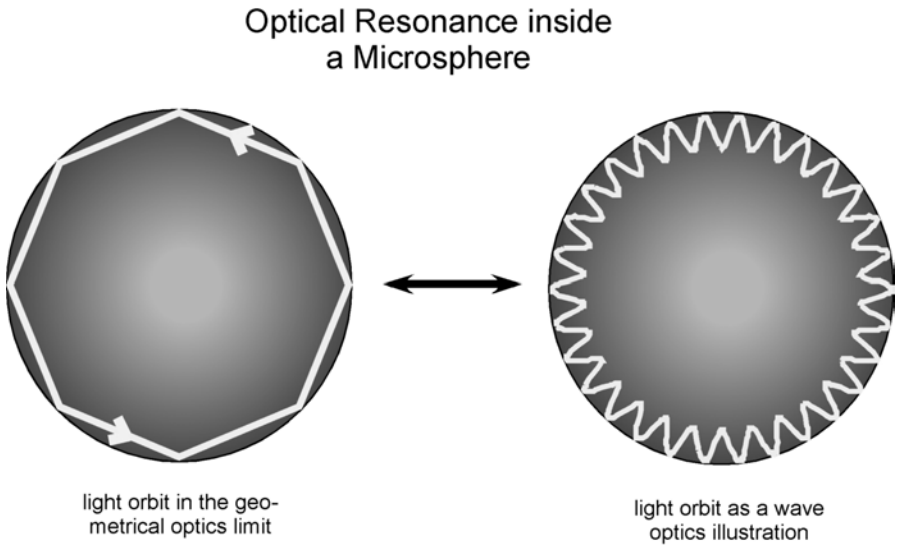

Figure A2.2 - Left: Ray optics interpretation of a light ray orbitting inside a glass microsphere due to total internal reflection at the sphere boundary. **- Right**: Wave optics interpretation of light confined in a microsphere: The light ray returns in phase after each revolution on its circular trajectory.

This ray optics interpretation can be extended to the image of the circulating lightwave (Fig.A2.2 - right). Inspired by this image, we might be tempted to draw the analogy to a hydrogen atom: the photons are orbiting around the inside of the sphere just as electrons are orbiting the nucleus in a Bohr atom. In quantum chemistry, a Bohr atom is described by the Schrődinger equation. Later we will see that a careful physical analysis of the light orbit indeed results in a Schrődinger-like equation. The Bohr atom thus seems a reasonable analogy for our photonic microsphere system. It is for this similarity, that the light orbits (also called *modes*) inside a microsphere are often referred to as "*photonic atom modes*" (Arnold, 2001; Arnold 2002). Like a hydrogen atom, this *photonic* atom is a very stable object. Scattering losses due to total internal reflection at the microsphere boundary are minimal and absorption of light in the transparent glass material is very low. The photons which form the light ray are able to circulate on their orbit several thousand times before they finally exit the microsphere cavity by loss mechanisms like scattering or absorption. This long lifetime of the microsphere-confined photon is associated with an optical path length of several hundred meters - if the photons would have traveled on a linear path in free space at all times. From this immense optical path-length we can already guess that the sensitivity for optical detection when using such microsphere-confined photons must be significantly enhanced as compared to other optical, *linear path* devices. In such conventional spectrometers light usually travels through a path the length of the cuvette-diameter: about one centimeter. Apart from the unprecedented path length, another advantage of a photonic atom mode is its resonant nature: the light returns in phase after each orbit thus forming an *optical resonance*. If the microsphere-confined, circulating light is brought in contact with a nanoscopic object such as a molecule, the interaction will be resonantly reinforced: the light ray will revisit the *same* analyte molecule many thousand times – an ideal situation if we wanted to optically study a single molecule.

In the following thesis I will experimentally and theoretically show how single, nanoscopic entities such as protein and DNA molecules as well as microscopic bacteria and polystyrene spheres perturb an optical resonance (photonic atom mode) confined inside a micron-sized silica sphere. I will show how this perturbation can be used for very

sensitive detection of nanoscopic Rayleigh entities as well as microscopic Mie entities. Although applications of microsphere resonators for sensing of dilute gas phase impurities by absorption measurements have recently been proposed (Rosenberger, 2000; Thompson, 2002) this is the first demonstration of biomolecular detection using an optical resonance. The detection principle utilizes changes in the frequency domain rather than time domain measurements of absorption.

The analogy with the Bohr atom will be used in developing a first order perturbation theory which will give us a quantitative understanding of the perturbative effect. A final chapter will conclude with a comparison of this novel sensing technology and its sensitivity with other, related optical biosensors such as surface plasmon resonance (SPR) devices.

Remark: Photonic atom modes are also often referred to as *Whispering Gallery Modes (WGMs)* in honor of Lord Rayleigh's whispering gallery in the St. Paul's Cathedral in London. There, sound waves travel along the outer wall of a walkway in the circular dome. The special construction conduits acoustic waves in a way which allows a remote listener to eavesdrop on a secretly whispered conversation at the other end of the walkway.

B General Properties and Quality of Resonant Systems

B1 – Resonant Systems in the History of Science

Resonant phenomena are well known across all scientific areas such as physics, chemistry and biology. For this reason they are introduced early in physics undergraduate education (Feynman, 1963). A resonance is something we all can naturally recognize. If looked at over a longer time period, a resonance seems to occur when an object (the oscillator or resonator) describes some kind of closed trajectory, which it follows periodically over and over again. The unperturbed resonating object, however, will only choose one specific frequency (the resonance frequency) for its oscillating journey. If manipulated by the outside observer, the least effort to force the object into its periodic behavior is needed when it is forcefully stimulated at this "built-in", natural resonance frequency. To put it into a picture, think of a child on a swing. The swing will periodically move back and forth at a constant, natural resonance frequency. To force the swing move higher, our least effort is needed if we repeatedly push the swing at precisely this natural frequency.

The resonant fork, the church bell or the violin-string are other well known acoustic examples of resonant systems. A pendulum is probably the most famous oscillator in the history of science. It has risen to fame by its use as a pacemaker in one of the first isochronous pendulum clocks designed by Christiaan Huygens in renaissance times.

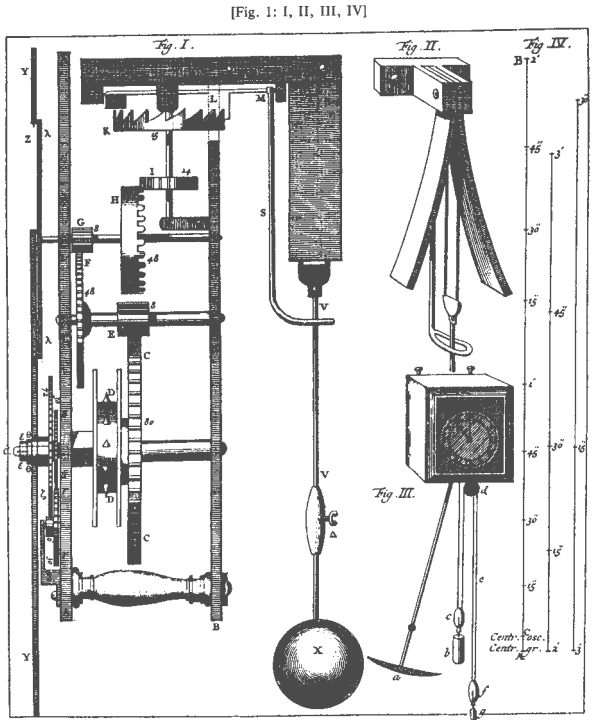

Figure B1.1: Illustration of the pendulum clock designed by Christiaan Huygens (From Huygens, 1673).

Huygens was the first to invent the system of a freely suspended pendulum connected to a clockwork driven by a weight (fig. B1.1). In his detailed publication *"Horologium Oscillatorium"* (1672) he analyses the oscillation with mathematical tools and introduces the cycloid path that allows the pendulum to follow an isochronous motion. From then on, the resonance frequency of pendulum clocks would be truly natural – even for large amplitudes. It did not take long until many church clocks (e.g. in Utrecht and Scheveningen) were equipped with Huygen's new invention.

Resonances are also widespread in nature and evolution has designed many exquisite resonant systems. The flight of an insect such as a mosquito would not be possible without its flight muscles exciting the resonance of its chitin torso. Many species communicate sending out sound waves generated in resonant organs such as the larynx in birds or the vocal chords in humans. Even the simplest building blocks of life, the cell, contains molecular resonators, which for example control the 24-hour wake and sleep cycle of many species on our planet earth, including our own. The heartbeat is paced by an electrical current circulating at a typical frequency of ~ 1 Hz through special tissues which command the contraction of the heart muscle on every oscillation.

In the following I will choose the mass on a spring as a simple, more abstract resonator to introduce general properties and a figure of merit for all the above-mentioned resonant systems. This model does not apply directly to our optical system but more to a mechanical setup where a quartz resonance is used for molecular detection. Nevertheless I felt that it is a good intuitive way of understanding a resonance and the wavelength shift associated with additional mass loading.

B2 – The Mass on a Spring

Let us imagine a mass m that is sitting on a spring k and bouncing up and down. Its motion shall be slightly damped by a piston γ pulled through a liquid of reasonable viscosity. The design is similar to a modern motorvehicle with a shock absorber connected to its spring-loaded wheel (fig. B2.1).

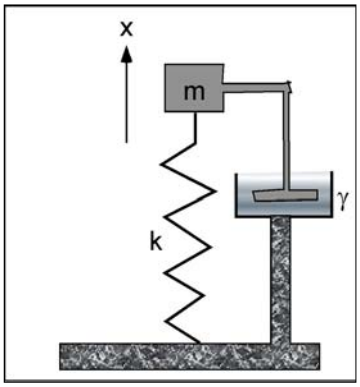

Figure B2.1: Mass on a spring. Imagine a mass m bouncing up and down on a spring k damped by a piston pulled through a liquid.

Newtons Third Law dictates the rules of the masses m linear motion in direction of the x-axis by balancing external driving force F "actio" with the "reactio" of inertia (mass m), friction (represented by the damping coefficient γ) and loading of the spring (represented by the spring constant k, with the angular frequency defined as $\omega_0 = k/m$):

$$\frac{d^2x}{dt^2} + \gamma\frac{dx}{dt} + \omega_0^2 x = F/m \qquad \text{Eq (B2.1)}$$

Suppose the driving force F is periodic $F = F_0 e^{iwt}$, then the square of the amplitude x_0 of our mass on a spring is calculated as a solution from equation (B2.1) as (Fig. B2.2):

$$x_0^2 = \frac{F_0^2}{m^2[(\omega^2 - \omega_0^2)^2 + \gamma^2\omega^2]} \qquad \text{Eq (B2.2)}$$

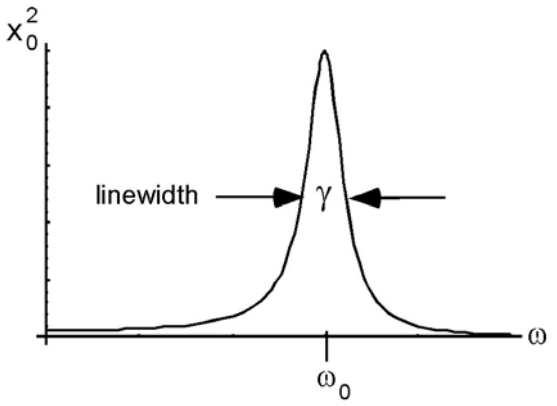

Figure B2.2: Amplitude response of a damped mass on a spring system.

If the frequency ω of the driving force F equals the natural frequency $\omega_0 = k/m$ then the system is at resonance and the response

of the amplitude is at maximum. Damping of the system (described by the magnitude of the coefficient γ) results in a broadening of the line width. In fact, the magnitude of the line width, measured at half-maximum of the amplitude signal x_0^2, is equal to the constant γ (that can be interpreted as the drag coefficient of the fluid divided by the mass m in this example). For the design of a shock absorber one would probably try to make the damping coefficient as large as possible without compromising the spring's relaxation time beyond acceptable values: By setting the force F = 0 in equation (B2.2) it can be shown that the maximal amplitude x_0 of the resonance decays exponentially with a time constant $\tau = \gamma/2$ which is called the transient response of the oscillator.

B3 - Energy and Quality factor Q of an Oscillator

In order to understand a time sustaining, steady-state response of the mass on a spring, however, it is necessary to analyze the balance of different types of energies (the potential and kinetic energy), which are mutually exchanged in this example. The change of total energy E with time t (the power P) of the mass on a spring resonator is calculated as:

$$P = \frac{dE}{dt} = F\frac{dx}{dt} \qquad \text{Eq (B3.1)}$$

With eq. (B2.1) we get:

$$P = m\left[\frac{dx}{dt}\frac{d^2x}{dt^2} + \omega_0^2 x\frac{dx}{dt}\right] + \gamma m\left(\frac{dx}{dt}\right)^2 \qquad \text{Eq (B3.2)}$$

Eq. (B3.2) can be re-written as:

$$P = \frac{d}{dt}\left[\frac{1}{2}m\left(\frac{dx}{dt}\right)^2 + \frac{1}{2}m\omega_0^2 x^2\right] + \gamma m\left(\frac{dx}{dt}\right)^2 \qquad \text{Eq (B3.3)}$$

Stored Energy *Dissipated Energy*

The first bracket [] consists of two terms: the kinetic and potential energy of the spring. This quantity is called the stored energy. In steady state, the mean stored energy does not

change. This means that if there would be no friction to damp the oscillation ($\gamma = 0$) the mass-on-a-spring would just store this energy by maintaining its oscillation for an infinite time. The mean stored energy $\langle E \rangle$ can be calculated by using a theorem which relates the average value $\langle x^2 \rangle$ of the complex variable $x = x_0 e^{i\varpi t}$ to the real part of the product with its complement $\langle x^2 \rangle = \frac{1}{2}\mathrm{Re}[x \times x^*]$.

Using this theorem we calculate the quantity:

$$\left\langle \left(\frac{dx}{dt} \right)^2 \right\rangle = \left\langle i\omega x_0 e^{i\varpi t} \times (-i)\omega x_0 e^{-i\varpi t} \right\rangle = \frac{1}{2}\omega^2 x_0^2 \quad \text{Eq (B3.4)}$$

The mean stored energy is then calculated as:

$$\langle E \rangle = \frac{1}{2} m \left\langle \left(\frac{dx}{dt} \right)^2 \right\rangle + \frac{1}{2} m \omega_0^2 \langle x^2 \rangle \qquad \text{Eq (B3.5)}$$

In "real life", however, there is always friction. Our mass on a spring is damped by the piston moving through the liquid. In each resonant cycle, this damping mechanism removes energy from our oscillator. If the oscillation is to be maintained in steady-state this *dissipated energy* has to be replaced by energy refueled through the action of the external force F on the mass m. If the energy loss is not replaced, the oscillation of the mass m will be damped to ultimately zero deflection. The mean power (the mean dissipated energy per period), that needs to be replaced for steady-state oscillation is represented by the dissipative term in equation (B3.3):

$$\langle P \rangle = \left\langle \gamma m \left(\frac{dx}{dt} \right)^2 \right\rangle = \frac{1}{2}\gamma m \omega^2 x_0^2 \qquad \text{Eq (B3.6)}$$

We can agree that we would call an oscillator "efficient" if the resonant system has the least energy leakage, which means the energy loss per cycle is minimal as compared to the stored energy. The figure of merit describing this efficiency of the oscillator is called Q-factor (Fowles, 1999). The Q-factor is defined as 2π times the mean stored energy divided by the energy dissipation per cycle. Using eq. (B3.5), eq. (B3.4) and eq. (B3.6) this equates Q as:

$$Q = 2\pi \frac{\frac{1}{2} m\left(\omega^2 + \omega_0^2\right)\left\langle x^2 \right\rangle}{\gamma m \omega^2 \left\langle x^2 \right\rangle 2\pi / \omega} = \frac{\omega^2 + \omega_0^2}{2\gamma\omega} \qquad \text{Eq (B3.7)}$$

The larger the Q-factor the better (or the more efficient) the oscillator.

For a good oscillator (large Q value), close to resonance, the definition eq. (B3.7) can be simplified by setting $\omega = \omega_0$. Q is then defined as:

$$Q = \frac{\omega_0}{\gamma} \qquad \text{Eq (B3.8)}$$

An oscillator achieves a better (higher) Q if the resonance frequency is large (mean stored energy is large) and the linewidth is very narrow (minimal energy dissipation per cycle). In horology for example, a large Q factor - equivalent with high frequency stability - is required to build most accurate clocks.

The following table shows typical Q-values as measured in different resonant systems ranging from physics to biology: A good pendulum clock made by Huygens in 1656 had a Q > 1000 and might have even surpassed the Q-value of a cheap, modern day mechanical wristwatch (Q ~ 100):

Thorax of an Insect	2.5
Integrated Circuit Filter (Cell Phone)	20
Mechanical Wristwatch	100-300
Surface Acoustic Waves	2000
Pendulum in Air	10^4
Quartz Crystal	10^6
First Atomic Clock	10^8
Optical Resonance in Microsphere	**10^9-10^{10}**

Table B3.1: Q-factors in biological and physical resonant systems.

It might come as a surprise, that the optical resonance in a microsphere even beats the first atomic clock in Q-factor and thus in precision! Indeed, Qs of up to 3×10^9 (highest for any optical system) have been experimentally measured for light trapped inside micron-sized silica and polystyrene spheres (Dubruil 1995; Gorodetsky, 1996; Lefevre-Seguin 1999). These experiments have almost reached the theoretical limit of Q in silica material at 1064 nm wavelength of 3×10^{10} (Weiss, 1995).

In this thesis, however, we are not so much interested in building the world's most precise clockwork but rather in the construction of the most sensitive system for detection of molecular events. In the following chapter I will explain how a large Q factor is related to the sensitivity of a resonant system used for detection of (molecular) mass. More general, in-depth reviews of high-Q whispering-gallery modes in microspheres and microdroplets and their various applications in quantum electrodynamics, cavity enhancement of fluorescence and Raman scattering etc. are available (e.g. Symes, 2004).

B4 – Mass Loading of an Oscillator: Resonance Frequency Shift

In the following we will quantitatively see how the frequency response of an oscillator can be used for sensitive detection of mass loading. As an instructive example I will demonstrate the shift in resonance frequency of a mass on a spring system after loading of additional sample mass Δm on the resonator (Fig. B4.1).

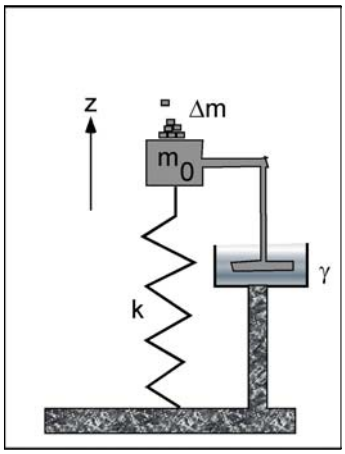

Figure B4.1: Additional mass loading Δm on a mass on a spring system.

Furthermore, this example will show that sensitive detection of the sample mass Δm depends on a high Q-factor: the higher the resonance frequency and the narrower the

linewidth - and thus the higher the Q - the smaller the least detectable sample mass Δm_{min}.

For a small damping coefficient γ, the (angular) resonance frequency ω_s of the resonator after loading of additional mass Δm is calculated as:

$$\omega_s = \sqrt{\frac{k}{m_0+\Delta m}} = \sqrt{\frac{k}{m_0}}\sqrt{\frac{1}{1+\frac{\Delta m}{m_0}}} \qquad \text{Eq (B4.1)}$$

This equation can be re-written using the unperturbed resonance frequency ω_0 before mass-loading:

$$\omega_s = \omega_0(1+\frac{\Delta m}{m_0})^{-\frac{1}{2}} \qquad \text{Eq (B4.2)}$$

For $\Delta m << m_0$ this can be approximated as:

$$\omega_s = \omega_0(1-\frac{\Delta m}{2m_0}) \qquad \text{Eq (B4.3)}$$

With the shift in resonance frequency defined as $\Delta\omega = \omega_s - \omega_0$ this equation becomes:

$$\Delta\omega = -\omega_0\frac{\Delta m}{2m_0} \qquad \text{Eq (B4.4)}$$

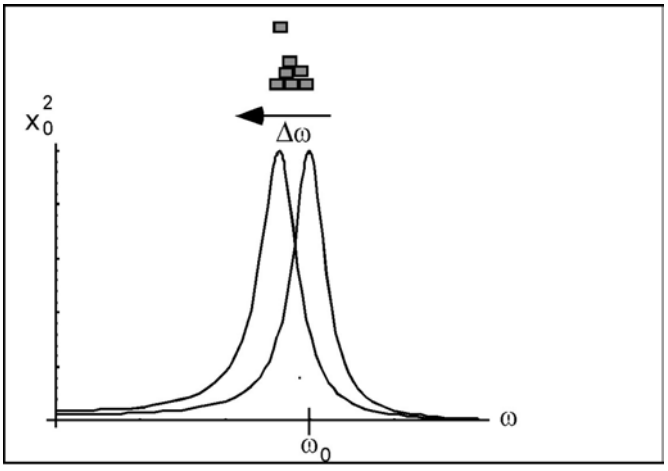

Figure B4.2: Resonance frequency shift $\Delta\omega$ of a resonant mass on a spring system after additional mass loading.

Fig. B4.2 illustrates such a frequency shift after additional mass-loading. This frequency shift due to additional mass is the reason why e.g. small mosquitos buzz at

high frequency, whereas large, grown up mosquitos are noticeable by a much deeper "hum". For the same token, a small, light resonant fork rings at high frequencies, whereas heavier ones are used to tune low frequencies. Assuming the smallest detectable shift in resonance frequency $\Delta\omega_{min}$ to be on the order of the linewidth γ:

$$\Delta\omega_{min} = \gamma \qquad \text{Eq (B4.5)}$$

and using the definition of the Q-factor Q = ω / γ:

$$\Delta\omega_{min} = \gamma = \frac{\omega_0}{Q} \qquad \text{Eq (B4.6)}$$

Using eq.(B4.4) and eq.(B4.6), this example shows that the detection limit Δm_{min} is proportional to 1 / Q:

$$\Delta m_{min} = \frac{2m_0}{Q} \qquad \text{Eq (B4.7)}$$

From this simple calculation we can draw the following general conclusions for resonant systems when used as detectors:

- Any such resonant systems can be used as detectors by measuring the frequency change due to additional load (e.g. additional mass on a pendulum, dust on a string, impedance in an electrical circuit, gravitational waves on a quasar). The frequency shift is predicted by eq. (B4.4).
- The detection limit will increase with large Q-values, eq. (B4.7).

As mentioned before, ultimate Qs as large as ~ 10^{10} have been measured for optical resonances in silica microsphere cavities, which makes them the *ideal* choice for a most sensitive biodetection system. Although the use of microspheres as sensors was already anticipated in 1995 (Griffel, 1996; Serpenguezel, 1995) this thesis is the first experimental demonstration and detailing of this sensing concept which allows highest sensitivity towards label-free molecular detection. Indeed I will later show that the

sensitivity is theoretically high enough to detect the smallest building blocks of the animated world: single, nanoscopic biomolecules.

It is fairly intuitive that mass-loading on a mass on a spring system leads to a change of its resonant frequency. But how can we conceptualize the frequency change of an *optical* microsphere resonator when detecting biomolecules? I will propose a simple picture in the next chapter.

B5 – Photonic Atom Sensor: A Simple Picture

In 1939, Richtmyer (Richtmyer, 1939) first proposed the use of an axially symmetric, dielectric object such as a microsphere to create an electromagnetic resonator with a high Q-factor. The unique properties of very high Qs and very small mode volumes, which are simultaneously obtainable in such resonators have since attracted much attention.

A light ray circulating inside a microsphere due to total internal reflection can only be stable if the ray – due to its electromagnetic wave nature - returns in phase when closing in on itself after one (or more) orbital revolutions. Then the periodically traveled, closed trajectory of the light creates an optical resonance due to constructive interference of the oscillating light. Any other phase relation will lead to destructive interference and annihilation of the microsphere-confined photons. Let us now imagine that a molecular adsorbent forms an additional layer of thickness t on the microsphere of radius a (fig. B5.1). The additional, molecular layer of material extends the radius a of the sphere to a total, new effective microsphere radius of t + a. What will happen to a given resonance after adsorption of such a molecular layer?

The resonance we are looking at is defined by the number of cycles (wavelengths) on an orbital path, in the example in fig. B5.1. To accommodate the now larger circumference of the sphere after molecular adsorption, a given resonance (of 30 cycles on an orbital path) will have to increase its wavelength from λ to $\lambda + \delta\lambda$ - where $\delta\lambda$ is the perturbation

of the wavelength introduced by the molecular adsorbent. Geometrical interpretation immediately relates the magnitude of the wavelength shift $\delta\lambda$ to the thickness t of the adsorbed layer: $\delta\lambda / \lambda = t / a$. We should be able to detect molecular adsorbents from an increase of the resonance wavelength change (or red shift of the resonance frequency) of a photonic atom mode!

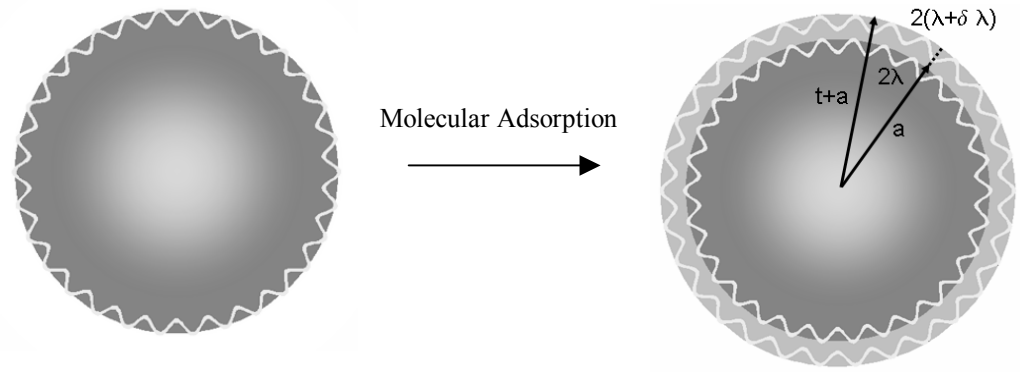

Figure B5.1: Optical resonance inside a microsphere. Increase of the effective microsphere radius a by an additional molecular layer t leads to a change $\delta\lambda$ of the resonance wavelength λ.

Let us relate the smallest measurable layer-thickness t_{min} to the quality factor Q of the optical microsphere-resonator. Since Q is defined as Q ~ wavelength / linewidth we calculate $\delta\lambda$ = Q x linewidth x t / a. If we assume the least detectable change of wavelength $\delta\lambda$ on the order of one linewidth we calculate the smallest detectable layer thickness of the adsorbent as t_{min} = a / Q. For a microsphere of 50 μm radius and a $Q = 10^{10}$ we should be able to detect a layer thickness of 5 femtometer, smaller than the diameter of an atom! In the next chapter I will outline an experimental setup, which will allow molecular measurements with high-Q photonic atom modes.

C Experimental Approach: Coupled Microsphere-Waveguide System

C 1 - Excitation and Detection of Microsphere Resonances

In the simplest experimental design I could just shine light from a coherent source onto the glass microspheres and hope to excite resonant modes. I would know about the light orbiting inside the sphere by looking at the light scattered off the microsphere surface. At resonance, the scattering intensity will be resonantly enhanced. This most direct light-microsphere coupling method, however, is known to be very inefficient (Lin, 1998). The reasons for this inefficient coupling are physical and thus controllable. A deeper understanding of the underlying rules presented in this chapter will enable us to optimize relevant coupling parameters and effectively excite and detect optical resonances in microspheres.

Channeling of light through a guiding structure (called a waveguide) is a convenient way to gain more control over a waveguide-confined, electromagnetic wave. It has been shown that light propagated through a narrow waveguide, such as an optical fiber, can be used to drive the resonant modes inside the microsphere by fine-tuning of relevant the coupling parameters (Knight, 1997; Little, 1999; Serpenguezel, 1995). These examples also show the first observation of resonances of the microsphere as dips in the transmission spectrum of the fiber transmitted light.

Light transmitted through an optical fiber is usually entirely contained within the outer material of the fiber called cladding. If I remove this outer part of fiber material (e.g. by an etching process as I will detail later) I will be left with the remaining fiber core. Light propagating through this thinned part of the fiber is no longer completely protected by the cladding material but extends in its environment. The field that now penetrates the environment is called ‘evanescent’. The evanescent field is stealth. This invisible field

however, makes it possible to access the propagating ray at any point along this thinned portion of the fiber. I can now place the microsphere in mechanical contact with the thinned fiber-part and thus illuminate the fiber-sphere contact region with evanescent light. This turns out as a very efficient way of driving resonant modes: The evanescent field overlaps with the modes of the microsphere resonator. Experimentally I will be able to couple an amount of light into the microsphere which is large enough so that I will even see the resonant light orbits with the help of a simple microscope.

Let me come back to the mass on a spring oscillator in order to understand the phase relationship between driving force (in this case the fiber propagated light) and amplitude response of the microsphere at resonance.

Before, we have calculated the amplitude response of the mass on a spring system eq. (B2.2). We can calculate the phase response of the oscillator from the angle of this complex phasor as:

$$\tan\theta = {}^{-\gamma\omega}\!\Big/\!_{(\omega_0^2-\omega^2)} \qquad \text{Eq (C1.1)}$$

We see immediately, that at resonance $\omega = \omega_0$ the amplitude response of the oscillator will be $\pi / 2$ out of phase with the driving force. In the picture of the child on a swing at resonance, we will push with maximum force whenever the swing sways through the minima at zero swing deflection.

In my microsphere-fiber system, part of the fiber-propagated light (or energy) can couple both ways, in and out of the microsphere resonator at the region of contact between microsphere and thinned fiber. Similar as for the mass on a spring system the most efficient coupling occurs only at the resonance frequency. Then, for each coupling direction, *in* and *out* of the microsphere, there will be a $\pi / 2$ phase shift. The light coupling back from the microsphere into the fiber will thus be in total 180° out of phase (Little, 1998) when compared with the uninterrupted, fiber-forward propagated light. This 180° destructive interference of the light coupling back from the microsphere at

resonance will provide us with an elegant method for detection of the resonant modes: whenever the wavelength of the light sent through the optical fiber matches the resonance wavelength of the sphere I will observe a significant loss in the fiber-transmitted light intensity recorded at the far fiber end. If I record a complete transmission spectrum by tuning the wavelength of the light launched into one end of the fiber over a broad enough spectral width I will be able to detect microsphere resonances as one or several Lorentzian dips in the transmission spectrum .

Notice that the intimate physical reason for the phase shift of the light coupling between fiber and microsphere, however, can only be explained using quantum mechanical concepts.

With this knowledge of resonant interference, I can envision the simplest experimental setup (Fig. C1.1) as follows:

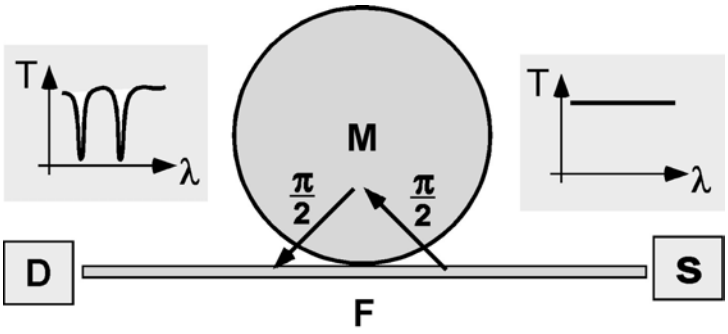

Figure C1.1: Destructive, resonant interference. The light (from laser source S) coupling back from the microsphere M into the optical fiber F is 180° out of phase with the forward propagating light in the waveguide. At resonance I thus expect a loss in the fiber transmitted intensity T as recorded by the detector D. Microsphere resonances will appear as Lorentzian dips in the transmission spectrum T if the laser wavelength λ is tuned over a broad enough spectral width.

The necessary components for a simple setup are four-fold: (1) A tunable light source S able to cover a sufficient spectral width; (2) an optical fiber F thinned at the microsphere contact region for evanescent coupling; (3) the microsphere cavity M and (4) a photodetector D. The digitally recorded transmission spectrum T will allow us to identify microsphere resonances as Lorentzian-shaped dips in the transmission spectrum.

With this picture in mind I can also introduce the idea of coupling efficiency and critical coupling. Critical coupling occurs, when the fiber-transmitted light will be completely annihilated. This occurs for one critical condition: when the amount (intensity) of fiber

transmitted light that has not coupled into the microsphere matches exactly the intensity of light coupling back from the microsphere at destructive 180° phase difference. Optical losses of the microsphere cavity will limit the light intensity coupling back from the microsphere. The microsphere losses can be tuned to reach this point of critical coupling (Cai, 2000). This important phenomenon finds its application in add-drop filters that might be used in future telecommunication devices (Cai, 1999; Laine, 2000). Wavelength division multiplexing (WDM) is a proven solution to solve the bandwidth bottleneck in the telecommunications industry. A WDM system utilizes the enormous bandwith of an optical fiber and multiplexes many channels independently by modulating each one of them with their own data onto a single fiber - thereby increasing the throughput. Add/drop filters which are able to access one channel of a WDM system without disturbing other channels are thus very important.

In the remaining parts of this chapter I will go into the details of the experimental components of this minimal setup for detection of microsphere resonances in a fiber-microsphere system. In the last part of this chapter I will present first results obtained with this experimental setup.

C2 - Light Guidance Principles

C2.1 Total Internal Reflection of Light: Snell's Law at a Critical Angle

We know that the speed of light is a universal constant, independent of any frame of reference. If light passes through matter, however, it is slowed down due to the dielectric nature of the transparent material, which is composed of individual, polarizable atoms. Light as an electromagnetic wave will polarize each of the atoms that lie on its optical path. Polarization of atoms at the optical frequency of the incident light will generate an electromagnetic field, which in turn interferes with the incident light ray itself. This interference results in the observed reduction of the speed of light in materials such as

silica glass. We define the index of refraction as the factor by which the speed of light in vacuum exceeds the speed of light in the dielectric material $c_{vacuum} = n \times c_{material}$.

At an interface of two materials such as air and water, the difference in the speed of light in the two media leads to two phenomena: refraction and total internal reflection of a light ray passing through the interface.

To illustrate both effects, imagine a light ray, which originated under water but now passes through the water-air interface, leaving the water surface at an angle θ_{out}, which we observe as always larger than the incident angle θ_{in} (Fig. C2.1.1 A). This well-known phenomenon is experienced by objects appearing closer under water than they actually are (Fig. C2.1.1 B, the magnification factor in sea water is about 1.3).

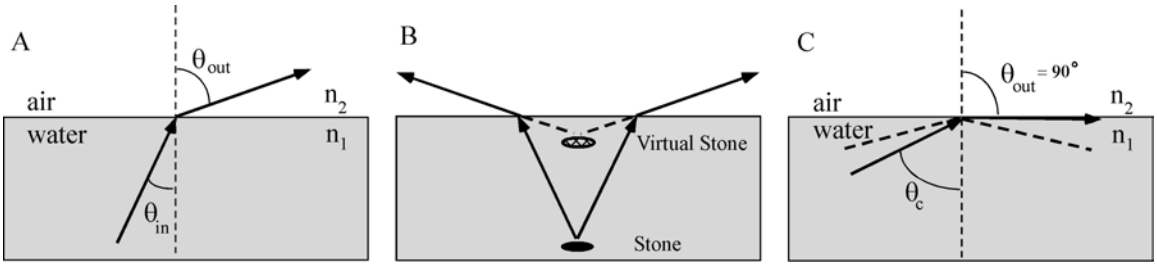

Figure C2.1.1 A: Refraction of a light ray at an air-water interface. Reduction of the speed of light in water as compared to air leads to the observation that the exit angle θ_{out} is always larger than the incident angle θ_{in}. **B:** Objects spottet under water appear closer to the observer. **C**: Total internal reflection occurs for $\theta_{in} > \theta_c$.

The relationsip between incident θ_{in} and exit angle θ_{out} is described by Snell's law:

$$n_1 \sin\theta_{in} = n_2 \sin\theta_{out}$$

In general, light passing from a medium of higher refractive index into a medium of less refractive index will leave the interface at an angle θ_{out} larger than the incident angle θ_{in}.

If the exit angle θ_{out} reaches 90° for $\sin\theta_{in} = \frac{n_2}{n_1}$ something very interesting happens. The light ray will now no longer leave the high refractive index medium but instead the boundary will now act as a mirror which reflects (Fig. 2.1.1 C) the incident light for any incident angle $\theta_c < \theta_{in} < 90°$. This phenomenon is called "total internal reflection" (TIR). Because of TIR, a fish cannot see out of the water except for a limited cone of vision overhead bounded by the critical angle of 49° for water. Divers know this phenomenon: looking up to the water surface they see the "dry" world inside a solid angle of 49°. For angles outside that cone, the water surface forms a perfect mirror and gives a pretty good view of the surrounding underwater environment.

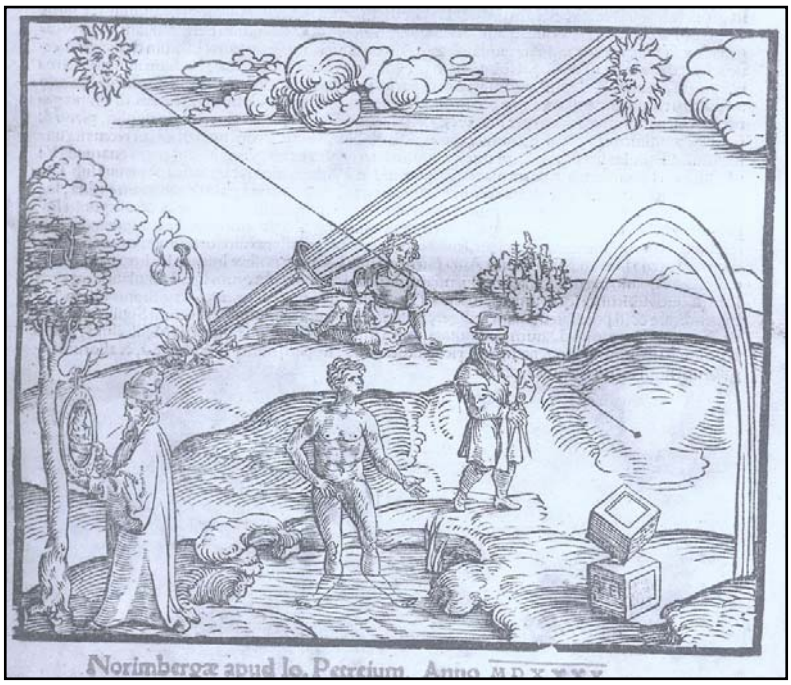

Fig. C2.1.2: An illustration taken from Witelo's book showing the effect of total internal reflection at an air-water interface. Notice the legs of the person standing up to his knees in the water.

The observation of Snell's law dates back as far as the Middle Ages. In the 13th century, Witelo, one of the earliest 'opticians' describes the effect of refraction and diffraction at a water-air interface. His handwritten notes were later published in 1536.

Fig. C2.1.2 shows an illustration taken from this book. Notice the man standing up to his knee in water – Snell's law is the cause for the dogleg appearing at the water-air boundary.

C2.2 Optical Fibers: Application of Snell's Law

An important, modern technological device based on the effect of total internal reflection is the optical fiber. An optical fiber is made of two materials: a core with slightly higher refractive index as compared to the cladding (fig. C2.2.1). Successive internal reflection of a light ray launched into the core at an angle θ larger than the critical angle θ_c will allow the propagation of the light over long distances. The critical angle defines the numerical aperture of the fiber: only light launched into the fiber within an acceptance 'cone' defined by the critical angle can propagate by TIR: NA = n_{core} sin [2 x (90-θ_c)] for fibers operating in air (in this case air is the cladding material).

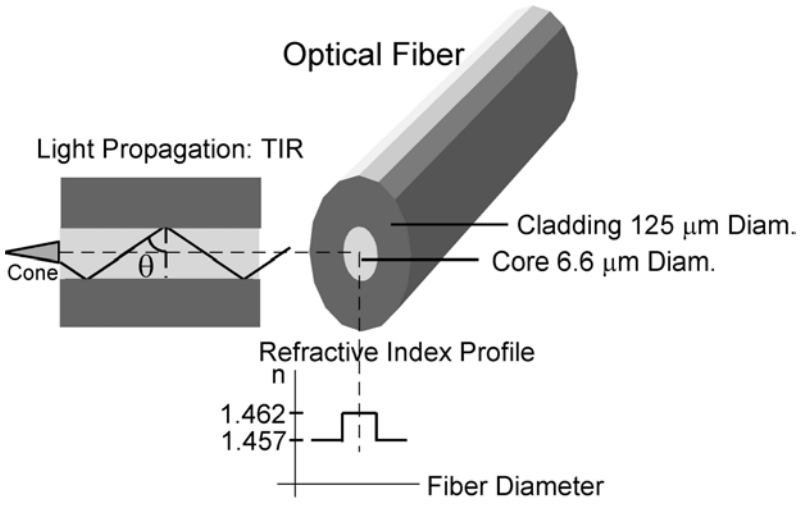

Figure C2.2.1: Schematics of a typical optical fiber. Light is propagated by total internal reflection through a high refractive index material which forms the core of the fiber.

Optical fibers are typically used to transmit infrared light at 1.3 μm or 1.5 μm wavelength. As with electrical wires, modulation in this case of light instead of current can be used for ultra-fast transmission of information (up to several thousand megabits per second). Amplitude modulation of optical oscillators is used to transmit a phone call at one specific frequency. At the other end of the optical fiber, this frequency is isolated and analyzed by a photodetector equipped with a frequency-specific filter. As we will see for the example of a dielectric microsphere, the Q of optical devices (such as oscillators for emission and filters for detection) are very high and the conjugate line widths are very narrow. The high-Q allows many different signals to be transmitted through the same fiber, each using non-overlapping, neighboring frequencies (WDM).

The ideal choice of fiber material will have a low absorption coefficient at the wavelength of the transmitted light to enable transmission with minimal absorption losses across long distances. Since it is easier to manufacture lasers operating at a specific wavelength than to synthesize large quantities of an artificial material with the desired optical property the telecommunications industry has chosen the naturally abundant silica as the first choice photonics material. Silica is an ubiquitous material in the upper layer of the earth's crust. It can be processed into fibers as thin as 50 nm (Tong, 2003) which allows minimal material usage. The ideal operating wavelengths are found at the minima of the silica absorption spectra: at 1.3 μm and 1.55 μm. Typical losses of IR-optical fibers are ~ 0.4 dB/km (a typical coaxial cable operated at 100 MHz has an attenuation of 22.6 dB/km in comparison). Unlike visible light the photon energy $E = h \times f$ of infrared light is too small to be detected by conventional silicon junction photodetectors (responsitivity: 300-1100 nm). Special germanium or indium gallium arsenide (InGaAs) photodetectors with smaller bandgaps had to be designed to be able to detect intensities ranging between 1000-1700 nm wavelengths. They are now available in non-multiplying, conventional pn-junction (PIN) designs or as avalanche photodiodes (APDs).

C2.3 Modes of an Optical Fiber

All rays launched at angles within the acceptance cone of the optical can be trapped and propagated by TIR. However, this is not true for all angles within that range. In fact, interference within the fiber itself limits the propagation to only specific angles (modes).

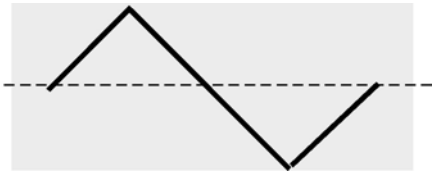

Figure C2.3.1: One translational period of a light ray propagating through an optical fiber.

When internally reflected at the upper and lower boundary along the narrow fiber, the light ray interferes with itself for every translational period (fig. C2.3.1). The electromagnetic wave at the very beginning and at the end of this translational zigzag period will have to interfere constructively for light propagation to occur. As for any cavity, a fiber waveguide has to fulfill the resonant condition for constructive

interference. Within one translational period, the phase of the light ray has to change by N x 2 π, with N being an integer number (0, 1, …).

As we can see from Fig. C2.3.1, the total phase shift in one translational period is the sum of the phase shift along the zigzag ray path plus the phase shift that occurs due to two reflections, one at the upper and one at the lower fiber boundary.

In the following I will attempt to derive the allowed propagation angles of fiber modes and present them in a mode chart. For the derivation it will be necessary to first understand another, very important property of total internal reflected light: the accompanying evanescent field. Later, understanding of this evanescent field will also be instrumental for the detection of mass-loading onto the sensor surface.

C2.4 Evanescent Fields: The Imaginary Solutions of Snell's Law

From our previous discussion of light propagating through an optical fiber one might get the impression the light is entirely confined to the core of the propagating fiber. This, however, is not true.

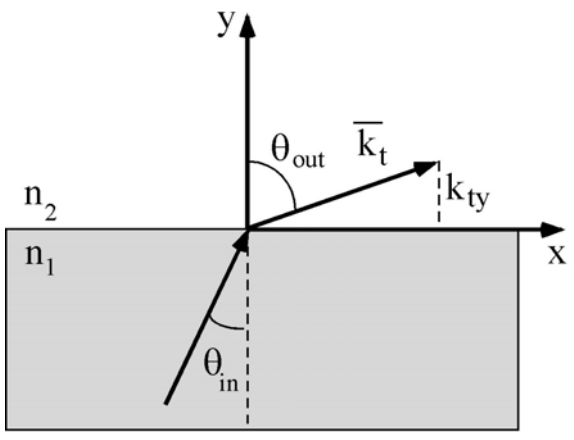

Figure C2.4.1: Light refraction and reflection at a boundary. If the incident angle Θ_{in} reaches the critical angle, the vertical k_{ty} component of the wavevector $\vec{k}_t$ describing the refracted light ray becomes imaginary.

Snell's law so far correctly predicted the refraction at a boundary of a high and low refractive index material (fig. C2.4.1). The light ray will be bent outwards when entering the low refractive index medium. Now, let's have a look what happens to the predictions of Snell's law if the incident angle θ_{in} is larger than the critical angle. So far we have treated this case as if the light is totally contained within the high refractive

index material (the fiber core) by reflection. Even for this case, however, Snell's law predicts an electromagnetic field component (described by the wave-vector component k_{ty}) which extends into the low refractive index medium in y-direction, although there is no refracted light ray leaving the fiber core (fig. C2.4.1). The k_{ty} vector component in this case is imaginary as we will see. Physically, an imaginary $\vec{k}_t$ vector describes a damped field that is exponentially decays the further we move from the boundary into the lower refractive index medium. Since the field strength rapidly decays to zero this field is seen as stealth from the outside and is therefore referred to as an "evanescent" field. In the following we will derive the decay-length of this so called evanescent field starting out from Snell's law.

The wavevector $\vec{k}_t$ of the transmitted (refracted) wave can be written as the sum of its components along the coordinate axis:

$$\vec{k}_t = \vec{k}_t \cos\theta_{out}\vec{j} + \vec{k}_t \sin\theta_{out}\vec{i} \qquad \text{Eq (C2.4.1)}$$

with $\vec{i}$ and $\vec{j}$ being the unit vectors in direction of the x and y coordinate axis, respectively.

K_{ty}, the y-component of the wavevector $\vec{k}_t$ describes the evanescent field we are looking for and is calculated as:

$$k_{ty} = k_t \cos\theta_{out} = k_t\left[1 - \sin^2\theta_{out}\right]^{\frac{1}{2}} \qquad \text{Eq (C2.4.2)}$$

With Snell's law $n_1 \sin\theta_{in} = n_2 \sin\theta_{out}$ we get

$$k_{ty} = k_t\left[1 - \left(\frac{n_1}{n_2}\right)^2 \sin^2\theta_{in}\right]^{\frac{1}{2}} \qquad \text{Eq (C2.4.3)}$$

If $\theta_{in} > \theta_c$ (incident light angle is larger than the critical angle for total internal reflection), the square root is negative and, as mentioned before, k_{ty} will become imaginary:

$$k_{ty} = k_t i\left[\left(\frac{n_1}{n_2}\right)^2 \sin^2\theta_{in} - 1\right]^{\frac{1}{2}} \qquad \text{Eq (C2.4.4)}$$

Inserting the imaginary k_{ty}-component in the general wave equation for an electromagnetic field we calculate the evanescent field as:

$$E = e^{-\alpha k_t y}\left[e^{i\left[k_x x - wt\right]}\right] \qquad \text{Eq (C2.4.5)}$$

with

$$\alpha = \left[\left(\frac{n_1}{n_2}\right)^2 \sin^2\theta_{in} - 1\right]^{\frac{1}{2}} \qquad \text{Eq (C2.4.6)}$$

As we can see from this formula, the evanescent field strength drops exponentially along the y-axis. How fast does the evanescent field get attenuated? The field drops to 1/e of its initial value at

$$y_{1/e} = \frac{1}{\alpha k_t} = \frac{\lambda}{2\pi\left[\left(\frac{n_1}{n_2}\right)^2 \sin^2\theta_{in} - 1\right]^{\frac{1}{2}}} \qquad \text{Eq (C2.4.7)}$$

In most applications the decay-length of the evanescent field is on the order of one wavelength, typically 1 μm for infrared light. This confinement of the evanescent field to a surface layer of one micrometer thickness it widely used in microscopy ("total internal reflection microscopy"). The evanescent field allows illumination of only a small sample volume and thus can be used to eliminate background light (or noise) in microscopy. An object, e.g. a cell or a molecule, immobilized on a high refractive index surface can be evanescently back-illuminated and a high NA objective can be used to collect the image from above. Since the illuminated sample volume containing the cell or molecule is very small, disturbing light scattering from the surrounding medium is minimized. The evanescent wave can also be utilized to excited fluorescent labeled molecules. In this case the evanescently improved signal-to-noise ratio is high enough to achieve single molecule resolution. Notice however, that the molecule needs to be modified with a fluorescent tag.

Now that we have understood the principle of evanescent fields associated with TIR light, we are able to derive the different modes (propagation angles) in an optical fiber. The solution will be represented in a mode chart and we will calculate the decay-length of the associated evanescent fields. This will lead us to an important conclusion for the design of my setup: in order to detect Lorentzian resonance dips in the transmission spectrum of a microsphere-waveguide system we have to use a 'single mode' fiber.

C2.5 Mode Chart of a Flat Waveguide

We can calculate the modes in an optical fiber by matching the evanescent field in the cladding with the evanescent field in the fiber-core (thus solving the problem by using a boundary condition).

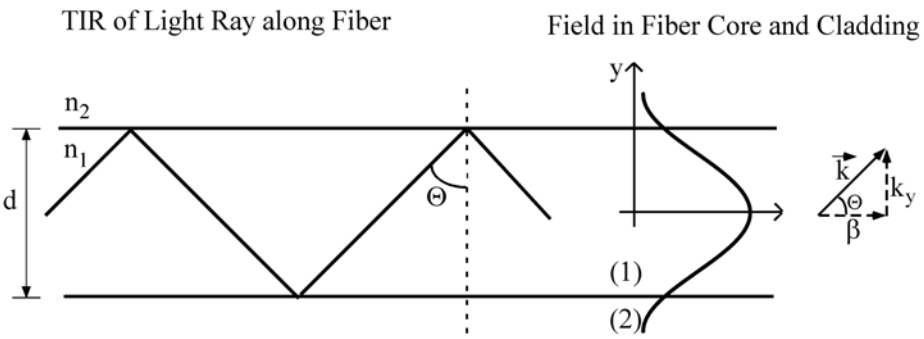

Figure C2.5.1: Wavevector $\vec{k}$ and electromagnetic field associated with TIR light between a core (1) – cladding (2) boundary. The diameter of the waveguide is d. n_1 and n_2 are refractive index of core and cladding. The inset on the right shows the Gaussian profile of the propagating field.

As we saw before, the light ray travels on a zigzag path through the core of an optical fiber (fig. C2.5.1). The light ray is totally reflected each time it encounters the core-cladding boundary. In this geometrical interpretation the wavevector $\vec{k}$ hits the boundary at a certain angle $\theta > \theta_c$. In the previous chapter we saw how this internal reflection leads to an evanescent field extending along the y-axis into the low refractive index medium (the cladding) of the fiber. Let us calculate the field along the y-direction but this time inside the fiber core.

With k_y being the component of $\vec{k}$ in y-direction, we calculate $k_{y,core}$ in the core as:

$$k_{y,core} = k\cos\theta = \frac{2\pi n_1}{\lambda}\cos\theta \qquad \text{Eq (C2.5.1)}$$

Depending on whether the light is reflected at the upper or lower core boundary, $k_{y,core}$ will be either negative or positive, respectively. This however means that we are dealing with two types of waves along the y-direction of the core, both traveling in opposite directions. The interference of both waves results in a standing wave pattern for the electromagnetic core-field, similar to a violin string. Because of the horizontal symmetry, the standing wave $E_{y,core}$ inside the core has to adopt a cosine waveform (fig. C2.5.1 region (1)):

$$E_{y,core} = \cos k_{y,core} y \qquad \text{Eq (C2.5.2)}$$

In the cladding, we found the evanescent field strength decaying as (fig. C2.5.1 region (2); eq. (C2.4.7)):

$$E_{y,cladding} = Ae^{-k\cdot n_2\left[\left(\frac{n_1}{n_2}\right)^2 \sin^2\theta_{in} - 1\right]^{\frac{1}{2}} y} \qquad \text{Eq (C2.5.3)}$$

Matching both field strengths, $E_{y,core}$ and $E_{y,cladding}$ at the core-cladding boundary means that the electric field has to fulfill two boundary conditions: field strength and field gradient have to be equal for y=+/-d/2 (fig. C2.5.1). For symmetry reasons we only have to consider one boundary y =d/2:

Boundary condition one:

$$E\left(\frac{d}{2}\right)_{y,core} = E\left(\frac{d}{2}\right)_{y,cladding} \qquad \text{Eq (C2.5.4)}$$

$$\cos k_{y,core}\frac{d}{2} = Ae^{-k\cdot n_2\left[\left(\frac{n_1}{n_2}\right)^2 \sin^2\theta_{in} - 1\right]^{\frac{1}{2}} \frac{d}{2}} \qquad \text{Eq (C2.5.5)}$$

Boundary condition two:

$$\nabla E(\frac{d}{2})_{y,core} = \nabla E(\frac{d}{2})_{y,cladding} \qquad \text{Eq (C2.5.6)}$$

$$-k_{y,core}\sin k_{y,core}\frac{d}{2} = -Ak\cdot n_2\left[\left(\frac{n_1}{n_2}\right)^2\sin^2\theta_{in}-1\right]^{\frac{1}{2}} e^{-k\cdot n_2\left[\left(\frac{n_1}{n_2}\right)^2\sin^2\theta_{in}-1\right]^{\frac{1}{2}}\frac{d}{2}}$$

Eq (C2.5.7)

By taking the ratio of eq. (C2.5.5)/eq. (C2.5.7) we obtain a transcendental equation from which we can calculate the (TE) modes of a fiber:

$$\tan(\frac{k_{y,core}d}{2}) = \frac{k\cdot n_2}{n_1\cos\theta_{in}}\left[\left(\frac{n_1}{n_2}\right)^2\sin^2\theta_{in}-1\right]^{\frac{1}{2}} \qquad \text{Eq (C2.5.8)}$$

with $k_{y,core} = k\cos\theta = \frac{2\pi n_1}{\lambda}\cos\theta$ Eq (C2.5.9)

This calculation is valid for one possible polarization of the light. The E-field in this calculation was considered as transverse electric (TE) polarized: The E-field vector was pointing out of the plane of fig. C2.6.1. Another possible solution can be obtained if the *magnetic* component of the electromagnetic wave is considered pointing out the plane in Fig. C2.6.1. The polarization is then referred to as transverse magnetic (TM).

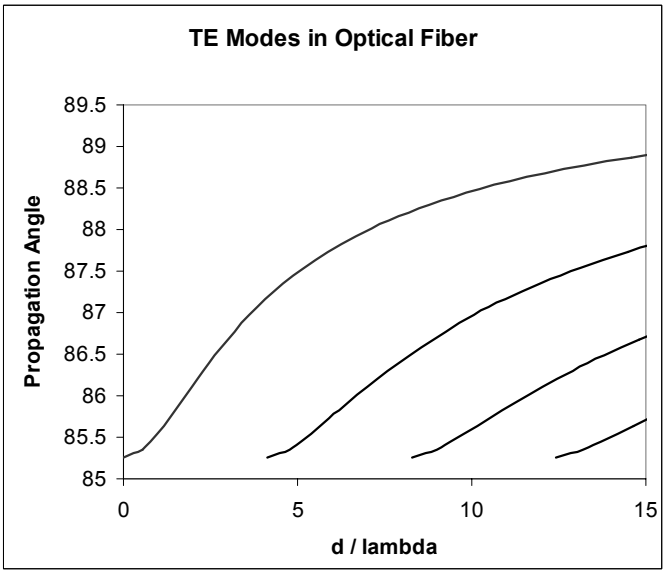

Figure C2.5.2: Transverse electric modes in a flat waveguide. The propagation angle θ of each mode is plotted versus the waveguide core diameter d divided by the wavelength λ. Refractive indices (as in a smf-28 fiber): n_1=1.1457, n_2=1.462.

Fig. C2.5.2 shows the possible θ propagation angles (modes) for a typical flat waveguide of diameter d calculated from equation C2.5.8. Depending on the ratio of waveguide core thickness d to wavelength λ of the propagated light (x-axis in fig. C2.5.2) one or more modes can be transmitted through the fiber core at their corresponding angles. The larger the diameter d of the waveguide core, the more modes can be propagated at one wavelength. For a given core diameter, several modes can be propagated by varying the wavelength of the fiber-transmitted light.

Fig. C2.5.2 shows the mode chart of a flat optical waveguide similar to the fiber which I will use in my experiments (smf-28) with $n_{core} = 1.457$ and $n_{cladding} = 1.462$ operating at a wavelength of 1.3 μm. From the mode chart we can determine, that a single mode fiber should be less than 5.07 μm in diameter. If a fiber is manufactured with this (or a smaller diameter) only one mode is propagated through the waveguide.

The diameter of 5.07 μm is very close to the core diameter of the actual smf-28 fiber (single mode fiber, 6.6 μm) I will be using in my experiments. This fiber of 6.6 μm core diameter, however, is designed as single mode, which is in accordance with an exact calculation that takes into account that the fiber is rather a cylindrical than a slab waveguide. With the above instructive example for a slab waveguide, however, we can understand the reason for the limited mode numbers of any optical waveguide. We can also understand that a fiber with less core diameter cannot support as many modes as a fiber with a larger core diameter. From the mode chart we can also examine how the propagation angle changes for a given mode depending on the waveguide thickness. We also note that the component of the wavevector $\vec{k}$ pointing along the propagating direction of the fiber core is called effective propagation vector and its magnitude is called effective propagation constant β (fig. C2.6.1) a constant widely used by engineers in the optical fiber area.

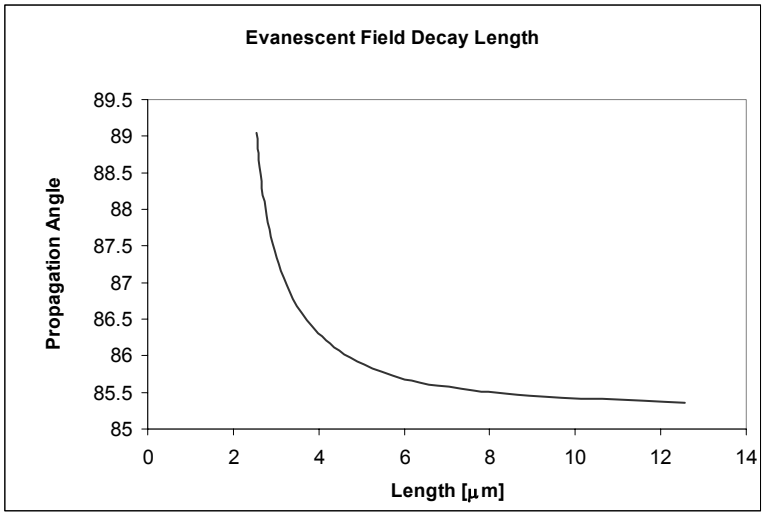

Figure C2.5.3: Evanescent field penetration depth [length in μm] associated with the propagation angle θ of a given mode.

Fig. C2.5.3 shows how the decay length of the evanescent field depends on the propagation angle θ. We can order all possible modes in a waveguide by their propagation angle. Modes close to 90° propagation angle are called lower order modes, and the first order mode will have the largest propagation angle and thus the largest propagation constant β. The larger the effective propagation constant β the smaller the penetration depth of the associated evanescent field.

We explained before, that we want to take advantage of the phase shift that occurs for evanescent coupling between a fiber and a microsphere cavity in order to detect resonances as dips in the transmission spectrum.

This destructive interference at resonance occurs only if there is exactly *one* available mode in the fiber into which the light can couple back from the microsphere. In my experimental setup I have to make sure that I am using a single mode fiber at 1.3 μm wavelength. Furthermore, I have to pay close attention to the thinned fiber part from which we will couple the light into the microsphere. As we will see in the experimental section, the thinning of the fiber will in fact help us to maintain the fiber transmission at single mode: if I first remove the fiber-cladding material I will change the refractive index n_2 and thus initially render the fiber withoud cladding multimode. Further thinning of the fiber core will limit those additional modes.

Furthermore, the thinning will extend the decay-length of the evanescent field which again will reward us with higher coupling efficiencies: the thinner I fabricate the fiber at the fiber-microsphere contact the deeper the resonant dips. In fact, the deepest dip (critical coupling) is achieved for a certain optimal diameter of the thinned fiber. For this diameter the light intensity, which is coupling back from the microsphere matches the uninterrupted light intensity propagating forward through the fiber. We now understand why we can achieve critical coupling by either adjusting the losses in the microsphere or by tailoring the thinned fiber to an optimal diameter.

C3 - Distributed Feedback Laser: A Current-Tunable Source

In the previous chapter I explained the necessity for the waveguide to be single mode. We understood that a waveguide can propagate different modes by either varying the waveguide diameter or by varying the frequency of the transmitted light. In order to detect microsphere resonances as dips in the transmission spectrum I have to propagate exactly one mode through the fiber. This means, that in addition to a single mode fiber I need a single mode light source: I have to make sure that the coherent light source operates at only one wavelength at a time.

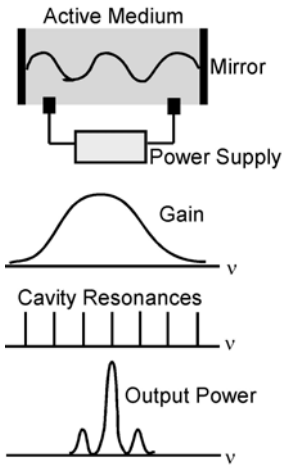

Figure C3.1: Schematics of a laser cavity. Gain spectrum, cavity resonances and output power.

A coherent light source (laser) can be built by confining an active (gain) medium to a cavity. A cavity is built of essentially two opposed mirrors which contain the light within the active medium due to reflection at the mirrored boundaries (fig. C3.1). The standing wave pattern of the cavity modes remind us in shape of the mechanical analog: the violin string. The first laser is a quite recent invention and its working principle was introduced in the late 60's. The active medium has in general more than two but only a limited number of allowed energy states and thus

provides amplification (pumping of the excited states) over a limited frequency range ν. (see gain spectrum in fig. C3.1).

For this application it is necessary, however, to work with only a single mode at a time in order to detect microsphere resonances as transmission dips. It is possible to design a (diode) laser cavity with only one mode of operation. Selection of only a certain wavelength/frequency of the laser cavity is achieved by coupling of the laser modes to a Bragg grating. The Bragg grating is not located in the cavity but we can understand from the previous chapter how evanescent coupling at the cavity boundary can be used to couple to the modes of the light within the lasing cavity. The Bragg grating is designed to allow only amplification of one mode. Since the grating acts as a distributed filter, such laser diodes are known as distributed-feedback (DFB) laser diodes.

DFB laser diodes have another feature important to these experiments. The laser wavelength can be tuned by varying the current drawn from the power supply (Griffel, 1996; Engelbrecht, 2000). I can scan over a narrow spectral width of typically less than 1 nm by ramping the operating current with a current-controllable power supply from 0 to its maximum value (typically several mA). The higher the current the more electrons are flowing through the active medium. The refractive index of the active medium, however, is a function of electron density, which explains the current tunability of semiconductor lasers in general. Furthermore since I am dealing with a single mode DFB laser I do not have to worry about any mode hopping between allowed laser cavity modes.

Figure C3.2: Michelson-Interferometer like setup to determine the tuning coefficient of a current-tunable DFB laser diode.

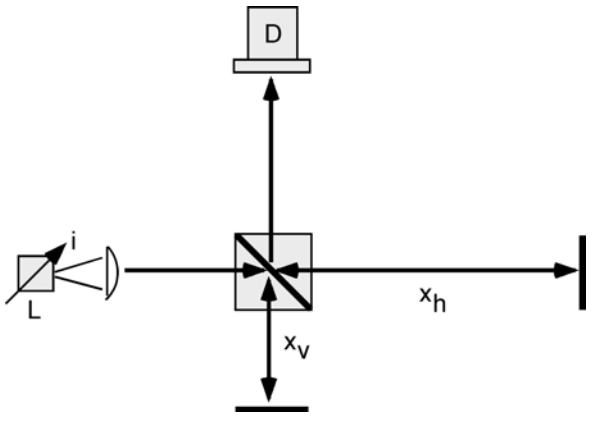

In my experiments, I will be using a DFB laser operating at 1.3 μm. The current tunability of DFB lasers is not a widely used feature and therefore the tuning parameter – change of wavelength Δλ

with current Δι: $\beta = \Delta\lambda / \Delta\iota$ [nm / mA] is not documented. In order to measure the laser wavelength with varying current I could not use a conventional spectrometer since the resolution is limited to several nanometers. Instead, we designed a Michelson-Interferometer-like setup to determine the function of wavelength over current (fig. C3.2). The setup allows us to record the intensity of the light arriving at photodetector D while tuning the current i of the DFB laser diode L.

The light is split by the beamsplitter B into two different path which both start at the laser diode L and end at the photodetector D. The light takes either one of these two possible paths. Both paths are identical except for the parts associated with a pathlength x_v and x_h. For one complete light-path from source to detector, each of those path lengths are traversed twice. At the photodetector D we record the intensity T^2 as a result of the interference of the two different waves:

$$TT^* = (e^{ik2x_h} + e^{ik2x_v}) \cdot (e^{-ik2x_h} + e^{-1k2x_v}) \quad \text{Eq (C3.1)}$$

$$TT^* = 2 + 2\cos 2k(x_h - x_v) \quad \text{Eq (C3.2)}$$

If we record the intensity as a function of current we should observe maximas at:

$$k(x_h - x_v) = \pi \quad \text{Eq (C3.3)}$$

The distance between two neighboring maximas at $k_1=2\pi/\lambda_1$ and $k_2=2\pi/\lambda_2$ is:

$$k_2 - k_1 = 2\pi(\frac{1}{\lambda_2} - \frac{1}{\lambda_1}) = 2\pi\frac{\lambda_1 - \lambda_2}{\lambda_1\lambda_2} \cong 2\pi\frac{\lambda_1 - \lambda_2}{\lambda_0^2} \quad \text{Eq (C3.4)}$$

with λ_0 being the nominal lasing wavelength.

The wavelength tuning between two neighboring maximas $\Delta\lambda=\lambda_1-\lambda_2$ can thus be calculated as:

$$\Delta\lambda = \frac{\lambda_0^2}{2(x_h - x_v)} \quad \text{Eq (C3.5)}$$

For the Mitsubishi DFB laser diode ML776H11F used throughout this thesis operating at $\lambda_0 = 1312$ nm I measured the following tuning data:

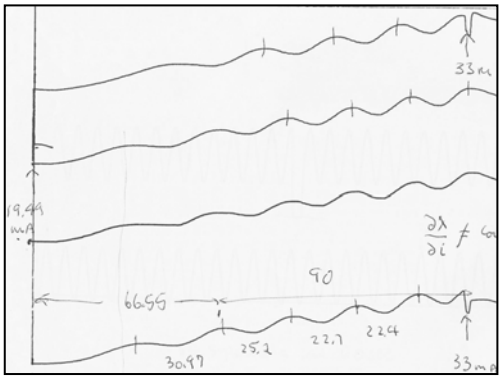

Figure C3.3: Data taken with setup in fig. C3.2. Vertical axis shows varying light intensity due to interference measured with the photodetector while scanning the operating current of the laser diode (horizontal axis) from 19.49 mA to 33 mA.

Fig. C3.3 shows the intensity scan when varying the laser current (between the arrows) from $\iota = 19.49$ mA to 33 mA ($\Delta\iota = 33 - 19.49$). From the graph I determine the distance between one maxima and its neighbor as 1.93 mA. We see, that the tuning coefficient $\beta = \Delta\lambda / \Delta\iota$ is not exactly constant. With good approximation, however, we determine the tuning coefficient as ($x_h = 101.3$ mm, $x_v = 53.7$ mm, $\lambda_0 = 1300$ nm):

$\beta = 0.01$ nm / mA. Eq (C3.6)

C4 - Hydrofluoric Acid Erosion of the Optical Fiber

In order to evanescently couple the light which is propagating down the core of an optical fiber into the microsphere resonator I have to access its evanescent field. The light is propagated in the core of the fiber and by removing the surrounding cladding material I expose the evanescent field. In the following, I will erode the fiber into its core by hydrofluoric acid erosion.

An optical fiber is essentially made of silica (silicon dioxide, SiO_2) which forms an amorphous material. The amorphous crystal is terminated at its surface by silanol groups, SiOH. Silica is almost non-soluble in water. When exposed to hydrofluoric acid (HF), however, the silanol group is attacked by the fluoric acid:

$SiOH + HF \rightarrow Si\text{-}F + H_2O$

Also the silica bond is broken by reaction with HF:

Si-O-Si-O- + HF → Si-F + HO-Si-O-

As soon as all 4 oxygens bound to a Si atom are replaced by 4 fluorides, SiF_4 dissolves in diluted HF as a SiF_6^{2-} complex (Iler, 1955).

Successive removal of silanol groups from the silica surface results in a well known etching process: hydrofluoric acid erosion of silica. The etching rates are especially high in aqueous HF solutions.

For this purposes, I would like to remove the low-refractive cladding material of an optical fiber by hydrofluoric acid erosion.

I first remove the polymer sheet protecting the silica part of the smf-28 fiber from bending breaks. The polymer can be dissolved in methylenedichloride ($Cl\text{-}CH_2\text{-}Cl$, dichloromethylene). I just have to dip the portion of the fiber for a few minutes in the dicholormethylene solution. Using a Kimwipe, I can then carefully peel off the polymer sheeting over a limited length of the fiber.

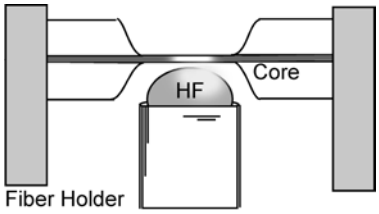

Figure C4.1: Experimental setup for hydrofluoric acid etching of the optical fiber.

I then fix the fiber on a stage made of two fiber holders. The fiber is typically imaged on a microscope with a 40x objective. A drop of 25% hydrofluoric acid solution on an Eppendorf tube is positioned on a stage below the fiber (fig. C4.1). The etching process is monitored on a CCD camera looking down onto the fiber immersed in the acid drop.

After ~ 4 hours I have removed all of the cladding and left with 6.6 μm diameter of high-refractive index core material. From the previous discussions we understand that I have to

taper the core diameter preferably to an even smaller optimal diameter which allows most efficient (in the best case critical) evanescent coupling to the microsphere.

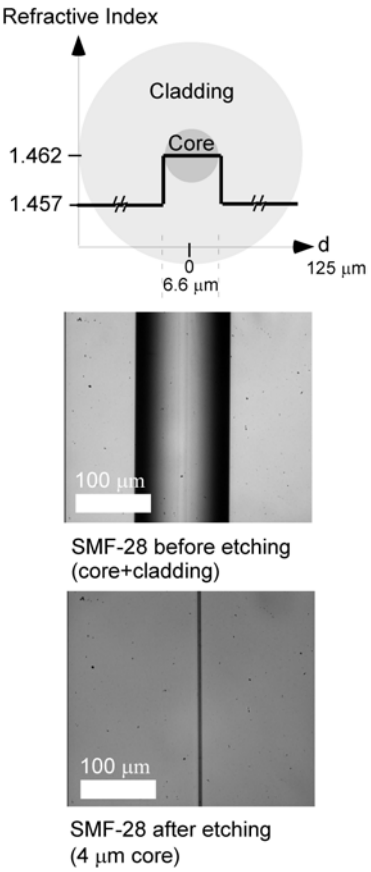

Figure C4.2: Hydrofluoric acid assisted thinning of a single mode optical fiber (smf-28). The initial fiber diameter of 125 μm is etched down to a final diameter of ~ 4 μm over a time course of ~ 4.5 hours.

Experimentally, I determined 4 +/- 0.2 μm as a convenient core diameter allowing high coupling efficiencies without making the fiber too vulnerable to breakage (fig. C4.2). I stop the etching process by neutralizing the hydrofluoric acid solution with a 1 M $NaHCO_3$ (sodiumbicarbonate) solution. I then briefly dip the eroded fiber in distilled water to remove remaining ions. It has been recently demonstrated (Tong, 2003) that even subwavelength-diameter silica wires can be fabricated and used for low-loss optical wave guiding.

Notice that the now tapered fiber with a diameter of 4 μm has a refractive index of 1.462, larger than that of air (1.0) and water (1.33). If I am operating the tapered fiber in these environments it is as if I have replaced the low-refractive silica cladding with an even lower refractive index air- or water cladding. Earlier optical fibers were in fact just core material operated in air. The light can still propagated along the new core-air or core-water boundary by total internal reflection.

A calculation of the new mode chart of the silica core-water system shows, that I can expect the tapered region now to become multimode over the short stretch of the thinned fiber (fig. C4.3; in this case d/lambda = 4 μm/1.3 μm = 3.08; Black, 1986; Boucouvalas, 1986; Love, 1991; Yariv, 1997). The multimode nature of the tapered region might lead to a limited mixing of modes (TE and TM).

The calculation also shows that the evanescent field of the silica-core-water waveguide now extends further into the surrounding which will facilitate coupling to micropshere modes (fig. C4.3).

Figure C4.3: Mode chart and evanescent field decay length for a flat waveguide of diameter d operated at λ=1300 nm with n = 1.462 in water (n=1.33). Such a flat waveguide is similar to the tapered region of the smf-28 fiber. Compare with fig. C2.5.2 and fig. C.2.5.3.

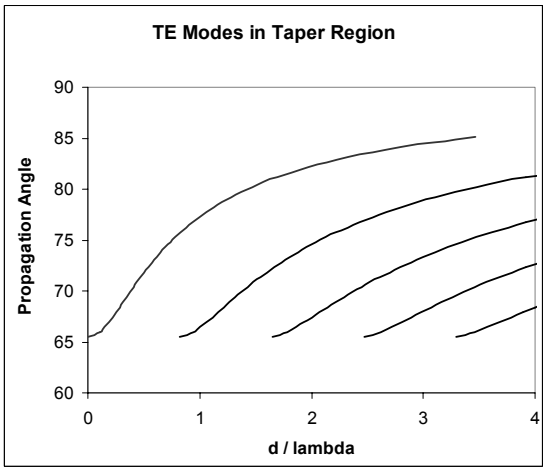

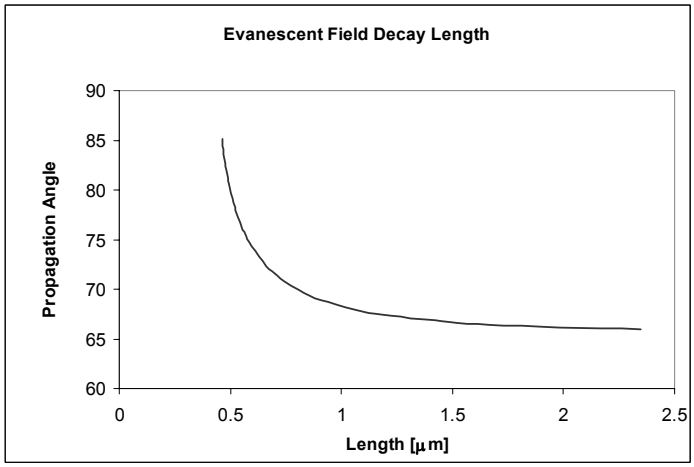

C5 Fabrication of Microsphere Resonators

Throughout this thesis, I use microsphere resonators fabricated from an optical smf-28 fiber chuck.

Figure C5.1: Fabrication of a microsphere resonator by melting of an optical fiber in a hot butane/nitrous oxide flame.

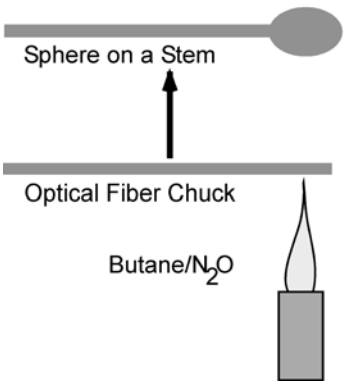

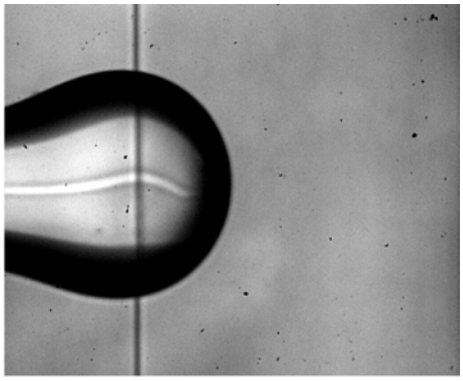

Silica is a material with a fairly high melting temperature of 2876ºF. A conventional butane flame of a Bunsen burner only reaches a maximum temperature of ~ 1500 ºF. In order to melt silica I have to use a butane/nitrosoxide (N_2O) gas mixture. The butane/N_2O flame of a microtorch can reach temperatures above 3000 ºF in the white cone of the flame. I use this flame to melt the tip of a conventional smf-28 fiber. Surface tension will draw the melted fiber into a spheroidal object which I will refer to as a microsphere throughout this thesis. After melting of the fiber tip I have fabricated a sphere on a stem ("lollipop"). The stem makes it very easy to manipulate and position the microsphere using conventional xyz-stages. Fig. C5.1 shows the sphere fabrication method. The right image shows positioning of a microsphere on a stem in contact with the eroded optical fiber. Microspheres can be fabricated in diameters ranging from 120 μm to > 500 μm depending on the amount of melted fiber material. Smaller diameters <150 μm require a previous pulling/thinning of the initial 125 μm diameter smf-28 fiber into a tapered fiber with smaller starting diameter. A similar microsphere fabrication procedure using a CO_2 laser to melt the silica fiber is described elsewhere (Cai, 2001).

C6 Experimental Results: Resonances in Air and Water

For the first experiment, I will fabricate a microsphere (on a stem) of ~ 400 μm diameter. Holding on to the stem I then mount the microsphere on a xyz-stage. I position the sphere in contact with the eroded fiber part as shown in fig. C5.1. Previously I demonstrated that a DFB laser diode can be tuned over a narrow spectral width by ramping the diode current. The tuning coefficient is $\beta = 0.01$ nm/mA.

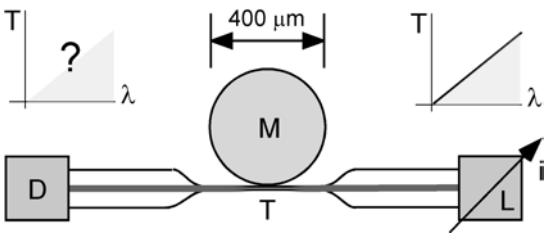

Figure C6.1: First experiment: Coupling of a microsphere ~ 400μm diameter to the tapered fiber in air. What will the transmission spectrum of the microsphere-fiber system look like (symbolized by ?).

I measure a linear transmission spectrum through the fiber if there is no microsphere resonator present (right spectrum shown in fig. C6.1). What happens to the spectrum if I couple a microsphere by mechanical contact to the eroded fiber part?

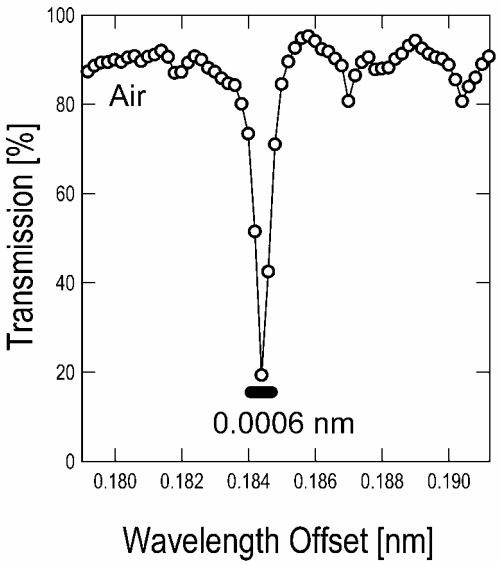

If I now modulate the laser diode current source with a sawtooth shaped function I will be able to periodically record the transmission detected by the photodiode D at each of the scanned wavelengths.

Figure C6.2: Microsphere resonance in air observed as narrow, Lorentzian shaped dip in the transmission spectrum recorded by the photodiode over a scan range of only 1 mA (corresponding to a spectral width of 0.01 nm).Notice the narrow linewidth of only 0.0006nm.

Here, I ramp the current by only 1 mA (corresponding spectral width of 0.01 nm). I identify a transmission dip in the spectrum (fig. C6.2). The transmission dip corresponds to a resonant mode excited in the microsphere. For the microsphere in air, I measure a resonance line width as narrow as 0.0006 nm. Already with this simple setup I reach Qs as high as ~ 10^7.

Figure C6.3: Microsphere transmission spectrum in water.

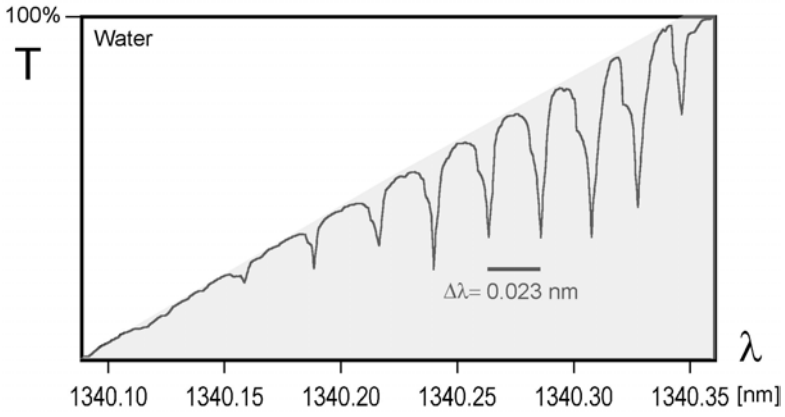

For future applications, I am more interested in measurements in water. For this purpose, I immerse the microsphere-fiber contact in a drop of distilled water again held on an eppendorf tube. This time I scan across the maximum spectral width of ~ 0.3 nm. I observe a nice periodic

spectrum of transmission dips (fig. C6.3). The distance between adjacent resonant dips is ~ 0.023 nm. The Q-factor in water is slightly lower due to overtone vibrational absorption of the resont IR light by H_2O. In water I typically measure Qs on the order of 2×10^6.

I experimentally determined the parameters for the coupled microsphere-waveguide system. These experiments lead to the development of a setup which will allow us to study the optical resonances upon perturbation with e.g. molecular particles. Before I proceed with my experiments I will try to explain the periodic structure of resonant modes I measured for the first experiment in water (fig. C6.3).

D Photonic Atom Model

The light orbit inside a microsphere resonator is governed by Maxwell's equations and can be precisely described by the derived Helmholtz formula (Hill, 1988). An asymptotic formula can be used to approximate the solutions of the resulting transcendental equation (Lam, 1992). This formula, however, is not very intuitive and in this section we will illustrate how Maxwell's equations can be rewritten as a Schrődinger-like equation similar to the well known wave equation describing the electron states in a hydrogen atom. Given a basic understanding of quantum mechanics, this *photonic atom* analog will allow us to understand the quantization of the angular momentum of an orbiting photon. The quantization of the angular momentum will provide us with an explanation of the sensing principle by the principle of conservation of optical size. The azimuthal splitting of the angular momentum will explain the spectral density of photonic atom modes.

Furthermore, the photonic atom model provides us with an understanding of the evanescent field as the extension of the photon wave function into classically forbidden regions outside of the microsphere boundary. This extension of the evanescent field will be instrumental for detection of molecules and larger particles such as bacteria.

D1 Hydrogen Atom Analogy: A Schrődinger-like Equation

The reader might be interested in a more detailed presentation and derivation of the photonic atom model (Arnold, 2002).

The electric field confined in a non-charged, spherical cavity is described in wave optics by the Helmholtz equation which can be directly derived from Maxwell's equations:

$$\nabla^2 E + k^2 E = 0 \qquad \text{Eq (D1.1)}$$

E is the electric field, k = 2π n(r) / λ is the propagation constant and n(r) is the refractive index, r is the radial coordinate.

We remember the angular momentum and its quantization as a very important concept governing many properties of the hydrogen atom. We can introduce the angular momentum operator $\hat{L}$ in spherical coordinates as:

$$\hat{L} = -i(\vec{r}x\nabla) \qquad \text{Eq (D1.2)}$$

Then we can re-formulate the Laplacian Operator as:

$$\nabla^2 = \left(\frac{1}{r} \frac{\partial^2(r)}{\partial r^2} - \frac{\hat{L}^2}{r^2} \right) \qquad \text{Eq (D1.3)}$$

The Helmholtz equation (D1.1) now becomes

$$\left(\frac{1}{r} \frac{\partial^2(r)}{\partial r^2} - \frac{\hat{L}^2}{r^2} \right) E + k^2 E = 0 \qquad \text{Eq (D1.4)}$$

Again we use our knowledge from quantum mechanics of the hydrogen atom. The angular momentum operator along one (the symmetry) axis and the square of the angular momentum can be measured (defined) at the same time since both operators commute: $[\hat{L}^2, \hat{L}] = 0$. This allows us to guess a solution of E as $E = \hat{L}\Psi$. If we insert this solution into eq. (D1.4), we can write this equation in terms of the angular momentum operator:

$$\hat{L}\left[\frac{\partial^2(r\psi)}{\partial r^2} - \frac{\hat{L}^2(r\Psi)}{r^2} + k^2(r\Psi) \right] = 0 \qquad \text{Eq (D1.5)}$$

If we set the equation in the brackets equal to zero:

$$\left[\frac{\partial^2(r\psi)}{\partial r^2} - \frac{\hat{L}^2(r\Psi)}{r^2} + k^2(r\Psi) \right] = 0 \qquad \text{Eq (D1.6)}$$

we can rewrite this equation (D1.6) in the form of a Schrődinger-like equation. We remember that for a hydrogen atom, the spherical symmetry allows us to separate radial and angular dependencies. The angular solutions for a hydrogen atom are known as spherical harmonics $Y_{l,m}$, where l is the angular quantum number and m is the azimuthal

quantum number. With the photonic atom we are dealing with an identical symmetry. By analogy with the hydrogen atom we can deduce the solution as a function separable in radial Ψ_r and angular $Y_{l,m}$ components:

$$r\psi(r) = \Psi_r(r)Y_{l,m} \qquad \text{Eq (D1.7)}$$

We are dealing with a spherical symmetry for which the angular dependencies are described by spherical harmonics. We remember from quantum mechanics that for such spherical symmetries encountered in a hydrogen atom the squared angular momentum is quantized according to:

$$\hat{L}^2 \mathrm{Y}_{l,m} = l(l+1)\mathrm{Y}_{l,m} \qquad \text{Eq (D1.8)}$$

If we now add and subtract $k_0^2\psi_r$ from the left of equation (D1.8) we identify a Schrődinger-like equation for the radial dependence:

$$\frac{d^2\Psi_r}{dr^2} + \left\{k_0^2 - \left[k_0^2(1-n^2) + l(l+1)/r^2\right]\right\}\Psi_r = 0$$

Eq (D1.9)

By analogy with the Bohr atom (fig.D1.1), we find the effective "energy" to be k_0^2 and we identify the effective potential as:

$$V_{eff}(r;k_0,n,l) = k_0^2(1-n^2) + l(l+1)/r^2 \qquad \text{Eq (D1.10)}$$

We can now see why the photonic atom is only an analogy: the potential scales with the effective "energy" ω^2 (remember that the effective energy E for the photonic atom is k_0^2) and does NOT scale linearly with ω (as in the hydrogen atom).

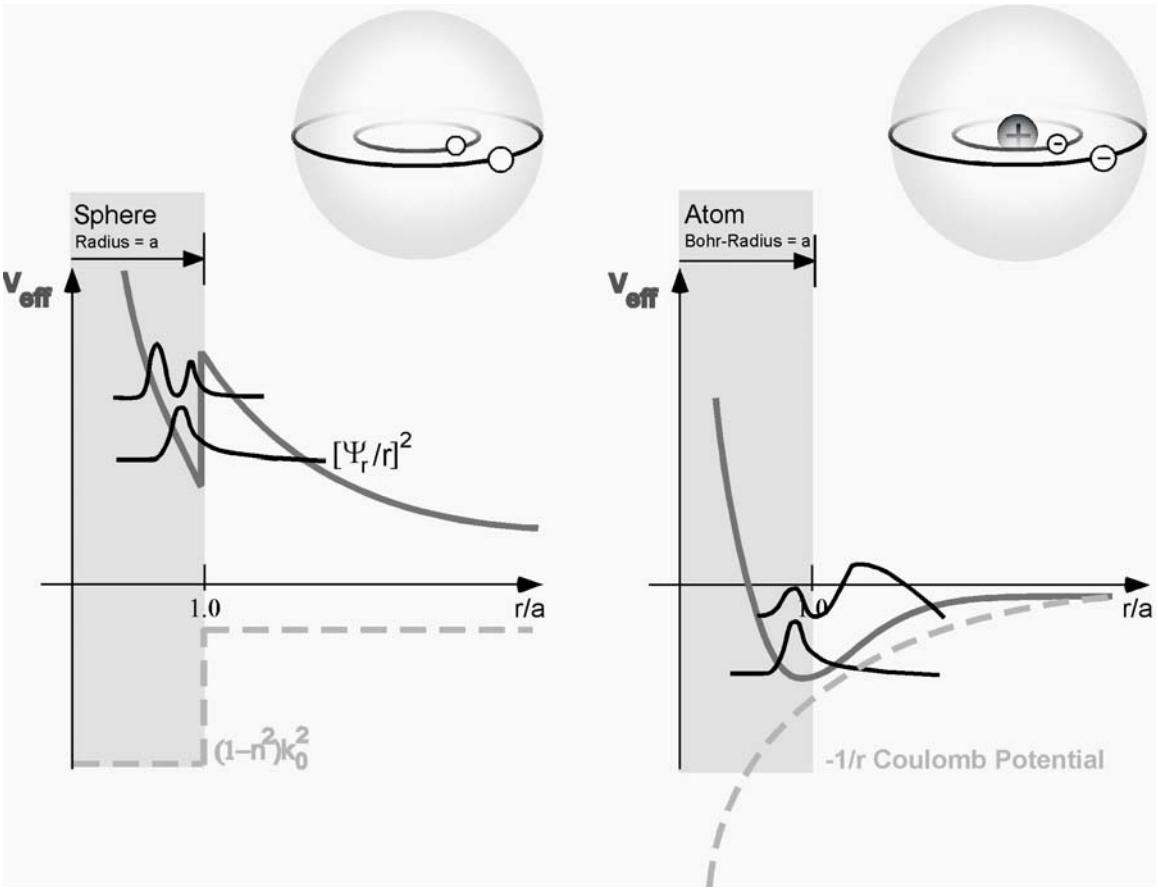

Figure D1.1: Analogy between a photonic atom and a Bohr atom. In the photonic atom the wavefunctions describing the photons are trapped in an effective potential well created at the refractive index boundary of sphere and surrounding medium. In a Bohr atom, the electrons are confined by a similar effective potential.

The photonic atom model illustrates nicely the trapping of a photon in a potential well similar to an electron in a Bohr atom. At the boundary of the dielectric sphere with high refractive index, a potential well confines the "wave function" of the photon to a caustic region just below the sphere surface. Fig. D1.1 shows the effective potential V_{eff} of the microsphere. Its offset at the boundary of the microsphere is due to the refractive index contrast with the surrounding medium as illustrated by the dashed potential. The wave function Ψ is depicted in black. Its radial solution is a spherical Bessel function. Table D1.1 summarizes the analogy between a photonic atom and a Bohr atom.

<table>
<tr><th>Photonic Atom</th><th></th><th>Bohr Atom</th></tr>
<tr><td>  </td><td></td><td>  </td></tr>
<tr><td>$\nabla^2\Psi + (V_{eff} - E)\Psi = 0$</td><td>“Schrődinger Equation”</td><td>$-\frac{\hbar}{2m}\nabla^2\Psi + (V_{eff} - E)\Psi = 0$</td></tr>
<tr><td colspan="3">Quantum Numbers
n = 1,2,3
l = 0,.., n
m = -l, …, +l</td></tr>
<tr><td>V_{eff} = “Refractive Index Contrast” + “Rotational E.”
$V_{eff}(r;k_0,n,l) = k_0^2(1-n^2) + l(l+1)/r^2$</td><td>Radial, Effective Potential</td><td>V_{eff} = Coulomb + Rotational Energy
$V_{eff} = \frac{-ze^2}{4\pi\varepsilon_0 r} + \frac{l(l+1)\hbar^2}{2\mu r^2}$</td></tr>
<tr><td>Bessel Function, n-1 nodes</td><td>Radial Solution</td><td>Laguerre Polynomial, n-1 nodes</td></tr>
<tr><td colspan="3">Angular Solution
Spherical Harmonic $Y_{l,m}$
 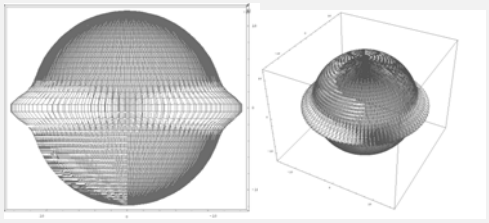 </td></tr>
<tr><td colspan="3">Quantization of Angular Momentum
$L = \hbar\sqrt{l(l+1)}$ $L_z = \hbar m$
 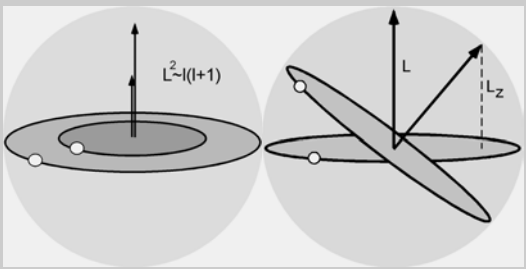 </td></tr>
</table>

Table D1.1: Summary of mathematical analogy between photonic atom and Bohr atom.

D2 Consequences of Angular Momentum Quantization

Quantization of L^2

In analogy to the Bohr atom, we calculated the quantization of the angular momentum in the photonic atom as:

$$L = \hbar\sqrt{l(l+1)} = \frac{hn}{\lambda} \qquad \text{Eq (D2.1)}$$

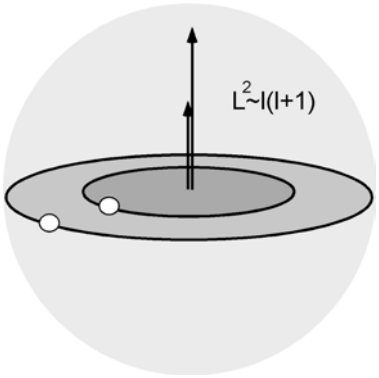

Figure D2.1: Quantization of the angular momentum in the photonic atom.

Only for resonant modes described by this quantization of momentum is there a substantial build up of energy in the potential well of the photonic atom, similar to the allowed electron orbits of the Bohr atom. Indeed we can show that the angular momentum number l is related to the integer number of wavelength that fit along one resonant light orbit. The angular momentum is defined as:

$$L = r \times p \qquad \text{Eq (D2.2)}$$

with the de Broglie wavelength which relates the wavelength to the impuls $p = h / \lambda$:

$$\frac{h}{2\pi}\sqrt{l(l+1)} = r \cdot \frac{hn}{\lambda} \qquad \text{Eq (D2.3)}$$

If we rearrange this equation we calculate for the circumference of a light orbit divided by the wavelength (= number of wavelength on a resonant orbit):

$$\frac{2\pi nr}{\lambda} = \sqrt{l(l+1)} \approx l \qquad \text{Eq (D2.4)}$$

Similarly as in the Bohr atom, we see that stable orbits are only encountered for waves, which return in phase. The wavenumber on one orbit is on the order of the angular quantum number l.

From equation (D2.4) we can deduce another important constant of the photonic atom: the optical size X:

$X = k_0 r = 2\pi r / \lambda$ Eq (D2.5)

As we see from eq. (D2.4) The optical size is constant for a given resonance of a specific l number. From this invariance of the optical size we can understand our sensing principle. If the optical size X is to remain constant, an additional layer increasing the effective radius a of the microsphere by δa will lead to a change δk_0 of the wavevector k_0:

$$\frac{\partial k_0}{k_0} = -\frac{\partial a}{a}$$ Eq (D2.6)

or in terms of wavelength change δλ:

$$\frac{\partial \lambda}{\lambda} = \frac{\partial a}{a}$$ Eq (D2.7)

From the quantization of the angular momentum, we should be able to calculate the distance between two modes l and l + 1 as previously measured from the recording of Lorentzian dips in the transmission spectrum. We can write eq. (D2.4) in terms of wavenumber k_0:

$$nk_0 a = 2\pi\sqrt{l(l+1)}$$ Eq (D2.8)

For large l the square root becomes approximately l. Then k_0 for a given l-number becomes:

$$k_{0,l} \cong \frac{l}{na}$$ Eq (D2.9)

The wavenumber of the resonance l+1 next to resonance l:

$$k_{0,l+1} = \frac{l+1}{na} \qquad \text{Eq (D2.10)}$$

Thus the difference in wavenumber δk between those neighboring resonances is:

$$\partial k_0 = k_{0,l+1} - k_0 = \frac{1}{na} \qquad \text{Eq (D2.11)}$$

The fractional wavenumber change for successive resonant modes thus equates:

$$\frac{\partial k_0}{k_0} \cong \frac{1}{l} \qquad \text{Eq (D2.12)}$$

with $k_0 = 2\pi / \lambda$ we calculate the fractional spacing of successive Lorentzian dips in our spectrum as:

$$\left|\frac{\Delta\lambda}{\lambda}\right| \approx \frac{1}{l} \qquad \text{Eq (D2.13)}$$

We already demonstrated that the l-number represents the number of wavelength on a first order resonant orbit. For a typical microsphere of ~200 μm radius, l = circumference / wavelength = 2π x 200 μm / 1.3 μm ~ 1000. The fractional resonance spacing should thus be on the order of:

$$\left|\frac{\Delta\lambda}{\lambda}\right| \approx \frac{1}{1000} = 10^{-3} \qquad \text{Eq (D2.14)}$$

In our transmission spectrum (measured at a wavelength λ=130$\tilde{0}$ nm), however, we find aproximatley 5 resonances over a spectral width of .3 nm, which gives us a measured fractional resonance spacing much smaller than so far predicted:

$$\left|\frac{\Delta\lambda}{\lambda}\right| \approx \frac{.3 \times nm/5}{1300nm} \approx 5 \times 10^{-5} \qquad \text{Eq (D2.15)}$$

We will explain this discrepancy in the following chapter. To explain this narrow spacing of microsphere resonances, we have to consider that the fabricated microspheres deviate from perfect spheres (fig. D2.6). This deformation leads to a further splitting and quantization of the angular momentum and thus in a smaller spacing of adjacent resonant modes.

Our mathematical approach will describe the distortion of the spherical shape by using a Legendre-Polynomial. Such an approach has been used to estimate the perturbative effect of spherical distortion on the width of microsphere resonances in Mie scattering (Lai, 1991). Such perturbations lift the spherical symmetry (Lai, 1990) as we will see. This leads to azimuthal mode splitting which could be used to discriminate isotropic from anisotropic stress acting on the microsphere (Ilchenko, 1998).

Azimuthal Quantization of Angular Momentum

As we know from the Bohr Atom, the L_z component of the angular momentum is quantized as

$$L_z = \hbar m \qquad \text{Eq (D2.16)}$$

with m being the azimuthal quantum number ranging from –l, …,0,…, +l.

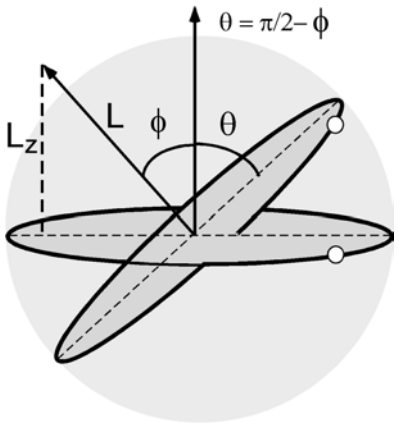

Figure D2.2: L_z component of the angular momentum L of a tilted orbit. Definition of angle θ and ϕ.

Since L_z is the projection of L on the axis of symmetry, the azimuthal L_z-splitting is associated with an angle ϕ between L_z and L and thus with a tilt of the orbit (fig. D2.2). For perfect spherical symmetry, the different azimuthal, tilted orbits are identical and associated with

the exact same energy and momentum. In the perfect spherical case, the azimuthal orbits are thus called degenerate. For each given l-number we can find 2l+1 degenerate azimuthal orbits in the hydrogen atom, each associated with a m-number ranging from –l, …, 0, …, +l.

In our microsphere experiments, however, we are not dealing with perfectly symmetrical spheres. In fact, as we saw in chapter C5, the fabricated microspheres used throughout this thesis tend to be rather visibly prolate in shape. In a prolate microsphere, the radius of the cavity on the equator (where the light is orbiting) is smaller than the radius measured to one of the poles, north or south. Our microspheres are shaped like an egg rather then like the earth – the earth has an oblate shape: it bulges out on the equator due to its rotation around the earth axis in north-south direction.

We can describe a prolate deformation of our microspheres mathematically. By adding a second order Legendre polynomial P_2 to the radial function of a perfect circle we obtain a function describing a prolate, egg-shaped object (eq. (D2.17), fig. D2.3):

$$r(\theta) = a + \varepsilon P_2 = a + \frac{\varepsilon}{2}(3\cos^2\theta - 1) \qquad \text{Eq (D2.17)}$$

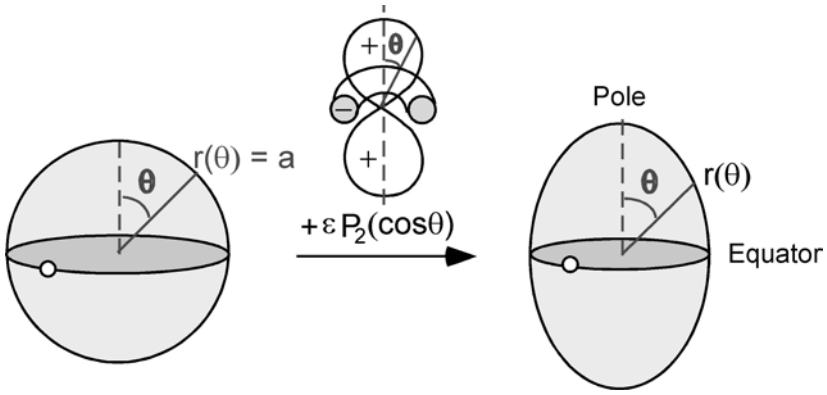

Figure D2.3: Description of the prolate shape of the microsphere resonators using a second order Legendre Polynomial P_2.

The second order Legendre Polynomial P_2 is well known to chemists: it describes the shape of a d-orbital. Since our microspheres are prolate, we are always dealing with a positive ellipticity ε.

Figure D2.4: Prolate microsphere resonators have a smaller equatorial diameter r_e and a larger polar diameter r_p.

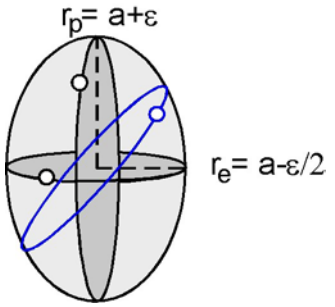

We can see that the additional term εP_2 subtracts $\varepsilon / 2$ from the original radius a around the equator (fig. D2.4, r_e). Around the poles, the radius a now becomes larger: $r_p = a + \varepsilon$.

In our case (fig. D2.2) we are evaluating the angular momentum at the radius r of the (elliptical) light orbit at angle $\phi = \pi / 2 - \theta$. We can rewrite equation (D2.17) as:

$$r(\phi) = a + \varepsilon P_2 = a + \frac{\varepsilon}{2}(3\cos^2\left(\frac{\pi}{2} - \phi\right) - 1) = a + \frac{\varepsilon}{2}(3\sin^2\phi - 1)$$

Eq (D2.18)

The angle θ of the tilted light orbit can be expressed in terms of quantization of the angular momentum L (fig. D2.2):

$$\cos(\phi) = \frac{L_z}{L} = \frac{m}{\sqrt{l(l+1)}}$$

Eq (D2.19)

We see that for m = l, the light orbits around the equator on a circular orbit for an angle $\phi = 0$ ($\theta = \pi / 2$). For any other azimuthal angle ϕ (θ), the light orbit describes a tilted, elliptical orbit.

In general, a light orbit in a prolate sphere can be identified by two quantum numbers: l and m. From fig. D2.4 we see that for a given l but varying m-number the associated orbital paths differ in circumference C_m. The smallest orbital path, which in this case describes a circular trajectory, lies on the equator for l = m: $C_{m=l}$ with associated radius r_e. Any other orbital circumference C_m will be larger and elliptical. The largest circumference can be found for the polar orbit with associated polar radius r_p. Again we use the argument of conservation of optical size: For a given resonance the number of wavelength is identified by the l-number. Azimuthal splitting in a prolate microsphere,

however, leads to different, tilted orbital path for this given l-number. For these azimuthal light orbits, the orbital paths C_m are all longer in circumference as compared to the equatorial orbit $C_{m=l}$. The wavelength associated with each of those azimuthal modes will thus be slightly larger in order to accommodate the same wave number given by the angular quantum number l.

We can calculate this fractional change in wavelength $\Delta\lambda$ from the fractional change in circumference:

$$\frac{\Delta\lambda}{\lambda} = \frac{C_m - C_{m=l}}{C_{m=l}} \qquad \text{Eq (D2.20)}$$

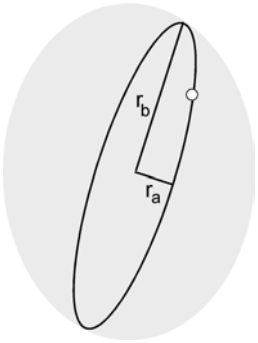

Figure D2.5: Radii r_a and r_b associated with a tilted light orbit.

All orbits are generally elliptical and their circumference can be approximated by (fig. D2.5):

$$C_l = \pi (r_a + r_b) \qquad \text{Eq (D2.21)}$$

Calculation of equatorial circumference $C_{m=l}$:

This is the only circular case where $r_a = r_b = r(\phi = 0) = a - \varepsilon / 2$:

$$C_{m=l} = \pi (2a - \varepsilon) \qquad \text{Eq (D2.22)}$$

Calculation of circumference C_m associated with tilted orbits:

r_a still remains the same as for the circular, equatorial orbit $C_{m=l}$:

$$r_a = r(\phi = 0) = a - \varepsilon / 2 \qquad \text{Eq (D2.23)}$$

r_b is provided by equation (D2.18) which describes the prolate shape of the distorted microsphere evaluated at the angle ϕ:

$$r(\phi) = a + \frac{\varepsilon}{2}(3\sin^2\phi - 1) \qquad \text{Eq (D2.24)}$$

The circumference C_m is thus calculated as:

$$C_m = \left[a - \frac{\varepsilon}{2} + a + \frac{\varepsilon}{2}\left(3\sin^2\phi - 1\right)\right]\pi = \left[2a - \varepsilon + \frac{3\varepsilon}{2}\sin^2\phi \right]\pi$$

Eq (D2.25)

with $\sin^2\phi = 1 - \cos^2\phi$ and with eq. (D2.19) we calculate C_m in terms of l and m number as:

$$C_m = \left[2a - \varepsilon + \frac{3\varepsilon}{2}\left(1 - \frac{m^2}{l(l+1)}\right)\right]\pi \qquad \text{Eq (D2.26)}$$

With eq. (D2.22) and eq. (D2.26) the fractional wavelength change $\Delta\lambda/\lambda$ is calculated as:

$$\frac{\Delta\lambda}{\lambda} = \frac{\Delta C}{C} = \frac{C_m - C_{m=l}}{C_{m=l}} = \frac{\frac{3\varepsilon}{2}\left(1 - \frac{m^2}{l(l+1)}\right)}{\left(2a - \varepsilon\right)} \cong \frac{3}{4}\frac{\varepsilon}{a}\left(1 - \frac{m^2}{l(l+1)}\right)$$

Eq (D2.27)

For a detailed derivation of this formula please refer to (Ching, 1996).

In our example the polar radius r_p and the equatorial radius r_e of the prolate microsphere is related to our ellipticity parameter ε (fig. D2.4) as:

$$r_p - r_e = \frac{3}{2}\varepsilon$$

Eq (D2.28)

which gives us the convenient definition of our *eccentricity ε.* For a perfect sphere the eccentricity ε = 0. For ε > 0 the object resembles a prolate egg, for ε >> 0 the shape is more rodlike and for very large ε the shape becomes more and more cylindrical.

We can now calculate the fractional spacing of neighboring azimuthal resonant modes in a prolate microsphere as:

$$\partial\left(\frac{\Delta\lambda}{\lambda}\right)=\frac{3}{4}\frac{\varepsilon}{a}\frac{2m\partial m}{l(l+1)} \qquad \text{Eq (D2.29)}$$

For direct neighboring modes (δm = 1) of light of a wavelength λ = 1.3 μm, close to the equator of the prolate microsphere (m = l) with an equatorial radius a = 200 μm (and thus number of wavelength on equatorial orbit l = 1000) we measured the fractional change as small as:

$$\partial\left(\frac{\Delta\lambda}{\lambda}\right)=\frac{3}{4}\frac{\varepsilon}{a}\frac{2m\partial m}{l(l+1)}=5\times10^{-5} \qquad \text{Eq (D2.30)}$$

From this fractional spacing we calculate an eccentricity ε of 2% which agrees well with the prolate shape of our microspheres shown in fig. D2.6. The typical eccentricity of microspheres fabricated in this thesis range between 2 - 3%. An eccentricity of 2% means that $\varepsilon = 2/3\ (r_p - r_e) = 0.02$ or $r_p / r_e = 1.03$ (fig. D2.6).

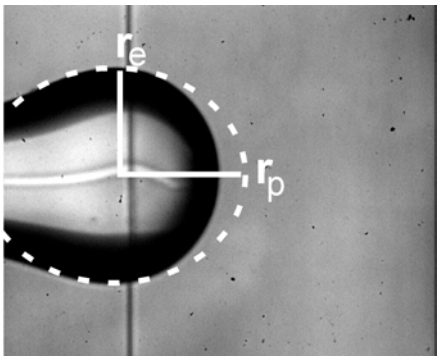

Figure D2.6: Image of a fabricated, prolate microspheres used throughout the thesis. Ratio of r_p/r_e is exaggerated in the illustration (actual $r_p / r_e \sim 1.03$).

To summarize: the reason why we detect resonances in form of transmission dips over a spectrum as narrow as .3 nm is due to the azimuthal splitting of the m-modes in the prolate microsphere. The "fence" structure of the resonant modes becomes much denser in prolate microcavities as compared to ideal spherical microspheres. Due to the slight prolate deformation of our microspheres we were able to use the small tunable range of a DFB laser to successfully detect several resonant dips corresponding to different, non-degenerate azimuthal modes.

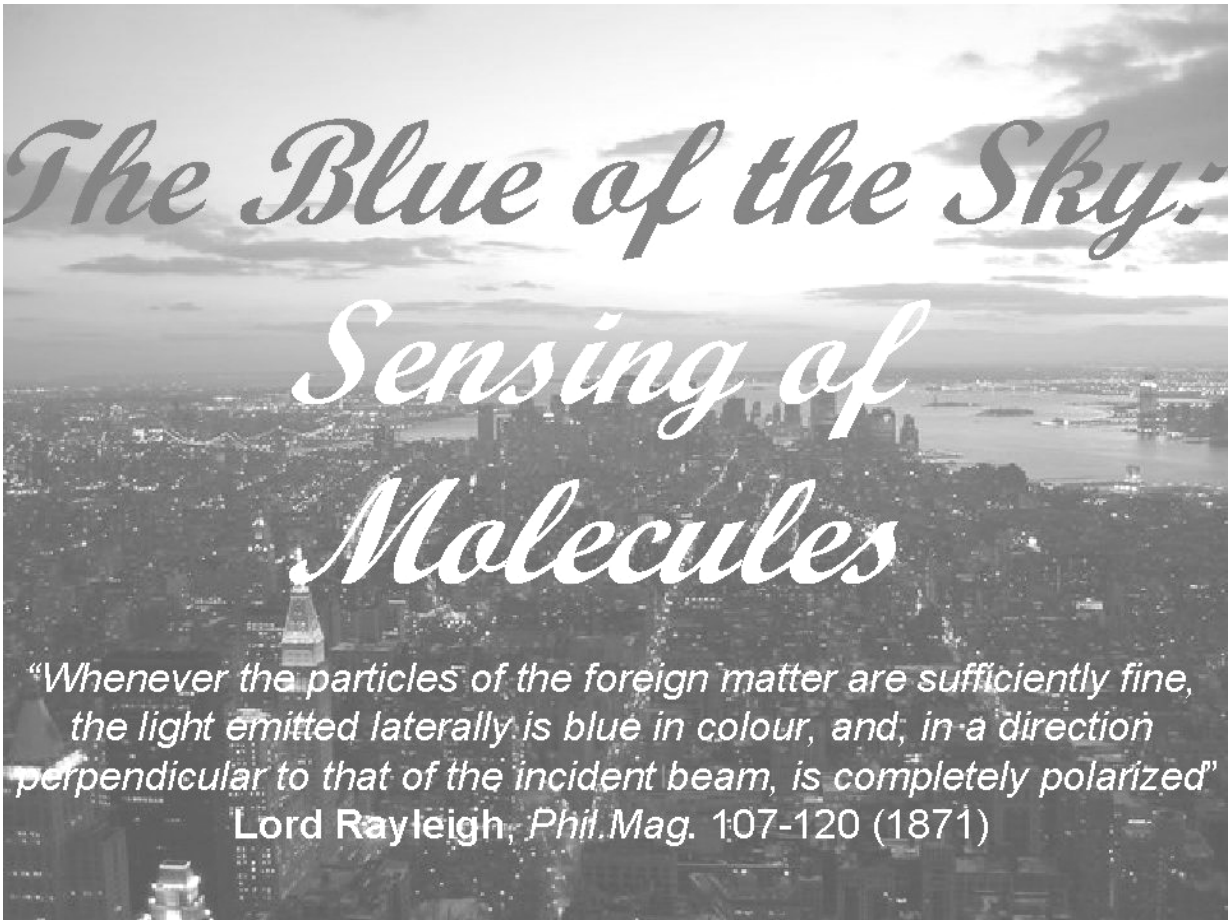
The Blue of the Sky:
Sensing of
Molecules
"Whenever the particles of the foreign matter are sufficiently fine, the light emitted laterally is blue in colour, and, in a direction perpendicular to that of the incident beam, is completely polarized"
Lord Rayleigh, Phil.Mag. 107-120 (1871)

E Molecular Perturbation of Microsphere Resonances: Protein Monolayer Adsorption

The contents of this chapter have been published (Vollmer, 2002).

E1 – Experimental Setup for Molecular Perturbation Detection

Biomaterials and their molecular components are usually studied in their native, aqueous environment for which they were designed by evolution on our blue planet.

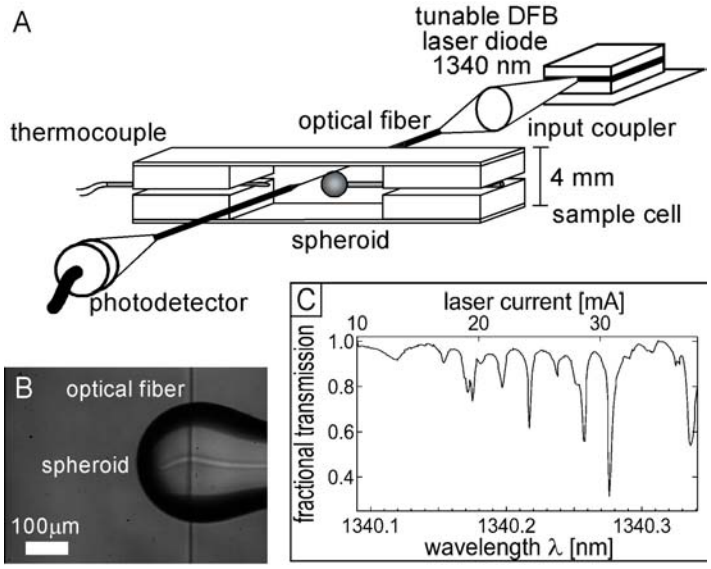

Figure E1.1: **A** - Experimental setup to study molecular perturbation of microsphere resonances. **B** – Image of the microsphere-fiber contact. **C** – Transmission spectrum showing Lorentzian-dips corresponding to microsphere resonances.

In order to study diverse functions of biomolecules such as molecular recognition, I attempt to modify the setup with a sample cell that is able to accommodate a water based sample volume. Fig. E1.1 - A shows the modified device: two glass plates (objective holders), separated by two silicone rubber pads are assembled around the microsphere-fiber contact forming an 'open' sample cell. The void between the two glass plates can be filled with an aqueous buffer solution: Glass-water surface tension holds a 1 ml liquid-volume in place. The sample cell is completely filled with the buffer solution immersing the microsphere-waveguide system in the desired aqueous environment. Furthermore, I place a thermocouple temperature sensor in close proximity to the microsphere. I will have to ensure a constant temperature for my biomolecular experiments since temperature fluctuations can impact on the resonant modes as well as on the function of the biomolecules themselves. Another important modification which is not illustrated in

fig. E1.1 - A is the optical isolator located between laser cavity and input coupler at the front end of the fiber. Without isolating the optical components from the coherent light source I do observe minor resonant coupling effects caused by back reflection of light into the laser cavity. Such back reflection can originate from the relections on the window of the photodetector. A microsocope (Axioscope) images the microsphere-waveguide system from above (fig. E1.1 - B). A typical transmission spectrum is shown in fig. E1.1 – C. Notice that the Lorentzian-dips are not always as nicely periodically spaced as discussed for an ideal example in Chapter C. This is due to fiber-sphere orientation and the particular local microsphere shape at the microsphere-waveguide contact.

The smf-28 optical fiber used throughout my experiments is embedded in a glass capillary tube that is fused to the front end of the fiber which is facing the input coupler. The capillary tube ended fiber is used for input coupling. The capillary tube is beveled at an angle of 8°, which further minimizes any back reflections into the laser cavity. The capillary tube is mounted on a standard single mode fiber coupler. An appropriate, low NA lens is used to focus the infrared light into the acceptance cone of the single mode fiber. Coupling efficiencies are ~ 2% (80 μWatt out of total 5 mW laser diode output) which is more than enough for my experiments.

As discussed in chapter B, I expect molecules in the sample solution to diffuse and bind to the microsphere surface and perturb the microsphere resonance by a sensitive red shift of the resonance wavelength. To detect the resonance wavelength shift caused by bound biomolecules I have to design a data acquisition routine (Labview) that reads out the photodetector recording of the transmission for every wavelength of the current tunable DFB laser source. The program also has to identify the resonance positions in the digitally recorded transmission spectrum. The resonance positions are determined by locating their minima using a parabolic minimum fit. The following diagram illustrates the working principle of my data-acquisition routine (fig. E1.2):

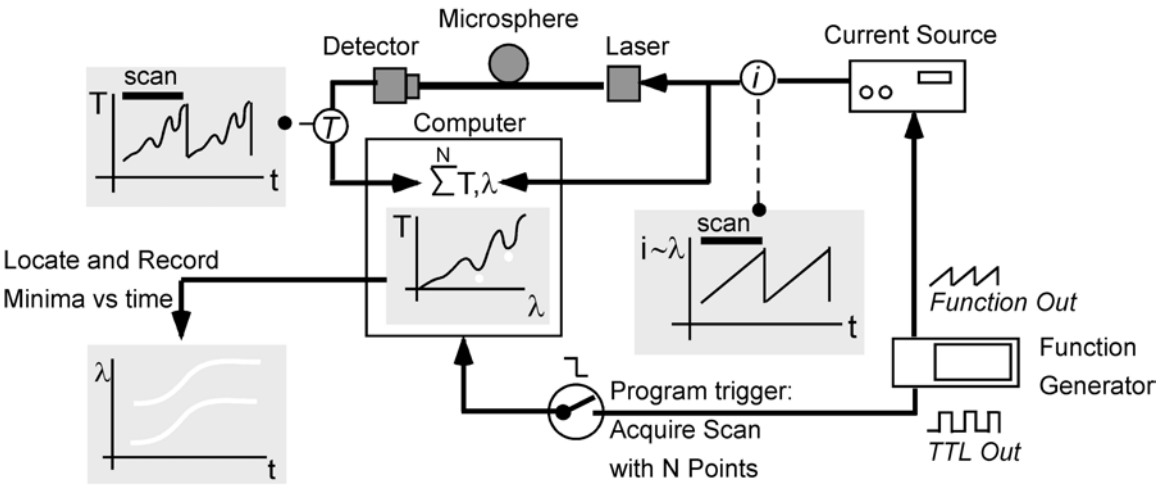

Figure E1.2: Data acquisition flow chart. The transmission spectrum is periodically scanned by a saw-tooth shape function. A Labview program locates and tracks a resonance position by a parabolic minimum fit of the Lorentzian-dip.

An improved version of this original program has been developed together with Dieter Braun. The new program version is able to track all given resonances. The spectra, resonance positions, Qs and temperature data are stored in a defined data format. A second program has been developed which analyzes the stored data.

A function generator is used to modulate the laser diode current source with a saw-tooth shaped, periodic wave form. It is important to modulate the laser diode current periodically to achieve a constant tuning of $\beta = 0.01$ nm/mA as determined previously. The tuning coefficient has been verified using a wavemeter. At all times, the laser is held at a constant temperature (about room temperature) with Peltier elements located in the laser diode mount and controlled by a constant temperature controller.

The Labview program is triggered by the falling edge of the TTL signal from the same function generator. After the falling-edge TTL trigger, the program acquires one complete scan (one saw-tooth) of the transmission spectrum. Usually 1000 points are used to record the transmission intensities and their corresponding wavelengths across a scan-range of $\Delta\lambda \sim 0.4$ nm (corresponding to a maximal current tuning range of the DFB laser diode ranging from 0 to 40 mA). The resolution of the scan is typically $\sim 0.4 \times 10^{-3}$ nm/point (sometimes higher, depending on the experiment). The maximum

achievable resolution is limited by the digital noise of the DAQ card and is about 0.4×10^{-6} nm.

After each complete scan, the program locates the minima in the acquired, digital transmission spectrum with a parabolic minimum fit using typically 11 points. The resonance positions are then saved together with a timestamp generated by the internal computer clock. The output of resonance position (in wavelength units) versus time is displayed as a trace on the computer screen. The program is able to track all resonances detected in the transmission spectrum simultaneously (~ 14 resonance positions in fig. E1.1 - C). The data acquisition using a 500 MHz PC limits the temporal resolution to about 1 kHz. Usual experiments are performed at 100 Hz. With the oscilloscope as an analog recorder of the spectra (thereby bypassing the computer), I determined the maximum temporal resolution of my microsphere-waveguide system as 80 kHz, limited by the response time of the photodetector and DFB laser.

On every scan, the thermocouple is directly read out with the DAQ board that is used to acquire the photodetector transmission data. The temperatures and their timestamps are saved together with the resonance positions and then displayed on a separate graph on the computer screen.

E1.1 List of Materials in Chapter E

Component	Manufacturer	Description
Chemicals	Sigma Aldrich, WI	Hydrofluoric acid, ethanol etc.
Data Acquisition Card, PCI-6036E	National Instruments, TX	12 Bit data acquisition card
DFB Laser Diode ML776H11F	Mitsubishi, Japan	Current tunable infrared source, 1312 nm nominal wavelength, 5 mW
Function Generator 33102A	Hewlett Packard	Provides saw-tooth current ramp
Labview	National Instruments, TX	Labview programming language
Laser Diode Mount LDM-4407	ILX Lightwave, MT	Laser diode mount, Peltier element controlled, constant temperature
Microscope	Zeiss Axioskope, Germany	Zeiss microscope, modified to accommodate sensor setup (object table removed etc.) Standard objectives: 6x, 20x, 40x
Optical Isolator	Optics For Research (OFR)	Optical isolator based on Faraday effect
Photodetector PDA400	Thorlabs, NJ	InGaAsP infrared photodetector
Silicone rubber Pads	McCarr-Master, NJ	Silicone rubber slab, ~ 2 mm thick
Single Mode Fiber Coupler F-1015 LD	Newport, CA	Fiber coupler for laser diodes
SMF-28 fiber with Capillary Tube on one end	Canadian Instrumentation&Research, Canada	Single Mode infrared fiber, terminated in 8° beveled capillary tube

Temperature Controller for Laser Diode Mount	ILX Lightwave, MT	Temperature controller for Peltier elements in laser diode mount
Thermocouple	Omega, NJ	Temperature sensor
Thermocouple Probe 5TC-GG-K-30-36 + Amplifier	Omega, NJ	Tungsten-constantan thermocouple to measure sample temperature
Tunable Current Source for Laser Diode Mount LDX-3525	ILX Lightwave, MT	Laser diode current source, external modulation up to 1 MHz possible
Wavemeter WA-1150	Burleigh, Canada	Wavemeter to confirm laser tuning coefficient $\beta = 0.01$ nm/mA

E2 – Bovine Serum Albumin

To demonstrate the anticipated frequency shift due to molecular adsorbents on the microsphere surface I choose a typical protein as a first test adsorbent. I choose a protein abundant in the blood serum: serum albumin. Its main physiological function is as a carrier of lipid molecules. For my experiment I will use the bovine-form of the serum albumin (BSA), which is almost identical in sequence and structure to the human homologue (human serum albumin, HSA).

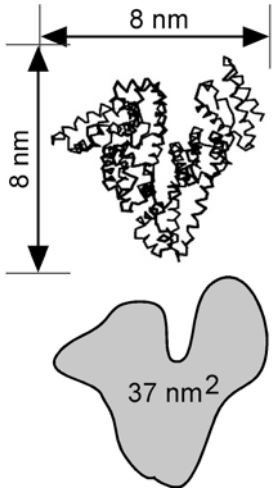

Figure E2.1: X-ray structure of BSA. The planar projection of the largest area is 37 nm^2.

The X-ray structure of HSA has been determined: HSA (as well as BSA) is a heart shaped protein of ~ 66 kD molecular weight with a diameter of about 8 nm along its longest axis (fig. E2.1). The largest areal projection of BSA is ~ 37 nm^2. The isoelectric point is pI = 5.5. BSA is highly negatively charged in neutral (~ pH 7.4) aqueous environments.

I already mentioned the lipid binding function of BSA. For my experiment, I would like to use the binding properties of BSA for a purpose for which it was not designed for by nature: the binding to a silica surface. BSA by itself does not have a high affinity towards silica. To promote adsorption of the negatively charged protein to a silica surface I have to chemically condition the microsphere sensor surface as detailed below.

Another important feature of most proteins including BSA is their high refractive index. Proteins have a refractive index n ~ 1.5, only slightly larger than the refractive index of the silica microsphere (n = 1.46). Binding of a molecular BSA layer to the microsphere surface can be viewed as an increase of the effective radius of the microsphere by additional mass loading of a material with similar optical properties as silica. This

additional mass-loading should lead to a red shift of the resonance wavelength as explained in Chapter B, fig. B5.1 by an increase of the effective radius of the microsphere cavity.

E3 - Silanization of Silica Microspheres

Silica (glass) is an important material for chromatography in the chemical industry. Many chemical surface modification procedures of silica have been studied in great detail. For my experiment, I will use one of the most basic modification procedures: silanization.

I already explained that BSA is a highly negative charged molecule at neutral pH. Although many different forces are involved in surface adsorption of molecules and proteins in particular, it seems at least for proteins to be a rule of the thumb that Coulomb forces are the most important ones. Since BSA protein is negatively charged, I will attempt to introduce positive surface charges on the silica microsphere to facilitate BSA adsorption by attractive, electrostatic interactions.

Silanization of silica surfaces is a basic method which is used in surface chemistry to introduce all kinds of functional groups on glass surfaces. The general procedure can be outlined as follows:

The silica surface is first meticulously cleaned. This can be achieved in two different, basic ways:

a) **Use of an aggressive solvent**: The Silica surface is immersed in a highly oxidative 'Piranha' solution consisting of 70% sulfuric acid (fuming) and 30% hydrogen peroxide solution (aqueous, 25%, stabilized) for up to 10 minutes. (Careful: The powerful oxidative potential turns Piranha solution into an explosive when in contact with reductive 'firewood' such as organic solvents).

b) **Silica surfaces can be cleaned by oxygen plasma etching**. An oxygen plasma can be generated in vacuum chambers by static discharge in a halogen tube. This is a much more convenient, safer and cleaner procedure.

After the cleaning procedure, the silica surface is completely oxidized: all surface groups are transformed into hydrophilic silanol functionalities. Contact angles with water are now very small compared to angles of non-cleaned glass surfaces.

The silanol (SiOH) groups are then used to introduce new functional groups on the glass surface. A silane compound activated by the chemical group X and carrying a chemical function R will react with the surface-exposed silanol groups:

Surface-Si-OH + X-Si-R → Surface-Si-O-Si-R + XH

With this silanization procedure I am able to introduce almost any chemical function R on the surface. Examples for both X and R chemical groups are (notice however that not all of the listed groups X and R are stable on the same molecule as a R-Si-X compound):

X	**R**
Methoxy-: CH_3O-	Amino-: NH_3-
Ethoxy-: CH_3CH_2O-	Carboxy-: COOH-
Alkoxy in general	Sulfhydril: HS-
Chloro-: Cl-	Alkoxy in general
	Teflon (Polyfluoroalkyl-)

Depending on the choice of the chemical group R I can render the microsphere hydrophilic (either positively charged or negatively charged) or hydrophobic. For this application I will choose the widely used silane aminopropyltriethoxysilane (APTES). APTES carries a positively charged γ-amino group, which I would like to chemically immobilize on the silica surface. In a nucleophilic reaction, the silanol group of the silica surface will react with APTES forming a covalent Si-O-Si bond (fig. E3.2). The ethoxy-leaving group will appear as ethanol in the solvent. Since the reaction is most likely a type S_N1-reaction I can promote the reaction by using a polar, aprotic solvent such as DMF (dimethylformamide).

In general, I can perform the silanization of this silanol-silica surface under two appropriate conditions:

a) **Solvent phase silanization**: I can dissolve APTES in an appropriate solvent. Most appropriate seems DMF. However, some literature reports that water catalyzes this reaction, so many recommended solvent systems are water based such as a mixture of acetic acid and water or methanol and water (Zammatteo, 2000).

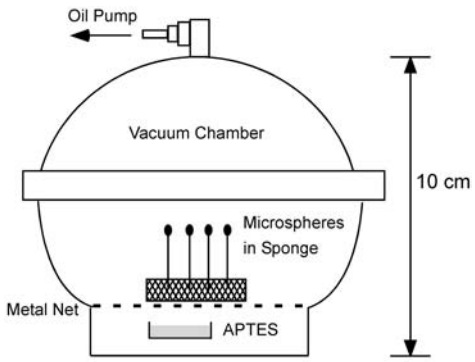

Figure E3.1: Experimental setup for vapor phase silanization.

b) **Vapor phase silanization**: APTES can be deposited directly on the microsphere surface by vapor deposition in a vacuum chamber (Choi, 2000). A conventional oil pump can generate a vacuum high enough to allow convenient silanization on a minute timescale. Fig. E3.1 illustrates the setup used throughout this thesis.

After surface-silanization, the reaction has to cure by removing remaining water in an oven at 120 ° for about 30'. The water which acted catalytically before has to be removed in order to form a stable, physico-chemical surface adsorbent.

Depending on the time of vapor deposition, one can even attempt to control the thickness of the aminosilane layer. In general, multiple layers are formed quickly within minutes using the vapor deposition method.

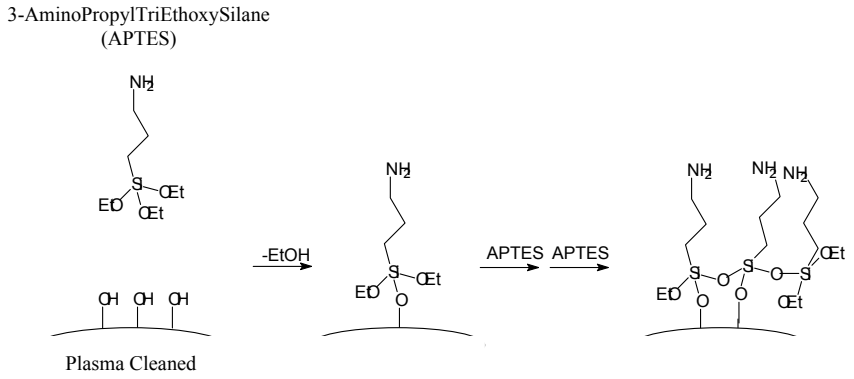

Figure E3.2: Surface chemistry of aminosilanization using APTES with oxidized silica surfaces.

In the following, however, I will always assume monolayer modification of the silica surface. Vapor deposition is my method of choice since it requires minimal sample handling: at no point the microsphere is in contact with any solution and thus contaminations are minimized. Fig. E3.2 summarizes the chemical surface modification procedure.

Methods and Chemicals in Chapter E3

Plasma cleaning of microspheres: Microspheres are positioned upright in a sponge-holder. The sponge holder is placed in the vacuum chamber of the plasma cleaner connected to a conventional oil pump. The microspheres are plasma etched for 4 minutes. The micropsheres in the sponge-holder are then immediately transferred to the vacuum chamber for vapor deposition.

Solvent base cleaning of micropsheres: Piranha solution (one-third hydrogen peroxide, 30%, and two-thirds sulfuric acid, 18M) is prepared in a 1 ml Eppendorf tube. Microspheres are exposed to the Piranha solution for 10 minutes, then left for 10 minutes in boiling distilled water and then dried in air at RT (room temperature).

Vapor phase silanization: Microspheres on a sponge-holder are placed in a small vacuum chamber (fig. E3.1). They rest on a copper net. Below the copper net I place 1 ml of the silanization solution (here: APTES). The vacuum char is closed and high vacuum grease seals the contact with the upper lid. A conventional oil pump is used to apply the vacuum. The vacuum sequence is the following:

A) 2 minute pump
B) 2 minute vapor deposition in vacuum, pump is off
C) slowly pressurize vacuum char

The silanized microspheres are then immediately placed in an oven at 120°C for 30 minutes to cure the reaction.

Solvent phase silanization: Microspheres are held at their stem and placed in silanization solution in an Eppendorf tupe. The silanization is performed in a solution of 90% methanol/water containing 2% APTES for 30 minutes. Microspheres are then washed three times with methanol/water, three times with methanol and three times with water and finally dried for 45 minutes at 120°C (Zammatteo, 2000).

All Chemicals were purchase form Sigma-Aldrich, WI.

E4 – Adsorption of Bovine Serum Albumin

For the adsorption experiment, I use the setup with the modified sample cell which can accommodate a liquid sample volume. I will demonstrate the effect of BSA molecules on an optical resonance after being injected into the clear, PBS (phosphate buffered saline) buffer solution of the sample cell. All solutions are previously filtered through a 0.2 μm sterile membrane filter. Settings for this experiment are:

- Microsphere: ~ 300 μm radius, prolate shape, immersed in PBS buffer solution
- Surface modification: positively charged amino groups (vapor deposition of APTES)
- Protein: 150 μM BSA dissolved in PBS
- Scan rate to acquire one transmission spectrum: 100 Hz
- Scan range: 10 to 40 mA corresponding to ~ 0.3 nm spectral width (laser threshold at ~ 7 mA)

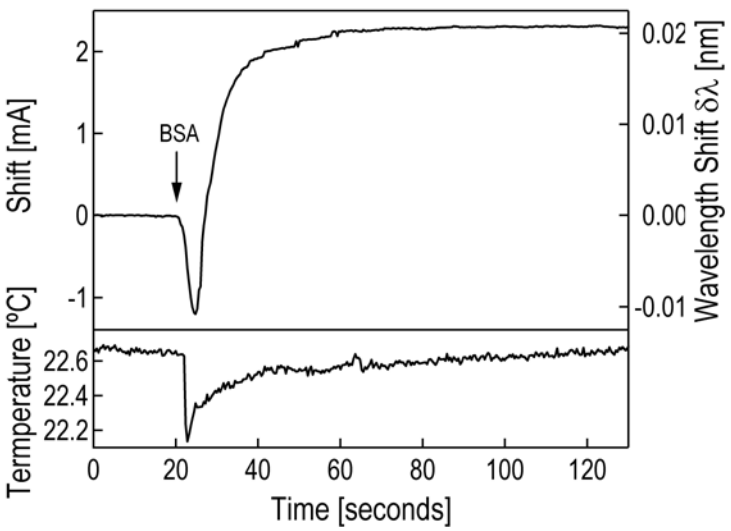

Figure E4.1: **Top**: Resonance wavelength shift due to adsorption of BSA molecules on the microsphere surface. **Bottom**: Temperature trace as recorded by the thermocouple throughout the experiment.

The ~ 300 μm diameter, aminosilanized microsphere is mounted in the sample cell filled with 1 ml of PBS buffer at room temperature (22.7ºC). The Labview program is started to record the trace of the resonance position. After equilibration of the resonance position at room temperature I inject 10 μl of the BSA solution into a total 1 ml of PBS sample volume to a final concentration of 1.5 μM. I display the recording of resonance position versus time as well as the recording of temperature versus time (fig. E4.1). The arrow indicates when the BSA solution is injected into the sample cell.

Notice the initial, negative shift of the traced resonance wavelength immediately after BSA injection (the wavelength scale is depicted on the right axis). This transient negative shift reverses rapidly and I observe an overall, positive resonance wavelength shift of +0.021 nm in equilibrium at RT. I attribute this overall positive shift to the adsorption of BSA molecules on the microsphere surface. The temperature trace, as recorded by the

thermocouple element located in close proximity to the microsphere, reveals a transient drop in temperature of about 0.5 °C immediately after injection of the BSA solution. The BSA solution was taken out of the refrigerator (proteins should be stored at lower temperatures just like other perishables). The refrigerated protein solution did obviously not have enough time to equilibrate exactly to room temperature (22.7°C). Injection of the slightly chilled BSA solution in the sample leads to a transient drop in the sample temperature which causes the microsphere to contract. Silica has a thermal expansion coefficient of ~ 7 x 10^{-6} /°C. A drop of 0.5 °C contracts the microsphere radius by ~ 1 nm. It is this transient thermal contraction of the microsphere I record as a negative wavelength shift on this trace of the resonance position. This initial negative shift is reversed rapidly as the solution equilibrates and I see an overall positive shift due to protein surface adsorption within ~ minute timescale. The adsorption process is largely diffusion limited since there is no mixing in this sample cell; I observe, however, convection due to evaporation of sample buffer from the open sample cell.

Figure E4.2: Langmuir-like adsorption isotherm of a BSA monolayer.

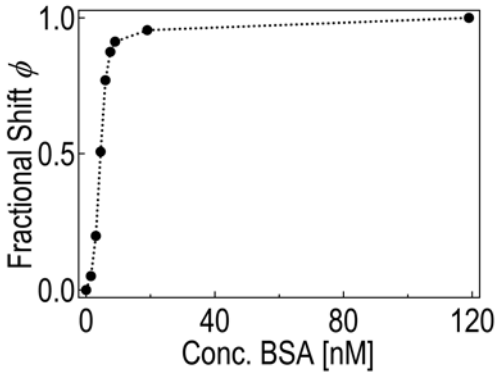

In the next experiment, I systematically vary the concentration of the BSA solution in the sample cell to determine the dose-response of this setup. I then normalize the measured wavelength shifts by dividing the magnitude by the value measured at saturation (at high BSA concentration > 20 nM, here 150 μM). I refer to those normalized resonance wavelength shifts as fractional shifts.

The measured adsorption isotherm shows a 'Langmuir-like' shape (fig. E4.2). This shape is expected, since the BSA molecules recognize binding sites on the microsphere surface where they will stably adsorb. The binding sites are limited and a fractional shift of 1.0 indicates complete protein-loading of the microsphere surface (~ 1 ng of total adsorbed protein material). The fact that fractional shift saturates at concentrations as low as 20 nM reveals that I am dealing with a saturated BSA monolayer for concentrations > 20 nM.

Apparently there is only one type of binding site on the microsphere surface – the BSA molecules do not seem to support additional BSA-BSA double or multi-layer forming, intermolecular contacts. The low concentration for half-maximal saturation at ~ 5 nM indicates a very strong affinity of the negatively charged BSA molecule towards the positively charged, aminosilanized surface. A Scatchard plot indicates a positive cooperativity for BSA binding to the aminosilanized surface.

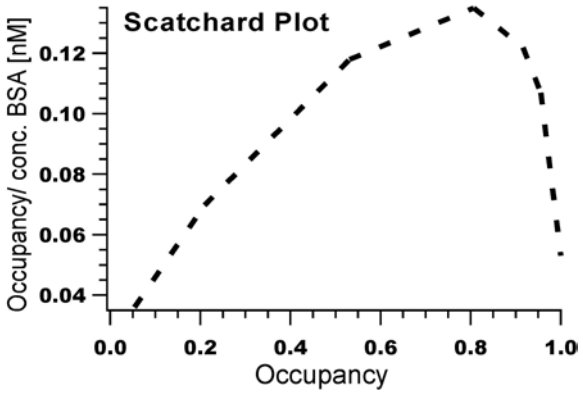

Fig. E4.3: Scatchard plot for BSA adsorption onto the aminosilanized silica surface.

If I assume complete BSA monolayer coverage for the shift measured at saturation, I calculate the thickness δa of the BSA monolayer from the conservation of optical size (Chapter B) as:

$$\frac{\delta\lambda}{\lambda} = \frac{\delta a}{a} \qquad \text{Eq (E4.1)}$$

For my microsphere of radius a = 150 μm, a measured resonance wavelength shift of δλ = + 0.021 nm after BSA adsorption and a nominal laser wavelength of λ = 1312 nm, I calculate the BSA monolayer thickness as

δa = 2.4 nm. Eq (E4.2)

I assume that the BSA molecule tries to maximize the adsorption enthalpy by binding with its largest planar projection. From the crystal structure of BSA (which is identical to the HSA structure) I know the least diameter of the molecule to be ~3.6 nm which is very close, but larger than my measured value of 2.4 nm. The reason why I measure a smaller layer thickness might be because the BSA monolayer is not closely packed: most likely there are voids of water between the individual surface adsorbed BSA molecules. In the next chapter I will derive an analytical formula which will allow us to calculate the surface density from my measured signal. Then I will see that there are indeed water filled voids between individually adsorbed BSA molecules. We should also keep in mind,

that this simple analysis presented here only works so well because the refractive index of proteins is almost identical to that of silica, the material of the microsphere cavity.

This sensor proves to be a powerful device for the study of surface assembled layers (such as self assembled BSA monolayers). The measurements allow calculation of bulk, thermodynamic properties of the molecular layer. From the dose-response curve at varying temperatures I can extract binding enthalpies and entropies. In the following chapter I will show an even more quantitative approach. We will develop a first order perturbation theory, which will allow us to relate the magnitude of the wavelength shift to the surface density of bound molecules. Ultimately, this approach will allow us to use this sensor in its most sensitive implementation: as a 'molecular mass spectrometer'. We predict that the binding event of a single macromolecule is detectable. The magnitude of the wavelength shift due to single molecule binding events would reveal the molecular mass of the protein as well as the number of proteins bound.

F First Order Perturbation Theory

F1 - Derivation of Perturbation Effect using the Photonic Atom Analog

In the following we will use first order perturbation theory to derive the magnitude of the wavelength shift of a microsphere cavity due to protein adsorption. We have published the derivation of this theory using two independent approaches developed with Stephen Arnold and Iwao Teraoka (Arnold, 2003; Arnold; 2004; Teraoka 2003). This is the first time to our knowledge that the frequency shift of a microsphere cavity due to molecular perturbation is quantitatively predicted. Other theoretical studies suggest the use of other transmission characteristics such as disk resonators for detection of biomolecules (Boyd, 2001).

In Chapter C we showed that the photonic atom modes of a microsphere are described by a Schrődinger-like equation:

$$\nabla^2\Psi + (V_{eff} - E)\Psi = 0 \qquad \text{Eq (F1.1)}$$

The effective potential V_{eff} was identified as a sum of "Energy due to refractive index contrast $k_0^2(1\text{-}n^2)$" + "Rotational Energy $l(l+1)/r^2$":

$$V_{eff}(r; k_0, n, l) = k_0^2(1-n^2) + l(l+1)/r^2 \qquad \text{Eq (F1.2)}$$

If we add an additional, nanoscopic layer to the microsphere surface as done with our BSA adsorption experiments at saturation, we perturb the effective potential by δV_{eff}:

$$\partial V_{eff} = \partial[k_0^2(1-n^2)] \qquad \text{Eq (F1.3)}$$

We remember from quantum mechanics, that the perturbation δV_{eff} of a non-degenerate energy level can be expressed by a first order correction δE_{eff} to the energy of the system:

$$\partial E_{eff} = \frac{\left\langle \Psi_r \middle| \partial V_{eff} \middle| \Psi_r \right\rangle}{\left\langle \Psi_r \middle| \Psi_r \right\rangle} \qquad \text{Eq (F1.4)}$$

In the photonic atom, V_{eff} acts only on the radial function Ψ_r of the complete wavefunction Ψ.

We remember form our discussion in Chapter D that for the photonic atom analog the Energy E_{eff} is identical to k_0^2. We thus have to write eq. (F1.4) as:

$$\delta(k_0^2) = \frac{< \psi_r | \delta[k_0^2(1-n^2)] | \psi_r >}{< \psi_r | \psi_r >}. \qquad \text{Eq (F1.5)}$$

The change in the square of the refractive index square is $\delta(n^2) = n_\ell^2 - n_m^2$, where n_ℓ and n_m are the refractive indices of the layer and medium respectively. The energy k_0^2 will not be constant and we expand eq.(F1.5) accordingly:

$$\delta(k_0^2)* < \psi_r | \psi_r >= \delta(k_0^2)* < \psi_r | \psi_r > + \\ < \psi_r | -k_0^2(n_\ell^2 - n_m^2) | \psi_r > + < \psi_r | -2k_0 \delta k_0 n_s^2 | \psi_r >,$$

Eq (F1.6)

which we can rearrange to:

$$< \psi_r | -k_0^2(n_\ell^2 - n_m^2) | \psi_r > + < \psi_r | -2k_0 \delta k_0 n_s^2 | \psi_r >= 0.$$

Eq (F1.7)

Expressing eq.(F1.7) in terms of volume integrals:

$$\int_{layer} -k_0^2(n_\ell^2 - n_m^2) |\psi_r|^2 dv + \int_{all\ space} -2k_0 n_s^2 \delta k_0 |\psi_r|^2 dv = 0.$$

Eq (F1.8)

which gives us:

$$\int_{layer} -k_0^2(n_\ell^2 - n_m^2) |\psi_r|^2 dv \cong -k_0^2(n_\ell^2 - n_m^2) |\psi_r(a)|^2 4\pi a^2 t.$$

Eq (F1.9)

Since 94% of the square of the wavefunction is located within the sphere, it is reasonable to take the second integral only over the microsphere volume:

$$\int_{\text{all space}} -dv \left|\psi_r(r)\right|^2 \ (2k_0)\delta k_0 n_s^2 \cong \int_0^a -dr\ 4\pi r^2 \ \left|\psi_r(r)\right|^2 \ (2k_0)\delta k_0 n_s^2 .$$

Eq (F1.10)

Therefore according to eq. (F1.8), eq. (F1.9) and eq. (F1.10), the fractional shift in frequency ($\frac{\delta\omega}{\omega} = \frac{\delta k_0}{k_0}$), is calculated as:

$$\frac{\delta\omega}{\omega} = \frac{\delta k_0}{k_0} = -\frac{a^2 t |\psi_r(a)|^2 (n_\ell^2 - n_m^2)}{2\ n_s^2 \int dr\ r^2 |\psi_r(r)|^2}. \qquad \text{Eq (F1.11)}$$

The integral in the denominator of eq. (F1.11) can be related to the surface value of the square of the spherical Bessel function in the limit in which the wavelength is much smaller than the microsphere radius:

$$\int_0^a j_\ell^2(\sqrt{\varepsilon_{rs}} k_o r) r^2 dr \approx \frac{a^3}{2} j_\ell^2(\sqrt{\varepsilon_{rs}} k_o a) \frac{\varepsilon_{rs} - \varepsilon_{rm}}{\varepsilon_{rs}} .$$

Eq (F1.12)

Substituting eq. (F1.12) in the denominator of eq. (F1.11) gives a differential shift due to additional loading of a layer on the surface, where ε_{rm} is the relative permittivity of the surrounding medium (here: water) and ε_{rl} is the permittivity of the loaded layer:

$$-\frac{\delta\omega}{\omega} = \frac{\delta\lambda}{\lambda} = \frac{(\varepsilon_{r\ell} - \varepsilon_{rm})}{(\varepsilon_{rs} - \varepsilon_{rm})} \frac{t}{a} = \frac{(n_\ell^2 - n_m^2)}{(n_s^2 - n_m^2)} \frac{t}{a}. \qquad \text{Eq (F1.13)}$$

In eq. (F1.13) we have presented the 1st order shift in terms of refractive indices and relative permittivities (i.e. $n^2 = \varepsilon_r$). If the refractive index of the layer and the refractive index of the silica microsphere are equal ($n_\ell = n_s$), eq. (F1.13) becomes identical to the eq. (D2.6) derived in Chapter D which described the conservation of optical size.

One can further introduce the molecular aspect of the experiment. The layer can be described as a surface assembly of molecular entities, each having an excess

polarizability α_{ex}. The excess polarizability α_{ex} of a molecule forming the layer is its polarizability P_l in excess of the polarizability of an equal amount of water P_w. We further introduce another variable: The number of molecules per surface area calculated as layer thickness t divided by molecular volume v_t. The molecular surface density shall be called σ. By using the equation $\varepsilon\mathbf{E} = \varepsilon_0\mathbf{E} + \mathbf{P}$ we arrive at the following expression for the permittivity difference times thickness in the numerator of eq. (F1.13):

$$(\varepsilon_{r\ell} - \varepsilon_{rm})\, t = \frac{P_\ell - P_w}{\varepsilon_0 E} t = \frac{P_{ex}}{\varepsilon_0 E} t = \frac{p_{ex}\, t}{\varepsilon_0 E\, v_t} = \frac{p_{ex}\, \sigma}{\varepsilon_0 E} = \frac{\alpha_{ex}\, \sigma}{\varepsilon_0}$$

Eq (F1.14)

With eq. (F1.14) we obtain:

$$\frac{\delta\lambda}{\lambda} = \frac{\alpha_{ex}\, \sigma}{\varepsilon_0 (n_s^2 - n_m^2) a}$$

Eq (F1.15)

This equation predicts the wavelength shift for a compact molecular monolayer of surface density σ. The equation is exact if the layer is considerably thinner than the evanescent field depth.

Ultimately, we are interested in the possibility for single protein detection. Single protein detection would be possible by looking at steps in the change of $\delta\lambda/\lambda$ with time, and this in turn provides a possible means for separately measuring α_{ex}. Since the light within a WGM circumnavigates the equator ($\theta = \pi/2$) in an orbit which is confined to a thin ring, molecules at polar angles outside the ring cannot influence the mode frequency. The greatest signal comes from molecules which stick at $\theta = \pi/2$ (fig. D2.2, Chapter D). For a TE mode which circulates at the equator, the angular intensity is proportional to $\left|\hat{L}Y_{\ell\ell}\right|^2$, which for large ℓ is proportional to $\left|Y_{\ell\ell}\right|^2$, the spherical harmonic describing the light orbit on the equator ($\ell = m$). So the ratio of the frequency shift for a protein at the equator to that averaged over random positions on the surface is enhanced by a factor $EF = 4\pi\left|Y_{\ell\ell}(\pi/2, \varphi)\right|^2$. This spatial enhancement EF can be significant. For the average sized microparticle anticipated (microsphere radius a ~ 100μm), $\ell \sim 1000$ and EF ≅ 36.

To obtain the average shift for an individual protein at a random position, we set the surface density in eq. (F1.15) to $\sigma = 1/(4\pi R^2)$ with the result $(\delta\lambda/\lambda)_r = \alpha_{ex}/[4\pi\varepsilon_0(n_s^2 - n_m^2)R^3]$. The shift due to a single protein at the equator is however enhanced: $(\delta\lambda/\lambda)_e = EF \times (\delta\lambda/\lambda)_r$, or (Arnold, 2003):

$$(\delta\lambda/\lambda)_e = \frac{\alpha_{ex}\left|Y_{\ell\ell}(\pi/2,\varphi)\right|^2}{\varepsilon_0(n_s^2 - n_m^2)\,a^3}. \qquad \text{Eq (F1.16)}$$

F2 - Quantitative Analysis of BSA Frequency Shift

At first glance, the excess polarizability of a protein may seem difficult to measure. There is, however, an easy method to determine the excess polarizability from refractive index measurements. One has to determine the change of the refractive index of a protein solution for increasing concentration of the protein or any other molecule of interest. From this change of refractive index over concentration, dn / dc, it is possible to calculate the excess polarizability according to:

$$\alpha_{ex}/4\pi\varepsilon_0 = (n/2\pi)(dn/dc)m, \qquad \text{Eq (F2.17)}$$

where n = 1.332 is the solvent refractive index (water), dn/dc = 0.184 cm^3/g is the differential refractive index of a BSA solution in water, and m = (66432 g/mol)/(6.02 × 10^{23} /mol) is the mass of a BSA molecule.

Eq. (F2.17) can be derived as follows:

Imagine a plate capacitor in free space (before). The volume of this capacitor is then filled with a dielectric liquid (later). I can relate the electric field measured for the capacitor filled with dielectric liquid (later) to the electric field before the capacitor was filled as: dielectric field later = dielectric field before + dielectric field introduced with the liquid of dipole moment density P.

$$\varepsilon E_{later} = \varepsilon_0 E_{before} + P \qquad \text{Eq (F2.18)}$$

To understand eq. (F2.18) we have to remember that the molecules of the dielectric are polarizable (the induced dipole moment of each molecule is $P_{molecule} = \alpha E$; α is the molecular polarizability). All of those induced dipoles are oriented inside the capacitor along the field lines and produce a net surface charge of the polarized dielectric opposing the original charges on the capacitor plates: $P = \sigma/\varepsilon_0$.

The dipole moment density of this dielectric is:

$$P = \frac{N}{V}\alpha E \qquad \text{Eq (F2.19)}$$

with N… number of molecules and V… volume of the dielectric between the plates of the capacitor. With eq. (F2.19) I can write eq. (F2.18) as:

$$\varepsilon E_{later} = \varepsilon E_{before} + \frac{N\alpha}{V} E_{before} = \varepsilon_0 (1 + \frac{N\alpha}{V}) E_{before}$$

Eq (F2.20)

This equation tells us the change of the electric field E_{before} after filling the capacitor with a dielectric of molecular polarizability α. I define a macroscopic material constant ε_r to characterize the macroscopic observable "relative permittivity" of a dielectric:

$$\varepsilon_r = (1 + \frac{N\alpha}{\varepsilon_0 V}) \qquad \text{Eq (F2.21)}$$

Realizing that N/V is the volume density ρ I can write the relative permittivity difference $\delta\varepsilon_r$ between a protein solution (polarizability α_p) and pure water (polarizability α_w) as:

$$\delta\varepsilon_r = \frac{\rho_p}{\varepsilon_0}(\alpha_p - \alpha_w) = \frac{\rho_p}{\varepsilon_0}\alpha_{ex} \qquad \text{Eq (F2.22)}$$

with α_{ex} being the excess polarizability (polarizability in excess of an equal amount of water).

With $\varepsilon_0\varepsilon_r = n^2$ I can relate eq. (F1.22) to the change in refractive index as:

$$2n\partial n = \partial \varepsilon_r = \frac{\rho_p}{\varepsilon_0}\alpha_{ex} \qquad \text{Eq (F2.23)}$$

If I introduce the mass density (concentration) $\delta c = m \times \rho_p$ (m… molecular weight) I get:

$$2n\partial n = \frac{m\rho_p\alpha_{ex}}{m\varepsilon_0} = \frac{\partial c\alpha_{ex}}{m\varepsilon_0} \qquad \text{Eq (F2.24)}$$

and I arrive at:

$$\alpha_{ex} = 2\varepsilon_0 nm\frac{\partial n}{\partial c} \qquad \text{Eq (F2.25)}$$

With eq. (F2.25) I can calculate the excess polarizability of BSA from published dn/dc measurements as:

$\alpha_{ex} = 4\pi\varepsilon_0 \times 3.85 \times 10^{-21}\ \text{cm}^3$

I can now use eq. (F2.15) to relate the wavelength shift of + 0.021 nm to the surface density of bound BSA molecules. At saturation, I measure a BSA surface density σ of:

$\sigma_s = 1.7 \times 10^{12}\ \text{cm}^{-2}$

Therefore, the average surface area covered by one BSA molecule is:

$\sigma_s^{-1} = 5.9 \times 10^{-13}\ \text{cm}^2$.

From crystallographic data I previously showed the largest planar projection of BSA to be about 3.7×10^{-13} cm^2, which is ≈ 63% of our measured surface density σ_s^{-1}, consistent with no more than one layer of adsorbed BSA molecules.

For the above experiments I used solvent silanization to amino-modify the microsphere surface. In other experiments done with vapor-deposited amino-groups, I measure an even higher shift for a surface adsorbed BSA monolayer adsorption on microspheres of comparable size. The silanization procedure using vapor deposition seems more effective. The following table shows the slightly different results for the BSA saturation shift depending on the aminosilanization method used to condition the microspheres to

promote adsorption. The areal projection is calculated assuming complete coverage (no voids).

Table F2.1: Experimentally determined BSA data (surface density, layer thickness, percentage coverage).

	Solvent Silanization	**Vapor Silanisation**	**X-Ray Data**
Layer thickness	2.4 nm	3.6 nm	3.7 nm
BSA areal projection σ_p^{-1} calculated: 3.7×10^{-13} cm^2	5.9×10^{-13} cm^2	3.4×10^{-13} cm^2	3.5×10^{-13} cm^2
Surface Density σ_s	1.7×10^{12} cm^{-2}	2.9×10^{12} cm^{-2}	-
Percentage Surface Coverage	63%	>90%	-

BSA binding to an aminosilanized microsphere previously modified by vapor deposition seems to form an extremely compact layer. Surface coverage seems on the order or even higher than the percentage coverage achieved by a close packing of spheres. I can illustrate the closed packed BSA monolayer with the following artistic picture (fig. F2.1).

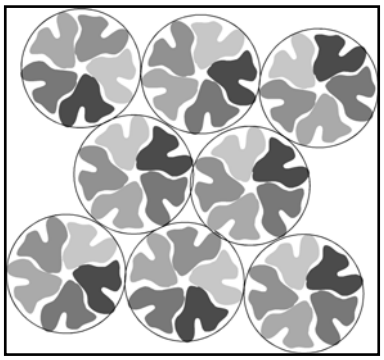

Figure F2.1: Artistic representation of a compact bsa monolayer.

A surprising result is the low noise in the current signal before the BSA was added: the low standard deviation of 20 μA corresponding to 0.18×10^{-3} nm. Using equation (F2.16) which predicts the frequency shift for a single molecule binding on the microsphere directly on the light orbit, I calculate the sensitivity of our current setup with the 300 μm microsphere diameter on the order of ~10000 BSA molecules.

From equation (F2.15) I learn that decreasing the sphere radius will increase the fractional shift in wavelength proportional to the microsphere radius a^3. The enhancement factor EF, however, will decrease with smaller radius proportional to the cavity radius $a^{1/2}$, slightly reducing the boost of wavelength shift for smaller microspheres. Assuming the Q-factor does not change when choosing smaller microspheres as sensors, I should be able to amplify the shift signal proportional to $a^{-5/2}$ – the smaller the microsphere, the larger the shift. Limitations are reached when the radius of the microsphere is similar to the wavelength ~ 1 μm in this case. This limitation might be overcome by working with high refractive index material (at the appropriate wavelength) such as silicon (n = 4) or amorphous sapphire (n = 1.7): the wavelength inside the material will be significantly shorter and will allow resonances in even smaller microspheres (Arnold, 2003).

By choosing higher refractive index material for the microsphere-waveguide system (e.g. amorphous sapphire with n = 1.7) and by choosing a shorter nominal wavelength of 400 nm it seems reasonable to achieve high-Q resonances in microspheres which can be as small as 3 - 4 μm in diameter. Assuming a Q on the order of 10^7 (comparable to our current results), our theory predicts single molecule resolution of our spectrometer for sapphire microspheres of 3 - 4 μm in size (please refer to Chapter I). The wavelength shift due to a single macromolecule such as an antibody will be detectable. Single mass-loading events on the microsphere surface will be revealed as steps in the wavelength-shift signal thus turning our device into a "mass-spectrometer".

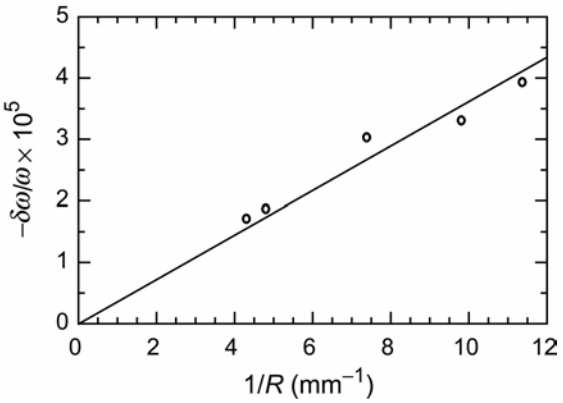

Figure F2.2: Microsphere size dependence of BSA monolayer shift. R is the microsphere radius.

I experimentally confirmed the 1/R (R is the microsphere radius) size dependence predicted by equation (F2.15). I fabricated microspheres ranging in radius from 88 μm to 232 μm. All of the microspheres are then modified with amino-surface groups by vapor

deposition of APTES. The saturation shift for BSA monolayer adsorption at high BSA concentrations was recorded for each sphere and plotted versus 1/R (fig. F2.2). The data was fit by a straight line going through the origin. Within the scatter in the data over this size range, a 1/*R* size dependence appears reasonable. Using the formula which describes conservation of optical size, $\delta k_0 / k_0 = \delta\omega / \omega = -\delta R / R$, I can determine the average layer thickness from the slope of the line as 3.6 nm. Again I measure a reasonable result for a compact BSA monolayer: crystallographic data predicts a layer thickness of about 3.7 nm.

F3 - System Calibration: Determination of Thermal Expansion Coefficient of Silica

For this experiment, I calibrate the thermocouple element which allows a reading within 0.1 K resolution. The silica microsphere is mounted in the sample cell as descried before.

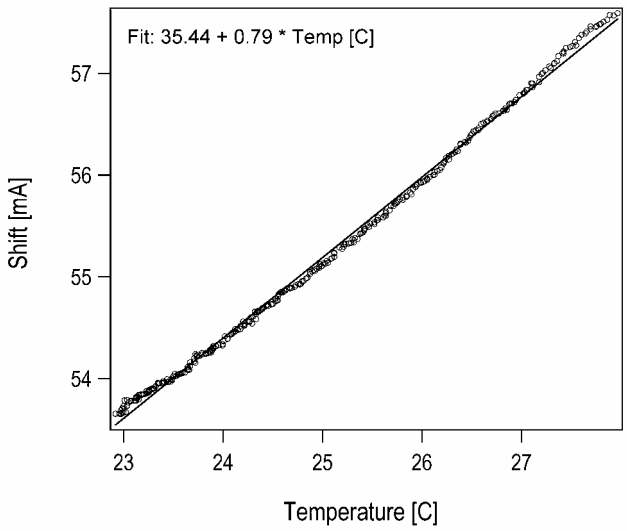

Figure F3.1: Wavelength shift associated with the thermal contraction of the silica microsphere.

The cell is then filled with 1 ml of warm water. The shift of resonance frequency was recorded while the sample cell cooled down to room temperature. I plot the wavelength shift versus the temperature T (fig. F3.1). The slope is determined from a linear fit as 0.79 mA / °C.

With a laser tuning coefficient of $\beta = 0.01$ nm/mA I determine the resonance wavelength shift with temperature as:

$\delta\lambda/\delta T = 0.008$ nm / °C

The conservation of optical size predicts a resonance wavelength shift δλ as a function of the change of effective sphere radius δa as:

$$\frac{\partial\lambda}{\lambda} = \frac{\partial a}{a}$$

With the thermal expansion coefficient κ I can formulate the change in microsphere radius δa as:

$$\partial a = a\kappa\partial T$$

and I can predict the resonance wavelength shift as a function of temperature T as (notice: the shift due to temperature is independent of sphere size):

$$\kappa = \frac{\partial\lambda}{\lambda\partial T}$$

with a nominal wavelength of λ = 1312 nm I measure a thermal expansion coefficient for the fabricated silica microspheres of:

$\kappa = 6.1\ 10^{-6}$ [1/°C]

which is very close to the reported literature value for the thermal expansion coefficient of quartz: 7.07×10^{-6} / °C. A smf-28 fiber is expected to have a very similar expansion coefficient. We havt to remember however, that the fiber is made of doped silica material which has been melted before. This might explain why I measure a slightly larger thermal expansion coefficient.

G Biosensing: Protein Recognition and DNA Hybridization

The contents of this chapter have been published (Vollmer, 2003).

G1 - Molecular Recognition

A wealth of chemicals form the organic matter in our natural environment. If I take our selves as an example, even though 90% of our body mass is water, the remaining 10% is a hugely diverse collection of mostly organic molecules. Many of the organic compounds are essential in the sense that we have to extract them from our environment before being able to incorporate those building blocks into our own, biochemical structure. Vitamins are such an example of essential compounds. Since they cannot be produced by our own chemical factories – found in all kinds of specialized cells and tissues throughout our body such as glands - we have to make sure that they are part of our food supply.

Many more chemicals, however, can be autonomously produced by the human body, given that building blocks such as aminoacids, sugars and free energy in the form of ATP are readily available. The blueprint for synthesis of such "household" chemicals is stored on a large molecule itself: the DNA. Each cell has access to a copy of this synthetic pathway library in the form of DNA coiled up as chromosomes which are located in each cell nucleus. All species (plants, animals and archaebacteria alike) use an identical DNA code. Four bases (A, T, C, G) form this linear code. There is one additional important feature of our genetic code: it is redundant. Each DNA molecule consists of two, linear polymers each made up of such a string of bases. Those two strands are bound to each other forming a double-helix (fig. G1.1).

Figure G1.1: DNA doublehelix, chemical structure.

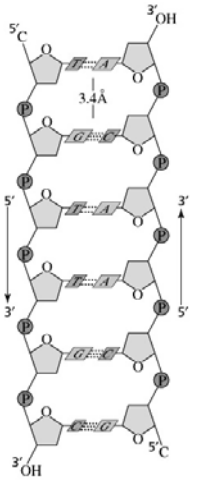

The bases are zipped-up by binding with each other (Watson-Crick base pairing). Each one of those bases binds to only one complementary base. Theses rules for binding are known as Chargaff rules: A pairs with T, G pairs with C. The redundancy of the double-helix is essential to maintain the code in the hazardous environment of the real world. The DNA is constantly subjected to mutations e.g. due to UV radiation and toxins. Such harmful alterations of the DNA sequence can be completely reversed as long as only one of the two complementary DNA strands is affected at a time.

Sequences of the DNA code are read out (interpreted) in different ways. In the most direct encoding, a DNA sequence codes for the amino acid sequence of a corresponding protein: 3 bases are read as a triplet called codon. Each codon codes for one out of 21 aminoacids. The codon table which relates codon and aminoacid is also highly conserved across different species.

Many other compounds in our body, such as lipids, are indirectly encoded. In this case, the DNA codes for several proteins (enzymes), which themselves are part of an anabolic, biochemical pathway. The product of this multi-step, biochemical pathway is as one example the lipid molecule. By this indirect encoding it is possible to store the information for synthesis of almost any, non-protein chemical compound. By stereo selective synthesis surprisingly complex molecules can be formed and the most complex ones have often evolved at the frontline of interspecies confrontation. Survival of the fittest led to invention of many complex organic compounds such as the paralyzing agent of the Japanese Fugu fish.

Once produced or supplied, it is the interaction between all those micro- and macromolecules that allow the complex actions and reactions we know as life. Molecular interactions are responsible for our ability to read this thesis.

Specific interactions between such a plethora of protein is guaranteed by a process called molecular recognition. In the center of molecular recognition stands the macromolecule typically a protein which has a "real volume" and thus presents a molecular surface to its surrounding environment. It is the molecular surface of proteins that allows them to specifically find a complementary surface by highly selective molecular binding. Molecular Surfaces of proteins are thus the carrier of a 'topologic code', a code secondary and higher dimensional in nature as compared to the primary, linear DNA code. The topologic code represented by the surface of proteins is so specific and selective that it allows them to find a complementary molecular surface among many billions of possibilities tested by diffusion. A protein bumps into parts of other proteins or chemicals many thousand times per second. Only when the interaction between those surfaces is just right does molecular recognition take place: complementary surfaces match in a lock-and-key mechanism. The two molecules recognize each other and stay together on a long enough timescale to exert their biochemical function.

To allow enough coding possibilities the topologic code exists only for macromolecules, which are large enough to allow a topologic (>three-point) interaction with a potential binding partner. This requirement in size is the reason why large proteins play such an important role in signal transduction cascades throughout our body. Chemical signals are mediated by large protein molecules needed to specifically transmit a complex code. A typical *E.coli* gene consists of about 1000 bases and thus is ~ 330 amino acids long. This gives an average size of a typical *E.coli* protein of ~30 kD, about half the size of the BSA molecule I have used in my previous experiments (one amino acid weighs about 120 D). Such a macromolecule has enough volume and thus surface to carry a topologic code compromised of:

- The primary amino acid sequence of the protein.
- The secondary, tertiary, and quarternary protein structures.
- The Coulomb potential resulting from the dimensional arrangement of charged aminoacids.
- Hydrophobic bonding.
- Steric exclusion principles.
- Hydrogen bonds, extending e.g. from each peptide bond.
- Long range Coulomb interactions starting from a charged protein surface-group and mediated into the surrounding by alignment of multiple water dipoles.

How to represent this topologic code in a general analytic form has not yet been figured out and should be a major research effort. Such a general form would allow the immediate identification of binding partners. Complex protein networks of which a complete set would form the artificial cell in silico could be modeled based on the understanding of the topological code, a task very important for drug discovery in the pharmaceutical industry.

The above ideas might be fiction for now however, we realize that the specific interaction between molecules of which at least one is a macromolecule of sufficient mass to act as a topologic code carrier is a hallmark of the biological world.

Any biosensor can make use of this specificity of molecular recognition, by immobilizing a so called recognition element on the sensor surface. The recognition element ideally reacts exclusively with only one chemical compound: the target analyte. The molecular recognition event of binding of the target analyte is then transduced by most biosensors into an electronic or optical signal. Whole arrays of recognition elements on array type sensors such as gene chips are used for parallel detection strategies. In the following I will use the highly specific, well studied interaction between vitamin H which is also called biotin and its specific binding partner called streptavidin to demonstrate biosensing by molecular recognition using this sensor system.

Notice that within the outlined semantics we can say that a linear polymer such as DNA is used for information storage, whereas a globular polymer such as a protein is used for information transduction or computation.

G2 Biotin-Streptavidin interaction

Streptavidin is a globular protein of 56 kD, It has four binding pockets for an organic compound called biotin (vitamin H). The interaction between streptavidin-biotin is known as the strongest, non-covalent bond in nature. The affinity constant is on the order of 10^{-15} Molar.

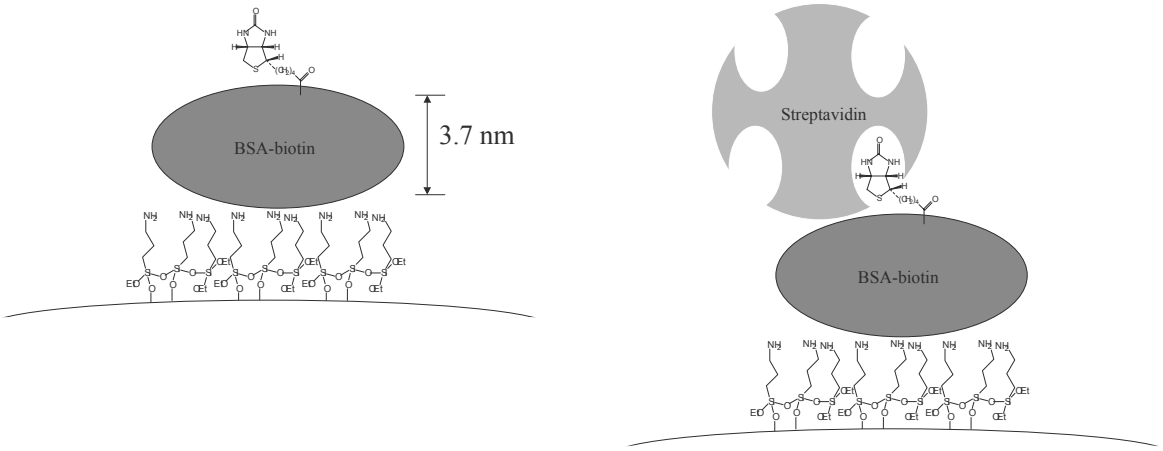

Figure G2.1: Biotin-streptavidin interaction: streptavidin has four binding pockets for biotin. Previously surface immobilized, biotinylated BSA will be used as the recognition element to specifically detect streptavidin binding.

In the following experiment, I will use vitamin H as a recognition element immobilized on the microsphere sensor surface. This can be easily achieved by the use of biotinylated BSA: each BSA molecule of this compound is chemically modified with several biotin molecules. The biotinylated BSA is immobilized on the aminosilanized microsphere surface in a way similar to the surface adsorption procedure I established for non-modified BSA in the last chapter. By immobilization of biotinylated BSA as the recognition element on this sensor surface I can prime the microspheres for detection of the target analyte streptavidin. To test the use of this device as a biosensor I then inject

the target analyte. I should be able to determine a resonance wavelength shift which monitors the specific binding of streptavidin to biotin (fig. G2.1).

The experimental results are shown in fig. G2.2. The arrow indicates when BSA-biotin (final concentration 1.5 μM) and streptavidin solution (0.01 mg/ml final) have been successively added to the liquid sample cell.

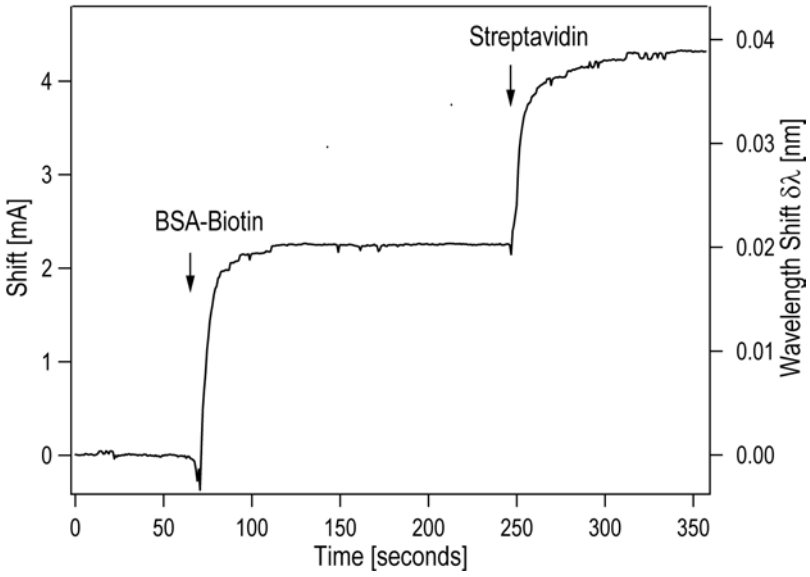

Figure G2.2: Immobilisation of BSA-biotin and successive specific binding of streptavidin.

I clearly see two resonance wavelength shifts: the initial shift is due to surface adsorption of a biotinylated BSA monolayer. After surface adsorption of BSA-biotin at saturation, I am left with a biotin recognition layer stably adsorbed on the microsphere surface. The wavelength shift equilibrates for the value corresponding to a BSA-biotin monolayer. Subsequent injection of the straptavidin solution results in a second shift: the streptavidin molecules diffuse to the microsphere surface where they encounter the surface immobilized BSA-biotin. Once recognized by biotin, a strong binding constant keeps the streptavidin immobilized to the surface as a second layer. Only streptavidin leads to a second wavelength shift – other proteins (e.g. BSA itself) do not result in any additional change of the microsphere resonance wavelength. With this multilayer experiment I have demonstrated the use of this resonant microsphere system as a biosensor for specific streptavidin detection.

G3 - Multiplexed Detection of DNA hybridization: Single Nucleotide Mismatch Discrimination

DNA is the storage form for the blueprints of our chemical nature. It is thus the chemical representation and identification of ourselves as individuals. The DNA of any two human beings might be similar depending on their evolutionary history (such as for twins) – but no two DNA molecules are 100% identical. Forensic sciences make increasing use of the ability to identify any individual by sequencing relevant parts of their DNA. As we interact with our environment, we often leave traces of ourselves in form of shed cells. Such cells might be dead in the sense that they show no more signs of an active metabolism but they still contain DNA molecules in their nucleus. A single DNA molecule is often enough to identify our individual sequence signature. Considering the wealth of different sequences and the miniature sample amount often available, a useful biosensor should be able to analyze sequences in parallel with highest sensitivity and selectivity (Junhui, 1997).

Gene chips (Wang, 2000) are an example of array type, parallel biosensors among other fluorescent techniques (Abel, 1996). To identify a DNA sequence, a DNA chip makes use of the unique ability of a DNA molecule to find its complement by specific binding (hybridization). Gene chips are fabricated by immobilizing sequences of interest on a sensor substrate which is typically glass. Only where the exactly matching sequence is immobilized on the sensor surface one will be able to detect a signal from the corresponding complementary sequence when detected in a sample. The detection method of choice for gene chips is based on fluorescence microscopy. A sample is preprocessed by labeling all of the contained DNA with a fluorophore. The sample is then exposed to the surface immobilized DNA recognition elements (sequences). A sample sequence is detected when a fluorescence spot builds up after the labeled DNA of the sample accumulates on the surface by specific binding only to the surface immobilized, complementary DNA molecules (the recognition elements) located in that specific area of the chip surface. Recent developments utilize the evanescent field of an

optical fiber for fluorophore excitation and detection (Pilevar, 1998; Graham, 1992; Healey, 1997; Piunno, 1995; Watts, 1995).

One main disadvantage of this technique is the requirement for a fluorescent label and there is a strong interest in developing ultra-sensitive, *label-free* DNA detectors (Song, 2002; Liu, 1999). In the following I will show how this sensor system presented with this thesis can be modified for parallel DNA measurements. I will demonstrate detection of DNA sequences using two microspheres. Each microsphere carries a different DNA sequence (recognition element) and is therefore specific for detection of only this DNA sequence. Parallel detection using two microspheres allows one to perform referenced measurements. In the following experiments I will utilize a referenced measurement to discriminate a single nucleotide mismatch. I will use the high specificity of the DNA hybridization process to detect a single nucleotide in a target DNA. Two DNA recognition sequences each immobilized on a separate microsphere differ from each other in only one base. If I now inject a sample target sequence, which is complementary to one of the microsphere-immobilzed sequences, it will preferably hybridize to this matching sequence. Hybridization to the other sequence is impaired since one of the bases do not match. I will be able to tell from sign of the difference signal, whether a hybridized target carries an T or a G mutation depending on preferred hybridization to the one or the other microsphere.

G4 DNA Immobilization on Hydrogels

DNA immobilization on silica supports of biosensors and microarrays have been widely studied (e.g. Chrisey, 1996; Dolan, 2001; Diehl, 2001; Henke, 1997; Joos, 1997; Kumar, 2001; Kumar, 2000; Lindroos, 2001; Rogers, 1999; Sabanayagam, 2000; Walsh, 2001; Zammatteo, 2000).

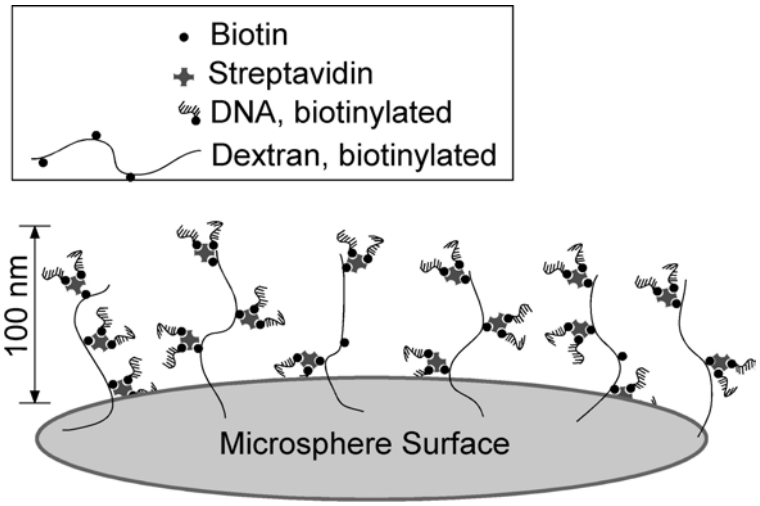

Figure G4.1: DNA immobilization strategy using a dextran hydrogel.

Typical DNA sequences immobilized as recognition elements on a DNA chip have a length of 20-25 nucleotides. Each nucleotide has a molecular weight of ~330 D. The single stranded DNA molecule thus has a molecular weight of less than 10 kD, 6 times less than that of previously measured BSA. In order to still achieve the highest resonance wavelength shifts after hybridization to the complementary DNA, I attempt to maximize the surface density of the bound DNA recognition elements. This can be achieved by modification of the sphere surface with a polymer matrix: a hydrogel. In this example, I will use a dextran hydrogel (Gregorius, 1995) which I will immobilize by physical adsorption onto the plasma cleaned microspheres. Dextran is a 70 kD polymer ~ 100 nm long which forms an ultrathin mesh on the microsphere surface after adsorption (Kuehner, 1996; Sengupta, 2003). I will then use the strong biotin streptavidin interaction to link DNA molecules throughout this matrix of the immobilized dextran-hydrogel. Instead of dextran, however, I will use biotinylated dextran which carries ~ 7 biotin groups per dextran molecule. The DNA recognition elements themselves will also be biotinylated at the 5' end of the linear DNA molecule. I then link the biotinylated DNA to

the surface immobilized, biotinylated dextran-hydrogel by using streptavidin as a monofunctional linker (fig. G4.1).

Materials Methods used in Chapter G2-4

Biotinylated DNA: The DNA is custom made by Quiagen Operon. The biotin modification is located at the 5' end of the oligonucleotide and is separated by a 15-atom spacer from the beginning of the DNA (biotin-TEG).

Hydrogel based microsphere-immobilization of DNA: The microspheres are fabricated in a butane/nitrous oxide flame as described before. Before use they are cleaned by 4 minutes of oxygen plasma etching as detailed in Chapter C. The microspheres are held head-over-end in a sponge-holder. They are then immersed in a ~ 4 μl hanging drop of a dextran-biotin solution until dry (fig. G4.2), thus forming a dextran-biotin hydrogel on the sphere surface.

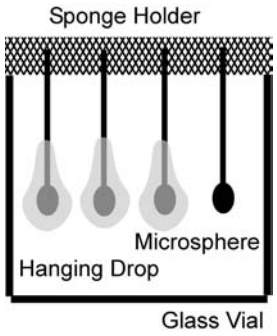

Figure G4.2: Surface modification of microspheres using a hanging drop of dextran in this example.

They are then briefly dipped in water for ~ 5 minutes. This ensures removal of excess dextran by the water solvent. Meanwhile, the solution of biotinylated oligonucleotides is mixed with the streptavidin solution at a molar ratio of 2:1. The final concentration of the formed streptavidin-biotin-DNA oligonucleotide complex is 7 μM. The microspheres are incubated with this solution until dry in another hanging drop of ~ 4 μl volume. The spheres can be stored in the dry state for weeks. After brief dipping in water for ~ 1 minute the spheres are used immediately.

Compound	Manufacturer	Description
Dextran-Biotin Solution	Sigma, MO	10 mg/ml biotinylated dextran solution to form hydrogel by drying on silica surface
DNA Oligonucleotides	Quiagen Operon, CA	Single stranded DNA sequences, biotinylated at the 5' end (Biotin-TEG)
Streptavidin	Sigma, MO	Streptavidin solution for bridging biotinylated dextran and biotinylated DNA oligonucleotide
Sponge Holder	-	Polymer foam into which microspheres can be poked and held with one end.

G5 Two-Sphere Multiplexing on a Single Fiber Waveguide

It is possible to evanescently couple more than one microsphere to the same thinned portion of the eroded smf-28 fiber. Each microsphere is held by its own xyz stage.

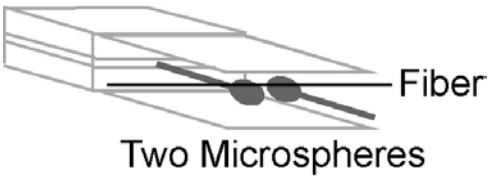

Figure G5.1: Sample cell for coupling two microspheres to the same, thinned optical fiber.

The sample cell utilized throughout this experiment is open on three sides (fig. G5.1), which allows the positioning of an additional microsphere by front-loading.

Fig. G5.2 shows a transmission spectrum obtained after sequentially coupling of first one and then two microspheres to the same optical fiber. The resonances corresponding to each microsphere are labeled S1 and S2. They are separated by several line width and can thus be unambiguously identified. The microspheres are modified with a dextran-hydrogel. Scattering losses due to the almost transparent dextran matrix are low: the Q is still on the order of 5×10^5. A refractive index of the dextran hydrogel which is very close to that of water helps to limit further absorption losses.

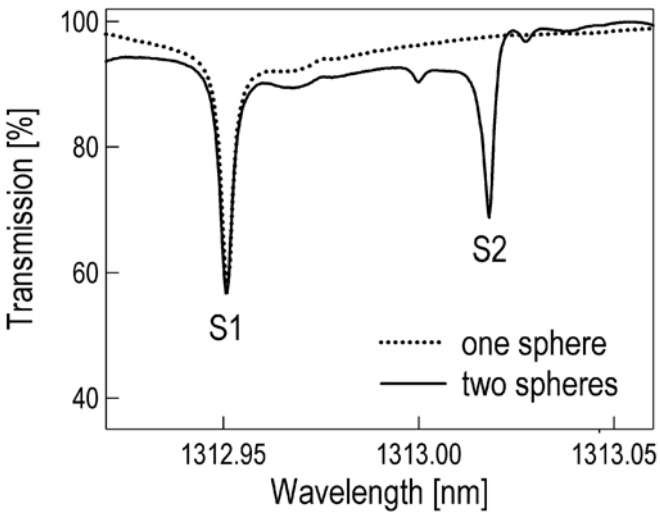

Figure G5.2: Transmission spectrum obtained after coupling first on (S1) then another (S2) microsphere to the same optical fiber.

G6 Sequence Specific Detection of DNA Hybridization

I will use two microspheres S1 and S2 coupled to a common smf-28 fiber.

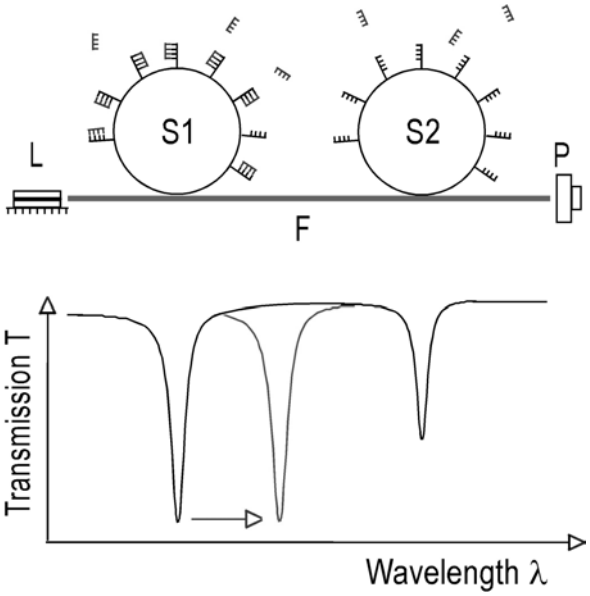

Figure G6.1: Schematic of the experiment for sequence specific detection of DNA hybridization using two microspheres.

Each of the two microspheres is modified with a DNA sequence of interest. The oligonucleotides are immobilized by using a hydrogel-based microsphere modification procedure outlined in Chapter G4. The two sequences immobilized on microsphere S1 and S2 are unrelated. I will demonstrate that specific hybridization to the DNA carried by microsphere S1 can be identified from a red shift of the microsphere-specific resonance wavelength (depicted in grey, fig. G6.1).

Chemical modifications of the microspheres S1 and S2 are summarized in the following table:

	MICROSPHERE S1	MICROSPHERE S2
1. Surface Cleaning	Plasma cleaning, 4 minutes	
2. Hydrogel physisorption	Biotinylated dextran Solution (10 mg/ml) adsorbt by hanging drop method	
3. Removal of excess hydrogel	Dip in distilled water, 5 minutes	
4. DNA immobilization	Biotinylated oligonucleotides pre coupled (at 2:1 molar ratio) to streptavidin; bound to dextran-biotin modified microsphere using hanging drop method (7 μM final concentration)	
6. Removal of excess DNA	Dip in distilled water, 5 minutes	
DNA sequence information	5'-ATTAATATAATTCAATCCTCGAGCAGAGTT	5'-ATTAATACGACTCACTATAGGGCGATG
Biotin modification	5'-biotin, 15-atoms spacer (biotin-TEG, Operon)	

Fig.G6.2 shows the wavelength shift of two resonances, one corresponding to microsphere S1 and the other one corresponding to microsphere S2.

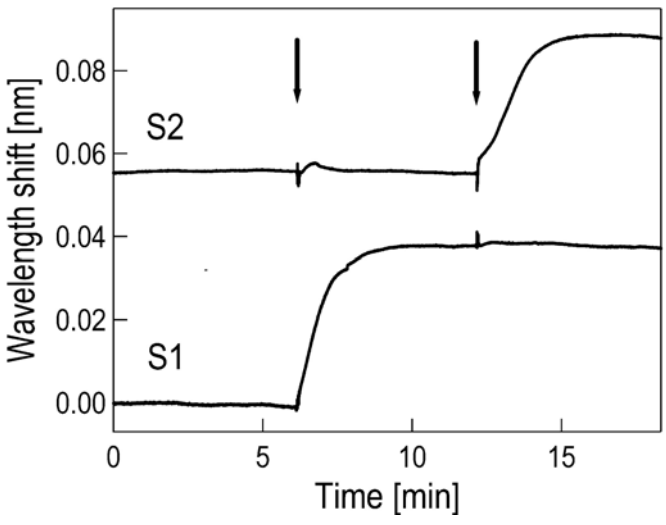

Figure G6.2: Microsphere specific DNA hybridization.

The arrows indicate when complementary DNA sequences have been added to a final concentration of 1 μM into the sample cell. First I inject the

DNA sequence complementary to the oligonucleotides immobilized on microsphere S1. I observe that only the S1-specific resonance wavelength shows a large red shift of ~ 0.038 nm. I then inject the DNA sequence complementary to the oligonucleotide immobilized on sphere S2. Again, I observe only the S2-specific increase in resonance wavelength (again ~ 0.038 nm). I do not observe any additional shift of the S1 specific resonance wavelength which is an indication that there is no significant unspecific binding of the DNA to the dextran hydrogel. With an excess polarizability of $4\pi\varepsilon_0 \times 4.8 \times 10^{-22}$ cm^3 for the hybridized oligonucleotide targets I calculate a surface density of 3.6×10^{13} oligonucleotide targets/cm^2.

The DNA recognition elements have previously been immobilized on the biotin-dextran hydrogel as a streptavidin-DNA complex. Each streptavidin molecule is bound to two biotinylated 27-mer oligonucleotides. I measure a wavelength shift of 0.255 nm for the binding of the streptavidin-DNA complex to the surface immobilized, biotinylated dextran hydrogel. With the excess polarizability of $4\pi\varepsilon_0 \times 4.3 \times 10^{-21}$ cm^3 for the streptavidin-DNA complex, I estimate the density of immobilized oligonucleotide probes as 4.6×10^{13} oligonucleotide probes/cm^2. By taking the ratio of the measured surface density for the hybridized target strands and for the immobilized DNA probes, I find that 78% of the immobilized single-stranded DNA is accessible for hybridization. Therefore this approach seems to combine the highest surface probe density with good accessibility for hybridization (Georgiadis, 2001).

G7 Differential Hybridization Measurement: Detection of a Single Nucleotide Polymorphism (SNP)

Discrimination of a single nucleotide is the ultimate test for any DNA biosensor. In the following experiment I attempt to identify a single nucleotide in an 11 base long DNA sequence by making use of the ability of DNA to hybridize preferably to its complement. I will use an 11-mer DNA oligonucleotide of known sequence except for the base at the 5th position (marked with a question mark):

C	T	A	T	?	T	C	A	G	T	C

I know that it is either a G (guanine) or a T (thymidine) therefore I will use two 11mer oligonucleotides, each immobilized on sphere S1 and S2 to determine whether the base in question is a G or a T nucleotide.

The two microspheres S1 and S2 are modified as described in chapter G4 with the following oligonucleotides that differ each at the 5th base, the position of the unknown nucleotide:

S1	**S2**
5'-CTAT**C**TCAGTC	5'-CTAT**A**TCAGTC

If I inject the sample sequence into the sample chamber with the so modified microspheres S1 and S2, I expect a large shift for hybridization to the perfectly matching sequence. If the 5th nucleotide is a G, the wavelength shift corresponding to microsphere S1 should be larger than that of microsphere S2.

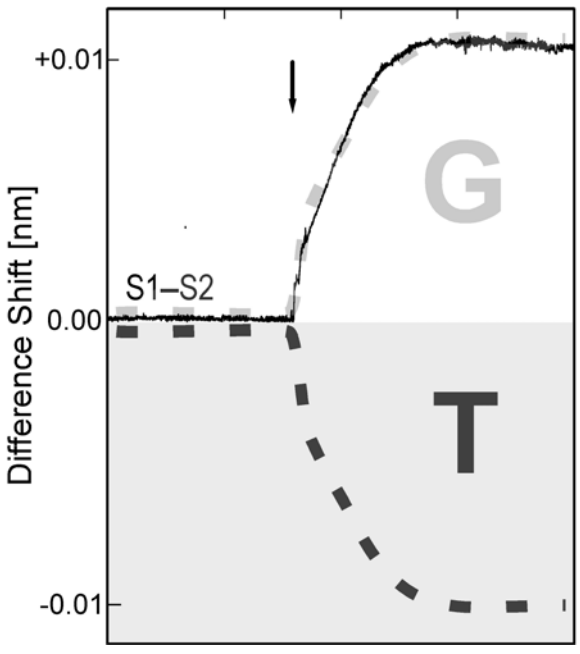

Figure G7.1: Differential shift identifying the single nucleotide in question as a G.

If the 5th nucleotide is a T, however, the situation is reversed and the wavelength shift corresponding to microsphere S2 should now be larger than that of microsphere S1. Accordingly, if I plot the wavelength shift of microsphere S1 minus the wavelength shift of microsphere S2 I should be able to identify the nucleotide in question: a positive difference shift indicates a G, a negative wavelength

shift indicates a T nucleotde at the 5th position of this sample sequence. Fig. G7.1 shows the result. The arrow indicates when the sample has been injected to a final concentration of 1 μM. I unambiguously identified the mutation as a G with a surprisingly high signal to noise of 54 determined as wavelength shift after hybridization divided by noise of signal before hybridization. With a complete set of 4 microspheres it would be possible to determine any nucleotide (A, G, T or C) at an arbitrary position also referred to as single nucleotide polymorphism. Taking this idea even further, it should be possible to determine the sequence of an N-mer oligonucleotide by hybridization to 4 x N microspheres.

Detection of the mismatch is optimal at a specific temperature and salt concentration which depends on the length of the oligonucleotide to be analyzed. Previously I varied the salt concentration and determined hybridization efficiencies of an 11-mer oligonucleotide on a single microsphere. I found the hybridization signal from the matching sequence can be nearly 10 times as large as the one from the mismatching sequence if the experiments were performed in a 20 mM Tris buffer (pH 7.8) containing 30-70 mM NaCl at room temperature (~23ºC).

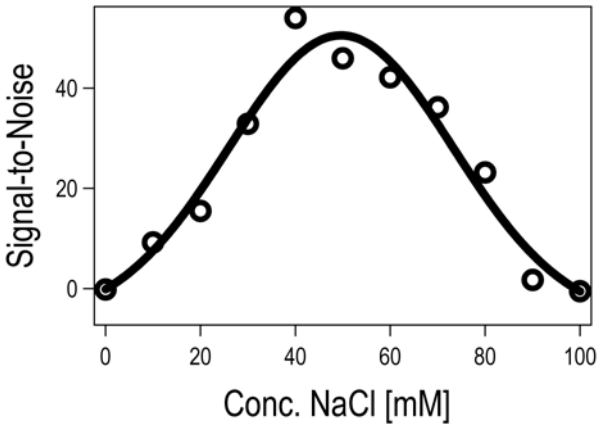

Figure G7.2: Optimizing the salt concentration for single nucleotide detection.

These optimized conditions were used in the above experiment. Only for the optimal salt concentration of 30-70 mM NaCl I reached the high signal to noise of 54. Increasing the salt concentration to more than 150 mM or less than 1 mM will reduce the signal-to-noise to less than 1. It is therefore imperative to determine the working range of the ionic strength for best results using this kind of SNP analysis.

G8 Discussion of Chapter G

In previous chapters I have demonstrated that this biosensor is a valuable tool for the study and identification of nucleic acids with single nucleotide resolution. DNA biosensors are valuable tools for real-time bio-specific interaction analysis. It has been shown that SPR systems (please refer to Chapter K) can be used to monitor different operations with DNA, such as strand separation, hybridization kinetics and enzymatic modifications (Nilsson, 1995; Watts 1995). The system presented with this thesis is useful for all of these approaches. The difference compared to SPR sensors, however, is the ultimate sensitivity of the resonant technique. Another difference is that SPR systems are difficult to design for parallel measurements, which seems ideal in this approach: multiple microspheres can be coupled to one or several waveguides. Both techniques are sensitive to refractive index changes and thus require no labels such as fluorophores used in other evanescent field DNA detectors mostly utilizing tapered optical fibers (Fang, 1999; Piunno 1995). The real-time monitoring of both techniques allows extraction of kinetic data which provides important information on affinity constants given a useful binding model. The time resolution of this system presented here (on the order of 1 μs) can be exploited for detection of rapid chemical steps such as the unzipping of single DNA bases. Furthermore, this system might eventually be miniaturized to an array type sensor with spot dimensions < 10 μm.

Wide-scale DNA testing also requires the development of small and robust lab-on-a-chip or micro-total analysis systems (μTAS; Wang, 2000). Integration of this device on a semiconductor chip seems possible by replacing silica with silicon components. Such a DNA chip would be an ideal analytic component of any robust and miniature lab-on-a-chip device or could be produced as a DNA array for massive parallel measurements. Existing DNA chips (Ramsay, 1998) and single DNA sensors detect the fluorescently labeled DNA when binding to recognition elements immobilized on plain glass surfaces or tapered optical fibers (Healey, 1997; Graham 1992; Pilevar 1998). A promising approach is also the use of fluorescently labeled molecular beacons in fiber-optic gene arrays (Steemers, 2000). It seems that the approach I presented in my thesis is an

alternative to these systems which does not require any labeling of the DNA and thus facilitates the analytic process.

H Fluorescent Imaging of Whispering Gallery Modes

The same setup as described in Chapter G is used for the following experiments. In this case, the light from a 635 nm red laser diode is coupled into a SM-600 single mode fiber.

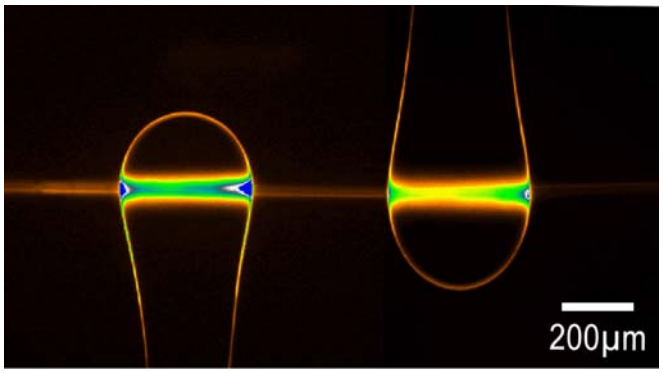

Figure H1.1: Fluorescent image of two microspheres coupled to the same optical fiber. The color scale reflects the intensity: hotspots are blue.

Evanescent coupling to the fiber is achieved as described before except that the SM-600 fiber is etched down to a final diameter of 2 µm to access the evanescent field of the narrow 4 µm fiber-core. The two microspheres are immersed in a fluorophore solution (Cy5, Molecular Probes) diluted 1:100 from the stock in PBS. The spheres are imaged on a cooled CCD using only an emission filter and a standard 6x objective. The evanescent field associated with each resonant mode excites the fluorophore solution. By imaging the emission from the fluorophore we can see inside the microsphere cavity and trace the resonant light orbit which would otherwise be stealth.

Fig. H1.1 shows the light orbiting in two spheres coupled to the same optical fiber. Notice the resonant enhancement of the fluorescent light emitted from the evanescent field of the light orbit as compared to the evanescent field of the eroded optical fiber. The light orbit seems to have a width on the order of several wavelengths (~ 10 µm).

Component	Manufacturer	Description
635 nm Laser Diode DL3038-011	Sanyo, NJ	Single longitudinal mode red laser diode.
Single mode fiber SM-600	Canadian Instrumentation & Research, Canada	Fiber single mode at 635 nm. Core diameter 4 μm; less as compared to the previously used smf-28 fiber.
Fluorophore Cy5	Molecular Probes, OR	Fluorophore, emission peak at ~ 670 nm, absorption peak at ~ 650 nm
Cooled CCD SensiCam	Cooke, MI	Camera to observe fluorescent micrographs
Emission filter D680/30M	Chroma Technology, VT	Emission filter mounted on microscope fluorescent channel. Transmits at 680 nm with a cutoff-width of 30 nm
Microscope Axioscope	Zeiss, Jena	Camera mounted on tube of Axioscope. Emission filter directly mounted on filter cube (no excitation filter, no beam splitter in this experiment)

Table H1.1: Materials used in Chapter H.

Dependent on the relative orientation of microsphere versus thinned optical fibers it is possible to create quite interesting resonant light orbits in this microsphere. Fig. H1.2 summarizes the observed light orbits for several orientations of thinned fiber versus microsphere. The thinned fiber runs vertically down the center of each picture. Interestingly, one of the light orbits resembles the topology of a Moebius sheet. Notice that the width of the resonant light orbit is on the order of several μm. In some pictures it is possible to identify interference effects along the orbital path, e.g. last picture of the series. This observation is especially intriguing since the resonant modes are formed by a traveling wave: we would not expect any standing wave pattern.

The microsphere cavities form three dimensional stadiums. The analysis of the resonances in such deformed cavities might be of interest for the study of chaos in quantum billiards.

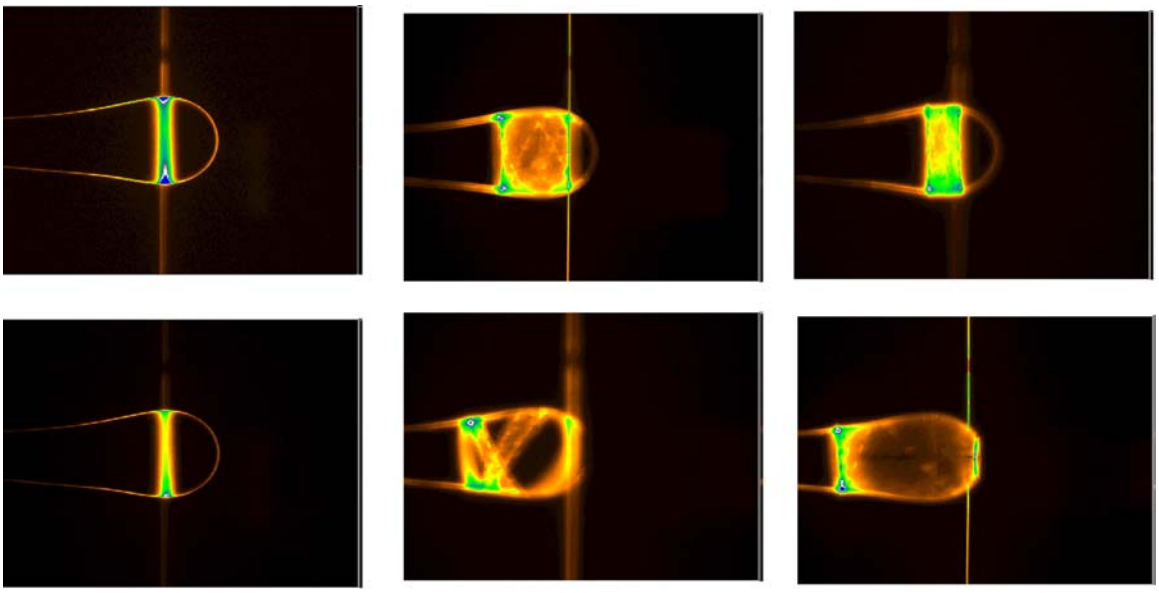

Figure H1.2: Fluorescent images of resonant light orbits in microspheres. The nature of the orbit varies depending on relative position of microsphere versus fiber.

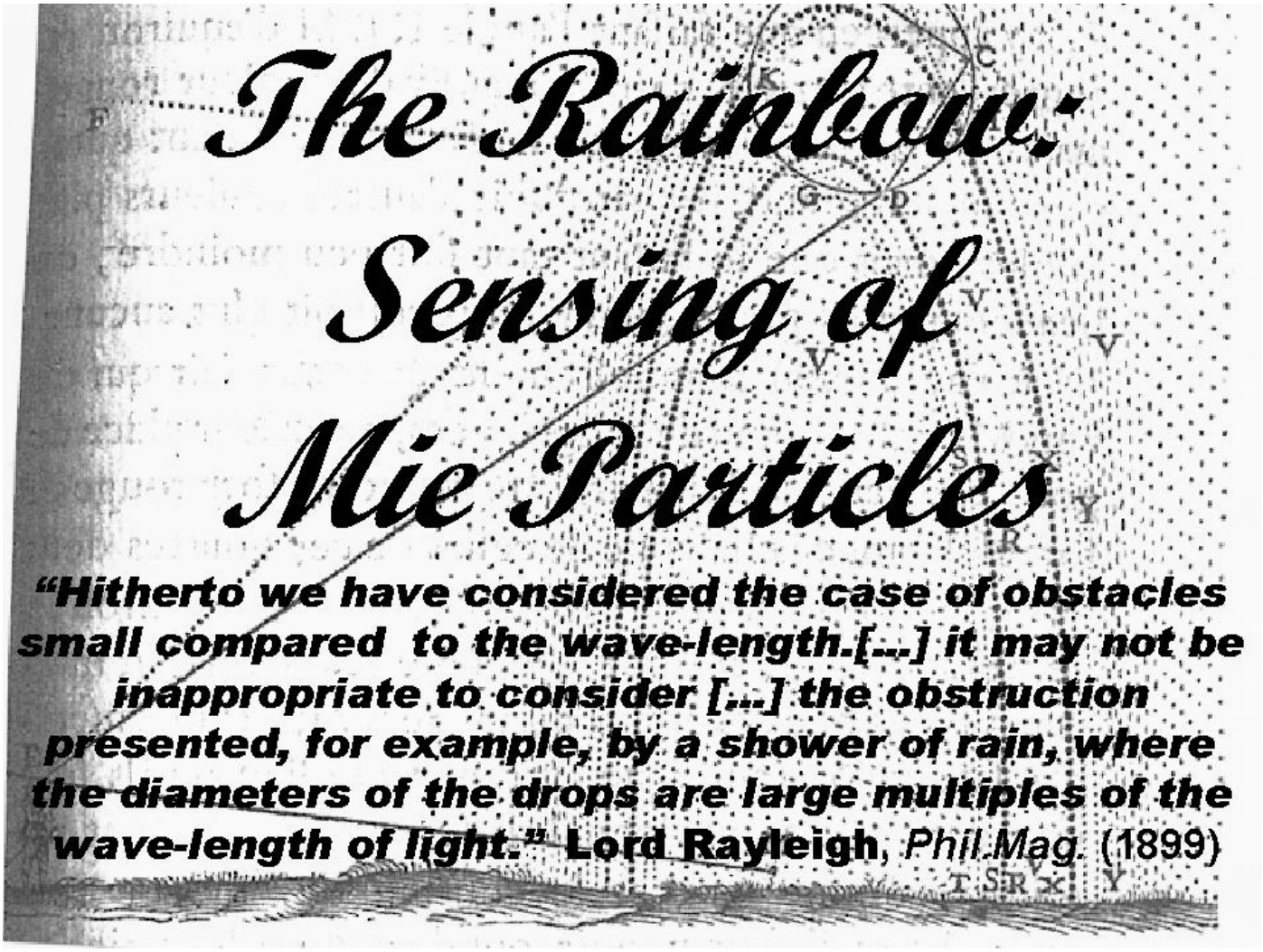
The Rainbow:
Sensing of
Mie Particles
"Hitherto we have considered the case of obstacles small compared to the wave-length.[...] it may not be inappropriate to consider [...] the obstruction presented, for example, by a shower of rain, where the diameters of the drops are large multiples of the wave-length of light." Lord Rayleigh, Phil.Mag. (1899)

I Bacterial Detection with an Evanescent Field: Leaving the Rayleigh-Limit

In previous chapters I have used optical resonances in microspheres for detection of nanoscopic objects such as proteins and DNA. Such biomolecules are two to three orders of magnitude smaller as compared to the resonance wavelength. I have shown that objects of this Rayleigh regime produce a red shift of the microsphere resonance wavelength, which is proportional to the polarizability times the surface density of the molecular material loaded on the microsphere surface. Our first order perturbation theory correctly predicts the wavelength shift for such a condensed 2D phase of proteins: the shift corresponding to a compact monolayer of BSA molecules agreed in theory and experiment. Studies with a variety of other protein monolayers of different polarizability confirm this approach (Noto, 2004). In this Rayleigh regime our analysis was simplified by the fact that the evanescent field could be taken as constant across the distance of the analyte molecule. Furthermore, I did not measure any electrostatic or dipolar interactions between neighboring protein molecules. Similar as for a dilute gas, we could consider the surface adsorbed protein and DNA molecules as isolated dipoles even for a condensed, compact monolayer. The macroscopic observable shift of the resonance wavelength was just the sum of the molecular contributions of each biomolecule and therefore an extensive property of our resonant system. The individual polarizability of a nanoscopic Rayleigh particle is small so that I did not detect any significant scattering which could have resulted in a linewidth reduction of the high-Q resonant transmission line.

Figure I.1: Illustration of molecules, bacteria and wavelength.

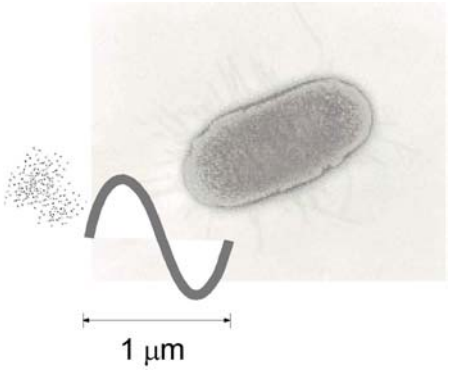

In the following chapter I will leave this nanoscopic world of biomolecules. Instead, I will perturb a microsphere resonance with macroscopic biological objects large enough in size to be directly observed with the microscope. Such macroscopic biological

objects are cells, bacteria, viruses, spores and plant pollen.

For my experiments I have choosen an organism widely used in molecular biology: *Escherichia Coli* (*E.coli*). *E.coli* is a cigar-shaped bacteria with dimensions on the order of 1 x 2 μm (fig. I.1). It is an enterobacteria and can be found as an inhabitant in parts of our digestive system. *E.coli* is a benign symbiont although aggressive malignant strains causing severe, bloody diarrhea are known (*E.coli* O157:H7). As few as 10 germs can cause illness. An estimated 73,480 people are infected per year and 600 of those cases are fatal (according to the federal Centers for Disease Control and Prevention). The size of this bacterial analyte is on the order of our resonant wavelength ~ 1 μm.

From other optical experiments we know that the physical rules for this mesoscopic size range are different from the optical rules encountered in the nanoscopic Rayleigh world. We are thus primed to expect new observations for bacterial adsorption on the microsphere cavity. Furthermore, I am now able to visualize the macroscopic bacterial adsorbent with a conventional microscope which allows me to directly relate the surface density with the measured shift of the resonance wavelength.

PROPERTIES OF *E.COLI*	
Shape	Rodlike, cigar shape
Dimensions	1 x 2 μm
Refractive index whole cell	1.387
Volume	1 μm^3
Effective radius of sphere of equal volume	0.62 μm
Total dry weight/cell	2.8×10^{-13} g
Total weight of one cell	9.5×10^{-13} g
Fastest doubling time	20 minutes

Table I.1: Biophysical properties of *E.coli*.

For the development of the theory in Chapter F we have so far ignored the decay length or penetration depth of the evanescent field extending from the microsphere surface. The evanescent field, however, drops exponentially with increasing distance from the microsphere surface as we have seen from our calculations in Chapter C2. The field strength drops to 1/e of its initial value over the distance of one decay length which is roughly the

wavelength: ~ 1 μm in this case. For small, nanoscopic objects such as typical macromolecules with dimensions comparable to BSA (less than 10 nm) we can assume the molecule to be completely immersed in the evanescent field of highest strength as it is encountered in the immediate surrounding close to the resonant microsphere-surface.

For larger biological objects, however, the dimension of the target entity (0.1 – 10 μm) becomes comparable or even larger than the decay length of the evanescent field. To predict the wavelength shift associated with microsphere-binding of such larger analytes we have to modify the previously derived theory. In the following, we will now have to take into account the penetration depth of the evanescent field. To assure the veracity of our mathematical approach, I will compare the new theoretical results with measurements taken from *E.coli* bacteria accumulating on the microsphere surface. The new analytic theory presented in this chapter has been derived by Hai-Cang Ren.

When bound to the microsphere surface *E.coli* is immersed in an evanescent field *gradient* rather than a constant evanescent field. The evanescent field magnitude drops significantly along the distance of the (least) dimension of the surface adsorbed bacteria (fig. I.2).

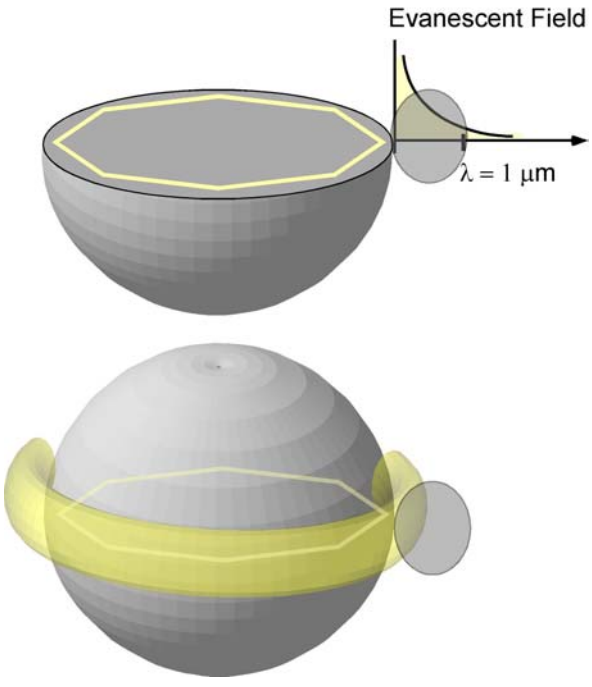

Figure I.2: *E.coli* immersed in evanescent field associated with the microsphere resonance.

As for any object made of polarizable material such as proteins and DNA, we can expect a measurable wavelength shift after surface adsorption of *E.coli*. Because

of the decay length of the evanescent field, the magnitude of the shift, however, will be much smaller as compared to the magnitude predicted by the simple equation derived in Chapter F.

I1 - Surface Adsorbtion of *E.coli*

In the following experiment, I will adsorb *E.coli* bacteria to the microsphere surface. The microsphere is previously modified with a poly-l-lysine hydrogel to promote stable bacterial surface adsorption. Poly-l-lysine is a widely used polymer for coating petri-dishes to accommodate epithelial and other cells.

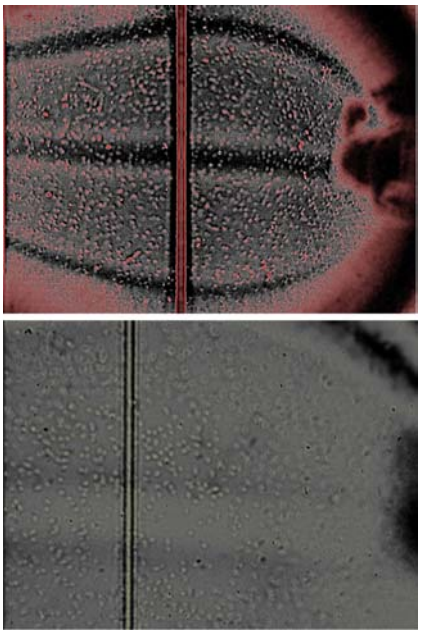

Figure I1.1: Adsorption of *E.coli* to poly-l-lyisine modified microspheres. Image of microsphere-fiber contact using a 20x (top) and 40x (bottom) objective. The images have been enhanced by false colors.

The experiment is performed in PBS buffer where the surface density of bound *E.coli* can reach more than 2.5 x 10^6 cm^{-2}. Notice that even for this high density, the mean distance between neighboring bacteria is still much larger than 1 μm (fig. I1.1). The cavity diameter of the microsphere in this experiment is measured as 340 μm. The *E.coli* surface density is determined from a videotape footage showing bacterial adsorption on a magnified (using a standard 20x-40x objective) area of the microsphere (fig. I1.1). With the help of the video footage, the immobilized *E.coli* can be discriminated from motile, unbound bacteria and the surface density can be determined by counting the adsorbed bacteria in a given microsphere-surface area (typically 1-100 counts). Fig. I1.3 shows one resonance dip of the transmitted spectrum followed over a time course of 4000 seconds while bacteria randomly diffuse to the microsphere surface where they permanently adsorb. The graph shows a few snapshots of the resonance position at 0, 100, 200, 300, 400, 500, 2000 and 4000 seconds incubation time. The bacteria accumulate on the microsphere surface which leads to a red shift of the

resonance wavelength. We realize a new effect as compared to previous molecular measurements: the linewidth of the resonance broadens with increasing accumulation of surface bound *E.coli*. Let us first, however, focus on the wavelength shift and compare its magnitude with the prediction of the theory previously developed in chapter F.

For this prediction, we will model the *E.coli* as a sphere of equal refractive index and volume (table I.1) as the original bacteria. *E.coli* has an average volume of $4/3\pi a^3 \sim 1\ \mu m^3$ which corresponds to an effective radius of a = 0.62 μm.

A uniformly polarized sphere can be regarded as a dipole to calculate the associated field at the sphere surface (fig. I1.2).

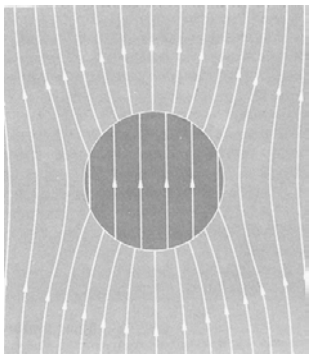

Figure I1.2: Polarization of a dielectric sphere (Purcell, 1985). Radius of the sphere is a.

A dielectric sphere (as all dielectrics of ellipsoidal shape) in a constant, homogenous external field will become uniformly polarized and will have a constant electric field inside. This allows us to calculate the polarizability of the spherical dielectric object as (Purcell, 1985):

$$\alpha = 4\pi\varepsilon_0 \times n_{medium}^2 a^3 \left(\frac{n_{bacteria}^2 - n_{medium}^2}{n_{bacteria}^2 + 2n_{medium}^2} \right)$$

As expected for a uniformly polarized object, the polarizability α of a spherical object is proportional to its volume a^3.

Taken this formula to calculate the polarizability of *E.coli*, we are able to predict the wavelength shift for bacteria using the previously developed theory. For an adsorbed bacterial density of 2.5 x 10^6 cm^{-2} we predict a wavelength shift of +0.82 nm. From our data (fig. I1.3), however, we determine the wavelength shift as ~ 0.05 nm, more than an order of magnitude smaller than predicted.

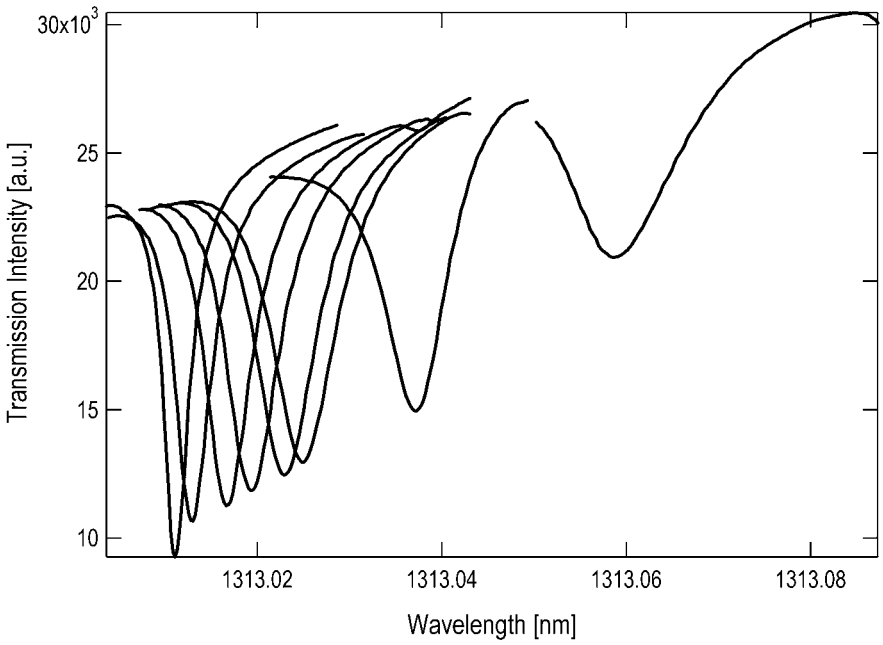

Figure I1.3: Wavelength shift and linewidth broadening due to microsphere-surface adsorption of *E.coli*.

I2 Perturbation Theory for Bacteria and other Large, Biological Objects

A rigorous, general derivation of the wavelength shift takes into account the drop of the evanescent field across the distance of the dimensions of a larger (e.g. bacterial) microsphere-adsorbent leaves us with the following result (Vollmer, 2004).

The electromagnetic field triggered by the optical fiber is determined by the macroscopic Maxwell equations. For a harmonic time dependence, $e^{-i\omega t}$, the equation satisfied by the electric field **E**, reads:

$$\varepsilon\omega^2\mathbf{E} - \nabla\times(\nabla\times\mathbf{E}) = -i\omega\mathbf{J} \qquad \text{Eq (I2.1)}$$

with **J** the electric current induced by coupling with the optical fiber. The dielectric constant is given by:

$$\varepsilon = \varepsilon_0 + \delta\varepsilon \qquad \text{Eq (I2.2)}$$

with ε_0 accounting for the background (cavity and solution) and $\delta\varepsilon$ accounting for the coated particles such as bacteria. We have $\varepsilon = \varepsilon_{\text{cav.}}$ for $r < R$ and $\varepsilon = \varepsilon_{\text{sol.}}$ for $r > R$ with R the radius of the cavity. The magnetic permittivity has been neglected.

The solution to eq. (I2.1) takes the form

$$E_a(\mathbf{r}) = -i\omega \int d\mathbf{r}' G_{ab}(\mathbf{r}, \mathbf{r}' \mid \omega) J_b(\mathbf{r}') \qquad \text{Eq. (I2.3)}$$

which has been averaged over the distribution of adsorbed particles. The poles of the Green function $G_{ab}(\mathbf{r}, \mathbf{r}' \mid \omega)$ on the complex $\omega^2 -$plane give rise to resonance frequencies and the corresponding linewidth, both are explicitly known for WGM in the absence of adsorbents. The scattering of the WGM modes by the adsorbed particles shifts the resonance wavelength and lowers the Q value of the cavity.

To treat the problem systematically, we recognize that the Green function $G_{ab}(\mathbf{r}, \mathbf{r}' \mid \omega)$ is mathematically equivalent to that of a quantum scattering problem with a vectorial wave function in an effective potential. The potential contains all multiple scattering processes and can be expanded according to the ascending powers of the excess dielectric constant of the coated particles, $\Delta\varepsilon$, and their density, σ on the surface of the cavity. The first term of the effective potential, which is proportional to $\sigma\Delta\varepsilon$, represents the mean field effect of the coated particles and its impact on the resonance can be obtained from eq. (I2.1) with the dielectric constant replaced by the average one. The Born approximation in this case gives rise to the shift of the resonance line:

$$\frac{\delta\lambda}{\lambda} = \frac{8\pi\Delta\varepsilon\sigma a^3}{(\varepsilon_{\text{cav.}} - \varepsilon_{\text{sol.}})R} f\left(\frac{8\pi a}{\lambda}\sqrt{\frac{\varepsilon_{\text{cav}}}{\varepsilon_{\text{sol.}}} - 1}\right) \qquad \text{Eq (I2.4)}$$

where a is the effective radius of a bound particle and λ is the wavelength in the solution. The form factor $f(z) = \frac{1}{z}(1 + e^{-z}) - \frac{2}{z^3}(1 - e^{-z})$ takes care of the damping of the evanescent field outside the cavity. This formula works quite well for *E.coli*, partly because of its small value of $\Delta\varepsilon$.

The corresponding line width can be estimated from the incoherent radiations from the coated particles driven by the electromagnetic field of the incident WGM. The result is

$$\Gamma = \frac{64\pi^3 \Delta\varepsilon^2 a^6}{27\varepsilon_{\text{sol.}}(\varepsilon_{\text{cav.}} - \varepsilon_{\text{sol.}})\lambda^4 R} F\left(\frac{4\pi a}{\lambda}\right). \qquad \text{Eq (I2.5)}$$

with F(z) another form factor which can be evaluated numerically. The agreement with the observation is only up to the order of magnitude and smaller as measured (a factor 3 ~ 4 off may be attributed to the asymmetric shape of *E.coli*, please refer to next chapter). For now, let's come back to the wavelength shift.

Inserting the form factor in eq. (I2.4) it can be re-written as:

$$\frac{\Delta\lambda}{\lambda} = \frac{6\sigma\alpha_{ex}}{\varepsilon_0\left(n_{cavity}^2 - n_{buffer}^2\right)R} f(z) \qquad \text{Eq (I2.6)}$$

Where f(z) is the unit-less form factor. As mentioned before, the form factor is a function of the size of the spherical bacteria and is defined as:

$$f(z) = \frac{1}{z^2}\left(1 + e^{-z}\right) - \frac{2}{z^3}\left(1 - e^{-z}\right) \qquad \text{Eq (I2.7)}$$

with

$$z = 8\pi \frac{a}{\lambda_0}\sqrt{1 - \frac{n_{buffer}^2}{n_{cavity}^2}} \qquad \text{Eq (I2.8)}$$

The unit-less form factor f introduces the scale of the adsorbed object (with an effective radius a) compared to the resonant wavelength λ_0 (which is roughly on the order of the penetration depth of the evanescent field).

The form factor f can be developed into a series, which converges for z -> 0 (i.e. for nanosized objects with an effective radius a << λ_0) :

$$f(z) = \frac{1}{6} - \frac{z}{12} + \frac{z^2}{40} - \frac{z^3}{180} + \frac{z^4}{1008} + \ldots \qquad \text{Eq (I2.9)}$$

For such small molecular objects (such as BSA), a << λ_0 thus z -> 0 and:

$$f(z) \cong \frac{1}{6} \qquad \text{Eq (I2.10)}$$

Inserting this nanoscopic limit in equation (I2.6) we again arrive at our previous theoretical expression derived in Chapter F:

$$\frac{\Delta\lambda}{\lambda} = \frac{\sigma\alpha_{ex}}{\varepsilon_0\left(n_{cavity}^2 - n_{buffer}^2\right)R} \qquad \text{Eq (I2.11)}$$

We recognize our previously derived equation as the nanoscopic limit of the more general solution of eq. (I2.6). Eq. (I2.11) is valid only for small, molecular objects whose dimensions are much smaller than the wavelength, typically at least one order of magnitude. For larger objects such as bacteria, we need to introduce the form factor f which describes the reduction in wavelength shift due to the limited penetration depth of the evanescent field (fig I2.1).

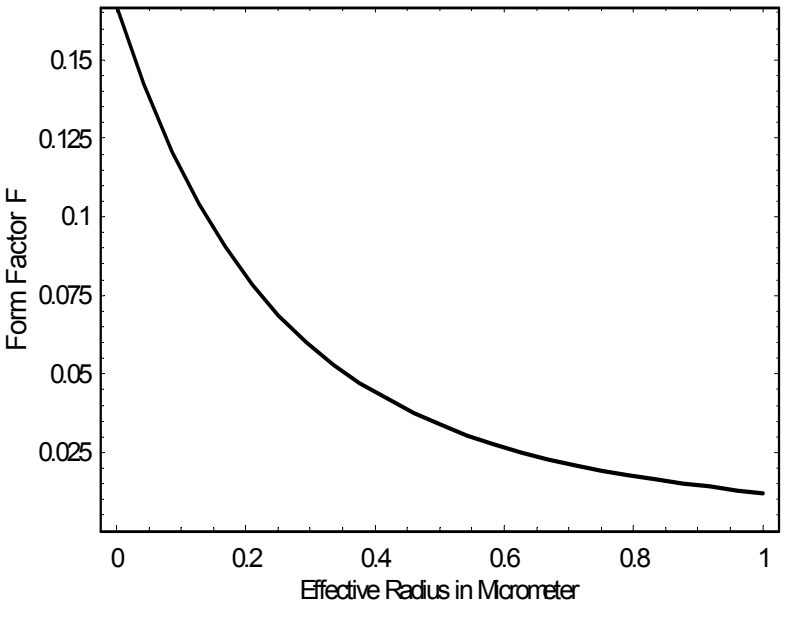

Figure I2.1: Plot of the form factor f versus the effective radius a of a spherical, bacterial object (λ_0=1312, n_{buffer} = 1.33, n_{cavity}=1.457, $n_{bacteria}$=1.387).

We see how the form factor approaches its limit of 1/6 at the nanoscopic (left) limit of the x-axis for nanometer sized objects (such as a protein molecule). For larger objects, however, the form factor decreases rapidly in magnitude

which reflects the limited extent of the resonant evanescent field. This rapid drop in magnitude is associated with the prediction of a reduced wavelength shift by the general theory eq. (I1.6) as compared to the wavelength shift predicted by the simple eq. (I2.11).

Fig I2.2 shows a 3D plot for the predicted wavelength shift associated with microsphere-adsorption of bacteria such as *E.coli* (n=1.387) as a function of surface density and spherical volume. Notice that the wavelength shift predicted by eq. (I2.6) is no longer proportional to the volume (polarizability) of the adsorbate (as it was predicted by the previous equation I2.11).

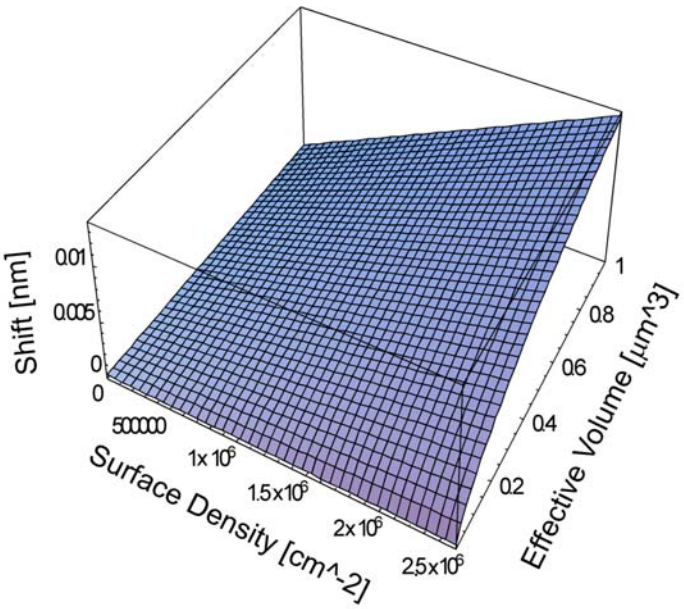

Figure I2.2: Plot of predicted wavelength shift versus surface density and effective volume of an object with similar optical properties as *E.coli* using eq. (I2.6).

Does this corrected theory described by eq. (I2.6) fit to the experimental data collected with *E.coli*? Fig (I2.3) shows the measured and predicted wavelength shift versus bacterial surface density. We realize how well the theory described by eq. (I2.6) agrees with the measured wavelength shifts for bacterial adsorption. Again notice that due to the limited penetration depth of the evanescent field, the bacterial wavelength shift is much smaller than predicted by the simple theory described by eq. (I2.11) (dashed line in Fig.I2.3). Notice also, that both theories (I2.6) and (I2.11) predict a wavelength shift linear with the surface density of adsorbed bacteria in agreement with the experiment. Not surprisingly, there are no interactions between neighboring bacteria, which are more than 1 μm apart.

Figure I2.3: Experimental data of *E.coli* wavelength shift, predicted shift by the simple theory (I2.11, Chapter F) and by the evanescent field corrected theory (I2.6).

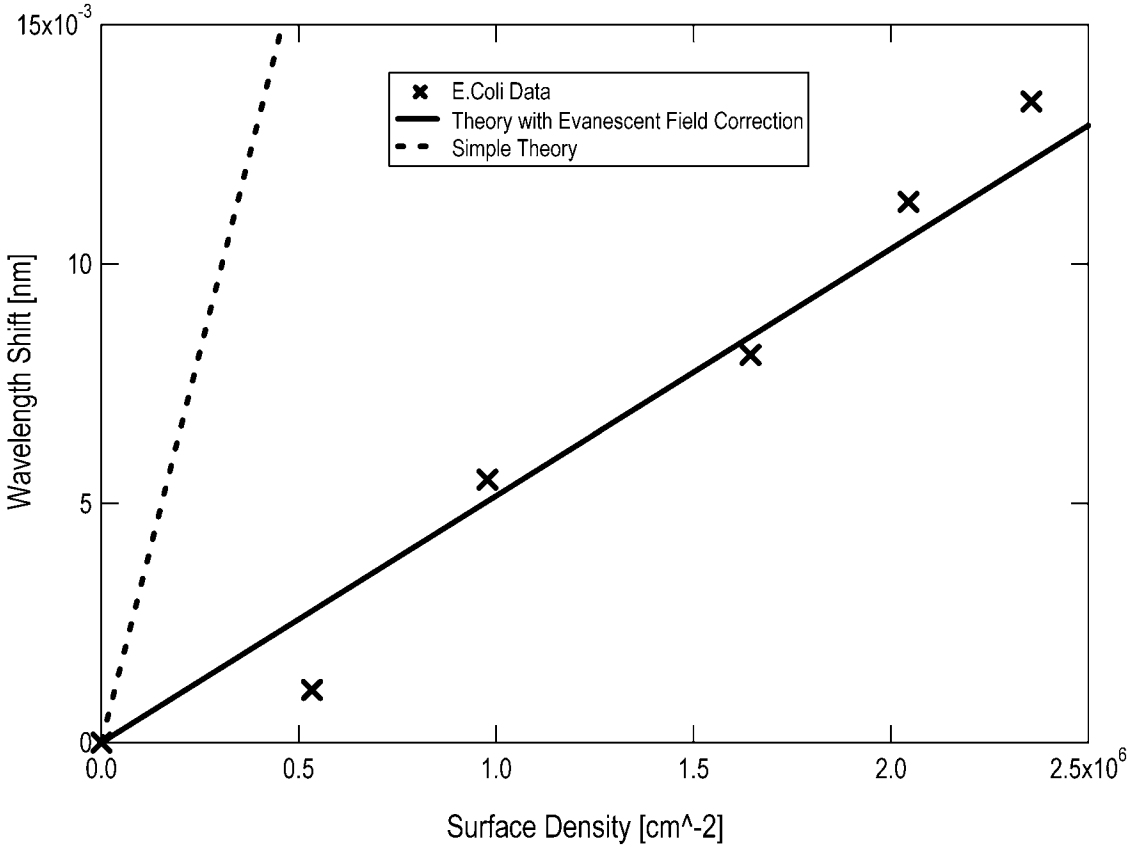

Fig. I2.4 shows a cross sectional area of the previous 3D plot I2.2 for a surface density of 2.5 x 10^6 bacteria/cm^2 (a saturation value we reached in the adsorption experiments with *E.coli*). The plot shows that the wavelength shift of adsorbed bacteria varies non-linearly with their effective spherical volume – a result not predicted for small molecules.

Figure I2.4: Wavelength shift predicted by eq. (I2.6) as a function of the effective particle volume.

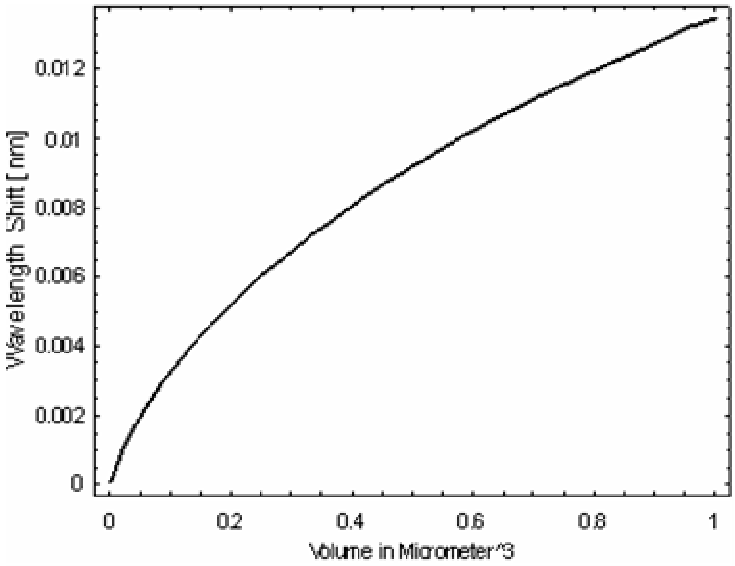

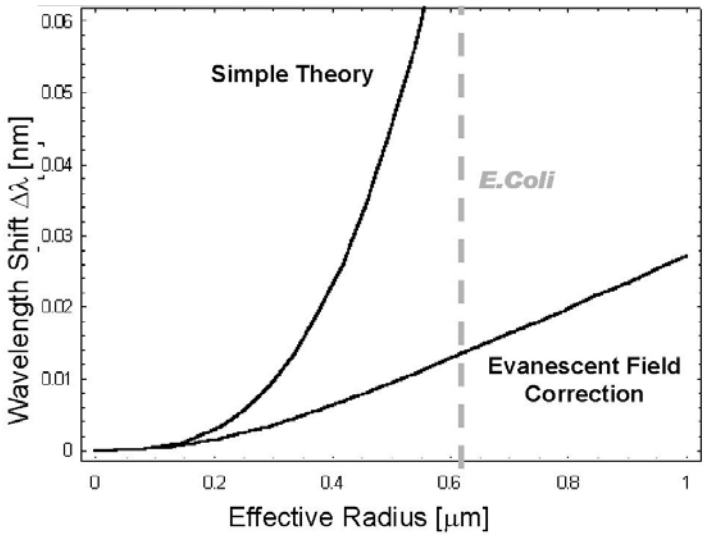

Figure I2.5: Wavelength shift predicted by eq. (I2.6), simple theory) and eq. (I2.11, with evanescent field correction). Notice that for detection of a large object such as *E.coli* the evanescent field correction is rather significant.

As mentioned before, the two theories represented by equations (I2.6) and (I2.11) agree for small objects such as nanometer sized molecules. Fig I2.5 shows a plot of the predicted wavelength shifts for spherical objects with a refractive index equal to *E.coli* (n=1.387) plotted versus the effective radius of the spherical entities. We realize that equation (I2.11, Chapter F) can be used with good approximation for wavelength shift predictions involving adsorption of molecules with up to 100 nm. For the case of BSA (< 8 nm), we calculate less than 1% error when using eq. (I2.11).

I3 - Material and Methods in Chapter I

Poly-L-Lysine Hydrogel: Microspheres are fabricated with a butane/nitrous oxide flame and plasma cleaned as described before. They are then incubated with a hanging drop of 10% poly-l-lysine (70 kD) solution (Sigma) until dry. The modified spheres are then carefully dipped in water for ~5 minutes to remove excessive poly-l-lysine. Poly-l-lysine forms a physisorpt hydrogel on the microsphere surface.

***E.coli* stock:** A ampicillin resistant laboratory strain of *E.coli* K12 is grown to saturation in 10 ml LB medium containing 10 μg/ml ampicillin. The bacteria are then sedimented in an Eppendorf centrifuge at 8000 rpm. Sedimented *E.coli* are resuspended in 1ml PBS buffer. Resuspended cells are sedimented at 12 000 rpm in an Eppendorf centrifuge and again resuspended in 1 ml PBS buffer. This washing procedure is repeated 3 times.

***E.coli* adsorption**: Poly-L-Lysine modified microspheres of ~ 400 μm diameter are mounted in the PBS filled sample cell. After equilibration, 10 μm *E.coli* suspension is added and the suspension is mixed briefly with a hypodermic needle. The resonance wavelength shift due to accumulation of bacteria on the poly-l-lysine surface is recorded as described before. Fig. I1.1 shows false-color pictures taken with a conventional 20 x and 40 x objective, respectively. The fiber runs through the center of the image. Only ~ 0.1% of *E.coli* used in this experiment seem to develop a flagellum as identified by straight, fast motion of the bacteria in the movie.

I4 Q-Spoiling with Bacterial Adsorption

In previous experiments we were examining the perturbation of nanometer sized objects on the microsphere resonances. We observed a red shift of the resonance wavelength for protein as well as DNA binding, which could be quantitatively interpreted by an accurate, analytic theory. The line width (Q-factor) of a resonance, however, did not change.

For the adsorption of large macroscopic objects such as *E.coli* I make a new observation. Cumulative binding of bacteria to the poly-l-lysine modified microsphere is not only associated with a red shift of the resonance wavelength (correctly predicted by equation (I2.6), but also with a broadening of the linewidth (Fig. I1.3).

E.coli is an inhomogenous, rodlike object. The size is comparable to the wavelength, which leads to significant scattering by the bacterial object itself. Scattering due to the bacterial cells perturbing the microsphere resonance is the cause of the broadening of the resonance line width.

The linewidth broadening can be calculated as eq. (I2.5):

$$\Gamma = \frac{16\pi}{27}\frac{\sigma\left(n_{bacteria}-n_{buffer}\right)^2\omega^4 a^6}{\left(n_{cavity}^2-n_{buffer}^2\right)R}F(2ka) \quad \text{Eq (I4.1)}$$

with

$$\frac{\Delta\lambda_{linewidth}}{\lambda_0}=\frac{\Gamma}{\omega},\ 2ka=\frac{4\pi a}{\lambda_0} \text{ and } \omega=\frac{2\pi}{n_{buffer}\lambda_0}.$$

Here, the form factor F describes the reduction of scattering amplitude associated with a spherical object of effective radius a embedded in an evanescent field of limited penetration depth.

For *E.coli* we use the previously determined effective radius a = 0.62 μm, corresponding to the *E.coli* volume of 1 μm^3. If we plot the line width versus surface density of *E.coli*, we find the line width broadening (Q-spoiling) per unit surface density to be larger as predicted (dashed line, Fig. I4.1):

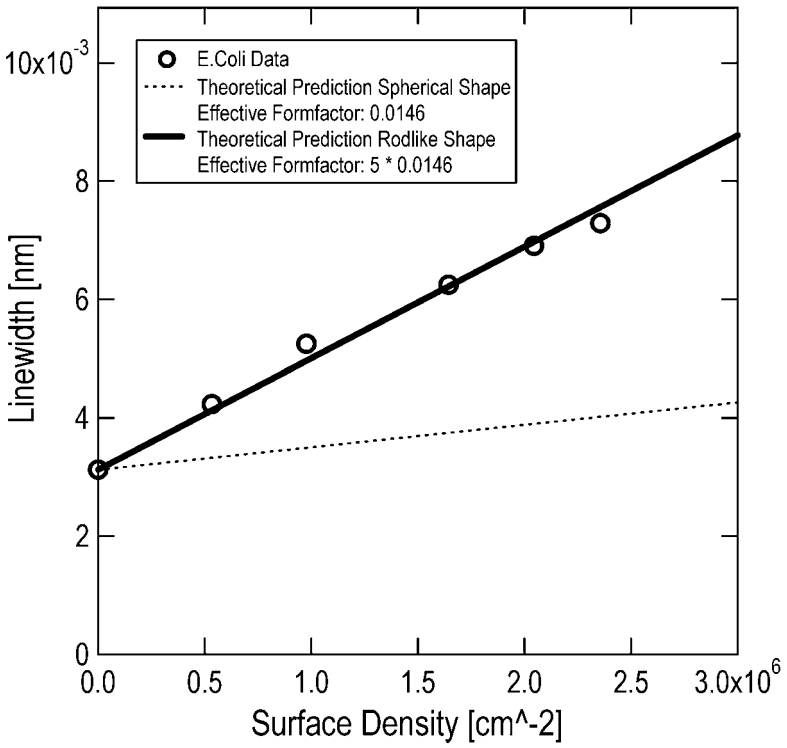

Figure I4.1: Linewidth broadening due to bacterial adsorption (circles). Predicted linewidth broadening using the theoretical effective formfactor for a homogenous sphere (dashed line) and 5 times the effective form factor (solid line), which might be attributed to the *E.coli* shape and the bacterial refractive index profile.

How can we explain this discrepancy? There might be other loss-mechanisms increasing the observed linewidth broadening associated with the inhomogeneous refractive index of bacteria and the rodlike shape of the object. We measure (fig. I4.1) that the form factor f has to be corrected by a factor of 5 to agree with our experimental results.

We realize that our bacterial sensor already forms a useful instrument for detecting bacterial titers on surfaces. Further technical improvements increasing the sensitivity will make it possible to determine the size and refractive index of an unknown bacteria. It should be possible to reach a sensitivity level, where the binding event of single bacteria can be determined from a step in the wavelength shift signal. It would then be possible to plot a histogram of the size distribution of all surface bound bacteria. Such a sensor might be ideal to study biological processes on the bacterial level such as lysis by phages or enzymes.

J Pairing Effect with Dielectric Nanospheres

From our theoretical analysis we realize that it is the induced molecular dipole moment that leads to the observed wavelength shift for adsorbents on the microsphere cavity. This microsphere sensor is an instrument which relates microscopic, molecular properties of dielectric matter to the macroscopic observable wavelength shift. This device is an ideal platform to study the induced dipole moment of surface bound entities such as molecules – or larger objects such as dielectric nanospheres (spheres on the order of several hundred nanometers in diameter).

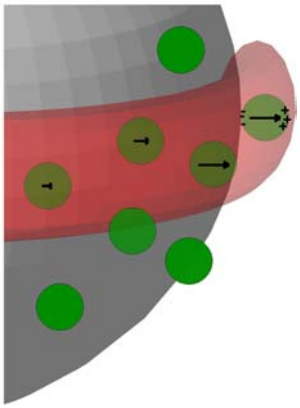

Figure J.1: Molecules or particles (called "nanospheres") binding on the equator of the microsphere get polarized at optical frequencies in the evanescent field associated with the cavity resonance.

It is an ongoing effort to predict macroscopic properties of dielectric matter such as the refractive index from the microscopic nature of the individual molecule. This theoretical analysis which represents the bridge between micro- and macrocosmos is the hallmark of thermodynamics. Quantum chemistry allows the calculation of the dipole moment associated with a multi-polar molecule. Predictions seem accurate for dilute phases such as gases: the refractive index can be calculated by integrating over all molecular contributions. In most condensed phases such as liquids, however, the calculations become more complicated due to dipole-dipole and other interactions of closely spaced molecular components. In simple cases, predictions are accurate if the mean-field of the dipole-dipole interaction is taken into account for example in the theory developed by Clausius-Mossotti.

The quantitative nature and high sensitivity of our sensor allows us to study dipole and multipolar interactions in greater detail. Molecules which bind to the equator of the microsphere surface are polarized at optical frequencies by the evanescent field (fig. J.1). Similar as for the refractive index, dipole-dipole interactions are expected to have an

effect on the magnitude of the observed wavelength shift. The high sensitivity of our sensor allows us to examine even smallest coupling effects between polarized molecules. As a test case we will examine the interaction between nanoscopic, spherical polystyrene particles.

Polystyrene particles (n = 1.59) with a diameter larger than 100 nm are highly polarizable entities. Surface immobilization of such polarizable objects (which I will refer to as nanospheres) on the microsphere cavity leads to the formation of a 2D phase of objects, which are likely to influence each other through the evanescent field induced dipole moments. The sensitivity of this system is high enough to study the onset of these interactions for low nanosphere surface concentrations. The use of fluorescent spheres allows us to directly relate surface density and wavelength shift for nanospheres as small as 50 nm in radius. the two important parameters of surface density and nanosphere size can be controlled by diffusive adsorption of polystyrene spheres of different diameters (100 nm, 210 nm and 500 nm).

J1 - Pairing Effect

The following plot (fig. J1.1) shows the observed wavelength shift of a microsphere resonance due to polystyrene nanospheres stably bound to the microsphere surface at specific surface densities. The experiment is repeated for microspheres of two different diameters: 100 nm and 210 nm. For 210 nm diameter nanospheres we observe an anomalous effect: the wavelength shift is far larger than predicted and non-linear in nature (top data set, fig. J1.1)! The anomalous shift for 210 nm diameter polystyrene nanospheres can be fit with a quadratic function which indicates a pairing effect.

The 210 nm diameter polystyrene nanospheres are on the order of a quarter wavelength und thus mark the transition between the Rayleigh and the Mie regime. Notice that both our theories (with or without evanescent field correction) agree and predict the correct wavelength shift for 100 nm diameter Rayleigh nanospheres. Nanospheres with a

diameter on the order or larger than a quarter wavelength, however, start to behave differently: a bound nanosphere seems to sense the presence of its neighbors: the wavelength shift becomes quadratic in nature.

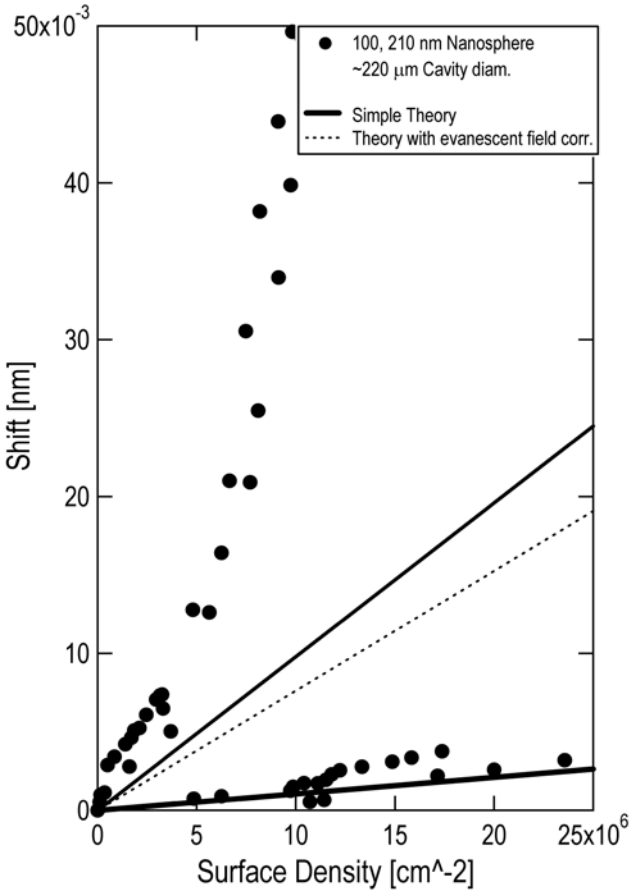

Figure J1.1: Anomalous wavelength shift for Mie nanospheres. Wavelength shift (full circles) due to nanospheres of two sizes (top and bottom data set) binding to a microsphere cavity of 220 μm diameter. For 210 nm diameter nanospheres we observe an anomalous "super" shift: the magnitude is far larger than expected and quadratic in nature. Theoretical predictions using the simple theory with eq. (I2.11, Chapter F, solid line) or the evanescent field corrected theory with eq. (I2.6, dashed line) would predict a much smaller wavelength shift for such nanospheres of 210 nm diameter. The two theories agree, however, for nanospheres of 100 nm diameter: then dashed and solid line lie on top of each other.

We can phenomenologically introduce a dimensionless parameter in order to describe the pairing effect. The main physical parameters involved in this problem are microsphere cavity radius R, nanosphere radius a, nominal laser wavelength λ_0 and nanosphere surface density σ.

I observe the effect to scale quadratically with the surface density and at a higher order with the nanosphere radius. It seems intuitively correct to introduce a dimensionless correction parameter σa^2 in the previous developed formula to describe the non-linearity of the anomalous wavelength shift.

Furthermore, the particles producing the non-linear shift are on the order of about a quarter wavelength. We have to treat them as Mie-particles and introduce a dimensionless parameter a / λ_0. We take this parameter to the third power to account for possible dipole-dipole interactions. Our intuitively arrived at formula predicting the fractional shift in wavelength, $\Delta\lambda / \lambda_0$, now takes the following form (C is a constant which is to be determined from the experiment):

$$\frac{\Delta\lambda}{\lambda} = \frac{\sigma\alpha_{ex}}{\varepsilon_0\left(n_{cavity}^2 - n_{buffer}^2\right)R}\left[1 + c\left(\frac{4\pi a}{\lambda}\right)^3 \sigma a^2\right] \qquad \text{Eq (J1.1)}$$

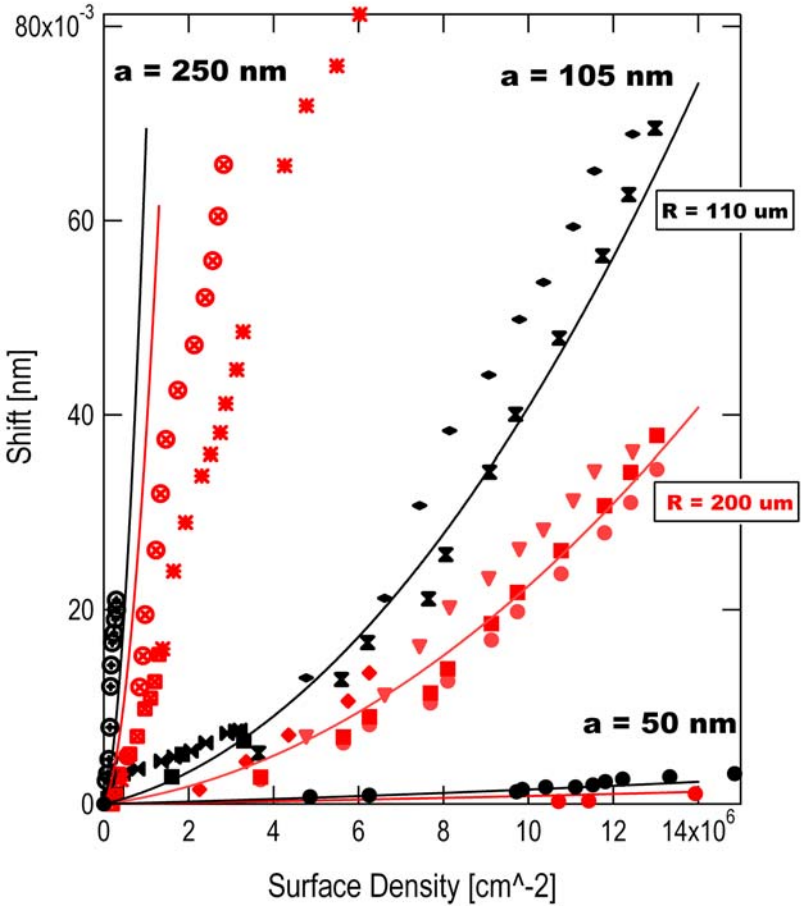

Figure J1.2: Wavelength shift measured for three different nanosphere sizes (of radius a = 50, 105 and 250 nm). The data is taken for two microsphere cavity sizes (black: radius R = 110 μm and red: radius R = 200 μm). The solid lines are calculated from eq. J1.1 using **C = 2500**!

Fig. J1.2 shows the measured wavelength shift for three different nanosphere radii (a = 50 nm, 105 nm and 250 nm). For each nanosphere size, the wavelength shift is shown for two different microsphere cavity sizes (R = 110 μm in black, R = 200 μm in red).

The solid lines show the prediction from equation (J1.1). Using this formula to fit our data we determine the coupling coefficient C as surprisingly large: **C = 2500**. We notice how well our phenomenological equation predicts the actual experimental data.

The adsorbed nanospheres produce a pronounced nonlinear σ dependence of the wavelength shift. The theoretical explanation is more challenging as compared to bacterial adsorbents because of the relatively large $\Delta\varepsilon = n^2_{\text{polystyrene}} - n^2_{\text{water}} = (1.59^2 - 1.33^2)$ which prohibits the use of certain theoretical approximations. The following analytical calculations of the pairing effect have been developed by Hai-Cang Ren.

We are dealing with a Mie scattering problem for which analytic techniques have not been well developed. The mechanisms that may contribute include: 1) the second order Born approximation of the mean field potential, 2) the coupling between two nanospheres via non-resonance modes; 3) the coupling among WGM of different azimuthal quantum number through the slight ellipticity of the cavity. On writing the line shift as:

$$\frac{\delta\lambda}{\lambda} = \left(\frac{\delta\lambda}{\lambda}\right)_{\text{linear}} \left(1 + C\sigma a^2\right), \qquad \text{Eq (J1.2)}$$

the contributions to C, according to Hai-Cang Ren's up to date analysis are summarized in the table below.

Table J1.1. Selected contributions to C

The mechanism	The contribution to C
The second order in the mean field	$C_1 \dfrac{\Delta\varepsilon}{\varepsilon_{\text{cav.}} - \varepsilon_{\text{sol.}}}$
Coupling via non-resonance modes	$C_2 \Delta\varepsilon^2$
Small ellipticity	$C_3 \dfrac{\Delta\varepsilon^2 a^3}{(\varepsilon_{\text{cav.}} - \varepsilon_{\text{sol.}})^2 R^3 \delta^2}$

The coefficients C_1, C_2 and C_3 are functions of $\frac{2\pi a}{\lambda}$. The dependence on the cavity radius, *R,* of the first and the second contributions is consistent with the observation but with a coefficient one order of magnitude smaller. The third contribution can be made closer to the observed magnitude at cost of fine tuning the *R* dependence of the eccentricity of the cavity, here δ. Other effects such as weak localization might also contribute to the total "super" shift. There might also be a novel coupling mechanism involved. Another possibility is the coupling of polarized spheres through the various radial modes of the microsphere cavity.

For nanospheres larger than 100 nm in diameter we also observe a linewidth broadening (fig. J1.3).

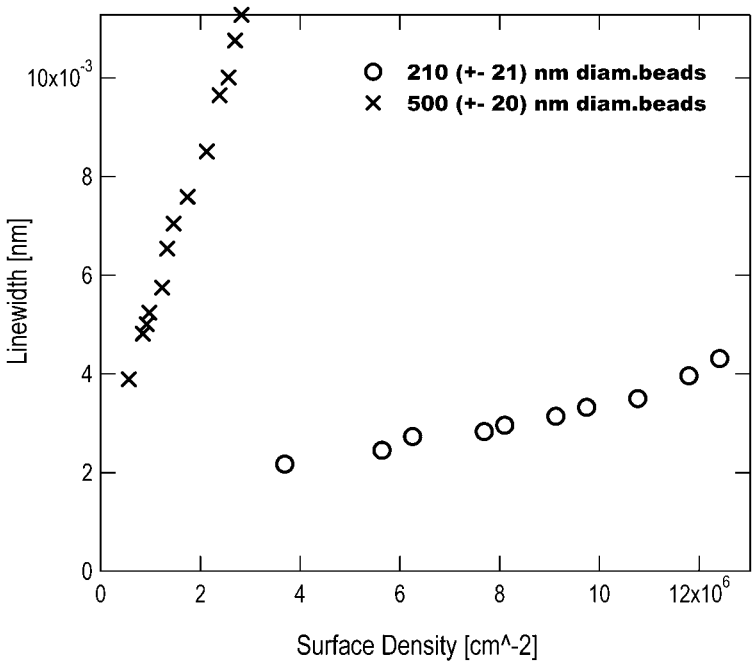

Figure J1.3: Linewidth broadening due to nanosphere of two different sizes (250 nm and 500 nm diameter) adsorbing to the microsphere cavity.

The increase of linewidth seems linear with increasing nanosphere surface density. Fig. J1.3 shows the linewidth spoiling for two nanosphere sizes: 210 nm and 500 nm diameter. Interestingly, the onset of a measurable pairing effect and the onset of a measurable linewidth broadening is coinciding for nanospheres with a diameter of about a quarter wavelength or larger. Both effects, the onset of non-linear "super"-wavelength shift and the linewidth reduction, seem to mark the transition between the Rayleigh and the Mie regime.

J2 - Materials and Methods in Chapter J

Fluorescent Imaging of Nanospheres: The Zeiss Axioskop - used to observe the liquid filled sample cell from above - was modified with an upright mounted, cooled CCD camera. A Xenon lamp was installed in the fluorescent port of the microscope. The filter cube of the microscope was equipped with excitation and emission filters as well as a beamsplitter for detection of the yellow-green fluorescent nanospheres. The nanospheres are carboxylated, fluorescent polystyrene spheres (n = 1.59) with radii of a = 50 nm, 105 nm and 250 nm (Molecular Probes). The carboxyl-groups introduce a net negative charge on each nanosphere (in neutral buffer) which is necessary in order to stably adsorb the polystyrene spheres to the previously plasma cleaned silica microsphere in PBS buffer. The cooled CCD camera images a part of the surface of the microsphere sensor through a standard 20x – 40x objective. Images are recorded and digitally stored on a PC. The saved images are later analyzed by determining the surface density of bound nanospheres by simple counting of the fluorescent, surface bond nanospheres. Each image represents an average of several exposures which makes it easy to identify the bound nanospheres as glowing spots on the microsphere surface. Counts range from 1 to 100 depending on surface density and magnification. In a typical experiment I inject 10-100 μl of a pre-diluted nanosphere solution in the 1 ml sample cell filled with PBS buffer. Surface adsorption of nanospheres is then recorded. In parallel, the computer records resonance position and linewidth of microsphere resonances detected in the transmission spectrum. Images are correlated with the shift and linewidth data using the common time stamp of each image and spectrum.

K Comparison with Existing, Label-free Biosensing Techniques

Optical techniques for the detection of biomolecules are among the most widely used methods in the life sciences: more than 3000 articles have been published over the past 12 years (Rich, 2002). Such biosensing approaches are especially useful if there is no need for a label on the sample analyte. Examples are the notorious surface plasmon

detectors (for example the Biacore instrument line; www.biacore.com) and other emerging optical biosensors (Baird, 2001). Many optical sensor technologies are still on the basic development level and will emerge with their specific applications in the near future (e.g. sensors based on porous silicon: Cunin, 2002; Li, 2003; Lin, 1997; sensors based on optically coated silicon: Jenison, 2001; and sensors based on optically probed cantilevers: Fritz, 2000).

Labeling of the sample analyte can be impossible in some cases or it can alter the relative concentrations of targets originally present thus introducing a systematic error in comparative measurements. An optical technique for *label-free* molecular interaction analysis which has recently drawn a lot of attention is based on the optical phenomena of surface plasmon resonance. A light ray internally reflected in a prism excites a plasmon resonance in the gold film deposited on the prism. Only for a specific incidence angle of the prism-reflected light is there a maximum coupling to the plasmon resonance. A scan of the light ray for different incident angles thus identifies the plasmon resonance at a specific angle for which the transmission is minimal. Binding of molecules to the modified gold surface locally changes the refractive index which leads to a change of this specific plasmon resonance angle. The change of angle is proportional to the mass-loading on the gold coated prism surface. Detection limits can reach 10 pg/mm^2 and have been reported for detection of label-free proteins (www.biacore.com).

A similar popular biosensor uses the electrical resonance excited in a quartz crystal. Such a quartz crystal microbalance is sensitive to a change of mass deposited on the crystal surface such as described for the mass on a spring in Chapter B. When used with biomolecules, detection limits reach typically 50 pg/mm^2.

To our knowledge, surface plasmon resonance sensors and quartz-crystal microbalances are the most sensitive optical biosensors without utilizing any labels. How does our technique compare with those commercially available, optimized instruments?

In a typical experiment, I use a glass microsphere of radius R = 50 μm to detect protein mass loading. Proteins have a typical excess polarizability of α_{ex} = $4 \pi \varepsilon_0 \times 4.3 \times 10^{-21}$ cm^3. In such a typical experiment we measure the linewidth of a given resonance as $d\lambda = 0.66$ pm corresponding to a Q of $Q = 2 \times 10^6$. Our program locates the position of the resonance with a parabolic minimum fit. This typically results in a precision of the resonance position (the minimum) within 1/50 of the linewidth. The effective Q_{eff} is thus on the order of 10^8.

Our theory predicts the wavelength shift due to a single molecule binding to the equator of the microsphere as (Arnold, 2003):

$$\left(\frac{\Delta\lambda}{\lambda}\right)_{molecule} = \frac{\alpha_{ex} EF}{4\pi\varepsilon_0 (n_s^2 - n_m^2) R^3} \qquad \text{Eq.(K.1)}$$

I can calculate the smallest fractional shift from the measured effective Q as:

$$\left(\frac{\Delta\lambda}{\lambda}\right)_{device} = Q_{eff}^{-1} \qquad \text{Eq. (K.2)}$$

I thus determine the detection limit in terms of smallest number of detectable protein molecules N_D as:

$$N_D = \left(\frac{\Delta\lambda}{\lambda}\right)_{device} / \left(\frac{\Delta\lambda}{\lambda}\right)_{molecule} = 5280 \qquad \text{Eq. (K.3)}$$

The experimentally reached detection limit of this device is ~ 5000 BSA molecules. This is however not an ultimate limit and there is a lot of room for improvement of this analytic sensing platform. Using a sapphire microsphere with a refractive index of n = 1.7 it should be possible to decrease the microsphere radius from 50 μm down to 3.6 μm where the sapphire sphere should still be able to host high-Q resonances. Since the enhancement factor EF scales as the square root of microsphere radius R, the smallest detectable fractional shift in wavelength scales with microsphere radius R as:

$$\left(\frac{\Delta\lambda}{\lambda}\right)_{device} \propto \frac{1}{R^{5/2}} \qquad \text{Eq. (K.4)}$$

One can use a microsphere of 3.6 μm radius and operate it at a wavelength of 400 nm. At this smaller wavelength one can benefit from a lower absorption by water which will increase the Q-factor. If it is possible to maintain the Q of the smaller, higher refractive index sphere at about 10^{7-8} we calculate a more than 5000 times increase in sensitivity: enough to detect a single, label-free BSA molecule in an aqueous environment.

The following table shows how our current sensor setup compares with SPR and QCM devices in terms of smallest detectable protein mass-loading.

QCM	50 pg/mm^2
SPR	10 pg/mm^2
Microsphere Resonator	1 pg/mm^2

Another advantage of our device is the possibility for miniaturization. Besides the sensitivity, size and geometry are important issues for any biosensor (Suzuki, 2001). Ideally, a biosensor would be small enough to fit inside a single eukaryotic cell which is several micrometers in diameter. Such a sensor could be used for single-cell gene expression profiling (Levsky, 2002). To reach this miniaturization goal it might be useful to change the detector geometry by "pig-tailing" the microsphere to the optical fiber (Ilchenko, 1999).

Different geometries might also be explored to form an ionic reservoir between the silica surface and a tethered membrane. Such a silica-membrane sensor could be used as a biosensor utilizing ion-channel switches (Cornell, 1997). A hollow microsphere detector with a stream of analyte flushing through its interior could open up a wealth of interesting applications in analytical chemistry.

Multiplexing of many microspheres to one waveguide might lead to an array type sensor useful for high-throughput screening of antibody-antigen interactions (de Wildt, 2000).

Integration of all components on a microfabricated chip will be another approach for miniaturization using flat waveguides coupled to disk resonators. Recently it has been shown that toroid microcavities on a chip can be manufactured with an ultra-high Q (Armani, 2003). Other examples are a polymer microring resonator fabricated by nanoimprint techniques (Guo, 2002; Guo 2003) and a refractive index sensor based on an integrated optical microcavity (Krioukov, 2002) as well a microdisks fabricated from indiumphosphate (Choi, 2002). A different coupling geometry between fiber and microsphere might also allow a smaller design. For this purpose, the microsphere could be "pig-tailed" to the optical fiber as mentioned before (Ilchenko, 1999). Extreme miniaturization using such an approach could lead to the first single cell biosensor. A monolithic biosensor chip would also increase robustness for use of our system as a small, field-able detector. Such robust detectors could find their use for water quality monitoring (Anderson, 2001), for applications in food analysis (Luong, 1997), for medical-diagnostic purposes in cancer research (Maesawa, 2003) or for viral detection (Cole, 1995).

Another yet unexplored possibility of this analytic platform is the analysis of frequency shifts related to the two differently polarized resonant modes: TE and TM. Such a refined analysis will allow to detect orientation and conformational changes of surface-bound molecules. This is a very important analytic aspect for any label-free detection system and is currently investigated for e.g. surface plasmon resonance based devices (Flatmark, 2001; Gestwicki, 2001; Ozawa, 2000; Paynter, 2002; Sota, 1998; Stokka, 2003; Zako, 2001). By scanning over a much broader spectral width our sensor might be useful as a true spectrometer revealing the structure of the analyte.

With this thesis we believe to have opened up the field of resonant biosensing. Although high-Q resonance of light had been studied widely this is the first demonstration of their use for biodetection. WGM seem the ideal choice to build what might well be the world's most sensitive biosensor. Applications seem plentiful not only as sensing devices but also as bio-optical components in computers and robots of the future. The highest sensitivity might allow for experiments important for emerging nanotechnologies.

L References

Abel, A.P, Weller, M.G., Duveneck, G.L., Ehrat, M., Widmer, H.M. "Fiber-Optic Evanescent Wave Biosensor for the Detection of Oligonucleotides" *Anal. Chem.* **68**, 2905-2912 (1996).

Anderson, G.P., Rowe-Taitt, C.A. "Water quality monitoring using an automated portable fiber optic biosensor: RAPTOR", *SPIE Proceedings* **4206** (2001).

Arnold, S., Camunale, J., Whitten, W.B., Ramsey, J.M., Fuller, K.A. "Room Temperature Microparticle Based Persistend Hole-Burning Spectroscopy" *J.Opt.Soc.Am.B* **9**, 819-823 (1992).

Arnold, S. "Microspheres, Photonic Atoms, and the Physics of Nothing" *American Scientist* **89**, 214-221 (2001).

Arnold, S., Holler, S. "Microparticle Photophysics: Fluorescence Microscopy and Spectroscopy of a Photonic Atom" in Cavity Enhanced Spectroscopies, Eds.R.D.Van Zee and J.P.Looney, pp.227-253, Aademic Press (2002).

Arnold S., Khoshsima M., Teraoka I., Holler S., Vollmer F., "Shift of Whispering-Gallery Modes in Microspheres by Protein Adsorption", *Optics Letters* **28**, 272-274 (2003).

Arnold, S., Noto, M., Vollmer, F. "Consequences of extreme photon confinement in micro-cavities: I. Ultra-sensitive detection of perturbations by bio-molecules" in *Frontiers of Optical Spectroscopy: Investigating Extreme Physical Conditions with Advanced Optical Techniques.* Ed. Baldassare diBartolo (Kluwer Publishers, in press 2004).

Armani, D.K., Kippenberg, T.J., Spillane, S.M., Vahala, K.J. "Ultra-high Q toroid microcavities on a chip" *Nature* **421**, 925-928 (2003).

Baird, C.L., Myszka, D.G. "Current and emerging commercial optical biosensors" *Journal of Molecular Recognition* **14**, 261-268 (2001).

Black, R.J., Bourbonnais, R. "Core-Mode Cutoff for Finite-Cladding Lightguides" *IEEE Proceedings J.***133**, 377-384 (1986).

Boucouvalas, A.C., Georgiou, G. "Tapering of Single-Mode Optical Fibers", *IEE Proceedings J.* **133**, 385-392 (1986).

Boyd, R.W., Heebner, J.E. "Sensitive disk resonator photonic biosensor" *Applied Optics* **40**, 5742-5747 (2001).

Cai, M., Hunziker, M.G., Vahala, K.J. "Fiber-optic add-drop device based on a silica microsphere-whispering gallery mode system" *IEEE Photon.Technol.Lett.* **6**, 686-687 (1999).

Cai, M., Painter, O., Vahala, K.J. "Observation of critical coupling in a fiber taper to a silica-microsphere whispering-gallery mode system" *Phys.Rev.Lett.* **85**, 74-77 (2000).

Cai, M. "Optical Fiber Taper Coupled Glass Microsphere Resonators" Thesis. California Institute of Technology (2001).

Chao, C-Y., Guo, L.J. "Polymer microring resonators fabricated by nanoimprint technique" *J.Vac.Sci.Technol.B* **20**, 2862-2865 (2002).

Chao, C.-Y., Guo, L.J. "Biochemical sensors based on polymer microrings with sharp asymmetrical resonance" *Applied Physics Letters* **83**, 1527-1529 (2003).

Ching, E.S.C., Leung, P.T., Young, K. "Optical Processes in Microcavities – The Role of Quasinormal Modes" in Optical Processes in Microcavities, Ed. By R.K. Chang and A.J. Campillo, World Scientific, Singapore (1996) p.11.

Choi, K.H., Bouroin, J.P., Auvray, S., Esteve, D., Duesberg, G.S., Roth, S., Burghard, M. "Controlled deposition of carbon nanotubes on a patterned substrate" *Surface Science* **462**, 195-202 (2000).

Choi, S.J., Djordjev, K., Choi, S.J., Dapkus, P.D. "CH_4-based dry etching of high Q InP microdisks" *J.Vac.Sci.Technol.B* **20**, 301-305 (2002).

Chrisey, L.A., Lee, G.U., O'Ferrall, C.E. "Covalent attachment of synthetic DNA to self-assembled monolayer films" *Nucleic Acids Research* **24**, 3031-3039 (1996).

Cole, T., Kathman, A., Koszelak, S., PcPherson, A. "Determination of Local Refractive Index for Protein and Virus Crystals in Solution by Mach-Zehnder Interferometry" *Analytical Biochemistry* **231**, 92-98 (1995).

Cornell, B.A., Braach-Maksvytis, V.L.B., King, L.G., Osman, P.D.J., Raguse, B., Wieczorek, L., Pace, R.J. "A biosensor that uses ion-channel switches" *Nature* **387**, 580-583 (1997).

Cunin, F., Schmedake, T.A., Link, J.R., Li, Y.Y., Koh, J., Bhatia, S.N., Sailor, M.J. "Biomolecular screening with encoded porous-silicon photonic crystals" *Nature Materials* **1**, 39-41 (2002).

Diehl, F., Grahlmann, S., Beier, M., Hoheisel, J.D. "Manufacturing DNA microarrays of high spot homogeneity and reduced background signal" *Nucleic Acids Research* **29**, e38 (2001).

Dolan, P.L., Wu, Y., Ista, L.K., Metzenberg, R.L., Nelson, M.-A., Lopez, G.P. "Robust and efficient synthetic method for forming DNA microarrays" *Nucleic Acids Research* **29**, e107 (2001).

Engelbrecht, R., Brand, H., Schmidth, L.-P. "Sensitive Simultaneous Detection of CO and CO_2 with Commercial DFB Diode Lasers for Optical Communications Systems" *Proceedings 6.Conference on Infrared Sensors and Systems (IRS)* (2000).

Hill, S.C., Brenner, R.E. “Morphology-Dependent Resonances” in *Optical Effects Associated with Small Particles*, Ed. By P.W. Barber and R.K. Chang, World Scientific, Singapore (1988).

De Wildt, R.M.T., Mundy, C.R, Gorrick, B.D., Tomlinson, I.M. “Antibody arrays for high-throughput screening of antibody-antigen interactions” *Nature Biotechnology* **18**, 989-994 (2000).

Dubruil, N., Knight, J.C., Leventhal, D.K., Sandoghdar, V. Hare, J., Lefevre, V. “Eroded Monomode Optical Fiber for Whispering-Gallery Mode Excitation in Fused-Silica Microspheres” *Opt. Lett.* **20**, 813 (1995).

Fang, X., Tan, W. “Imaging Single Fluorescent Molecules at the Interface of an Optical Fiber Probe by Evanescent Wave Excitation” *Analytical Chemistry* **1999**, 3101-3105 (1999).

Feynman, R.P., Leighton, R.B., Sands, M. “The Feynman Lectures on Physics”, Addison-Wesley Publishing, California Insititute of Technology (1963).

Flatmark, T., Stokka, A.J., Bere, S.V. “Use of Surface Plasmon Resonance for Real-Time Measurements of the Global Confromational Transition in Human Phenylalanine Hydroxylase in Response to Substrate Binding and Catalytic Activation” *Analytical Biochemistry* **294**, 95-101 (2001).

Fowles, G.R., Cassidy, G.L.”Analytical Mechanics”, Sixth Edition, Saunders College Publishing, New York (1999).

Fritz, J., Baller, M.K., Lang, H.P., Rothuizen, H., Vettiger, P., Meyer, E., Guentherodth, H.-J., Gerber, Ch., Gimzewski, J.K. “Translating Biomolecular Recognition into Nanomechanics” *Science* **288**, 316-318 (2000).

Gestwicki, J.E., Hsieh, H.V., Pitner, J.B. “Using Receptor Confromational Change To Detect Low Molecular Weight Analytes by Surface Plasmon Resonance” *Anal.Chem.* **73**, 5732-5737 (2001).

Griffel, G., Arnold, S., Taskent, D. “Excitation of Morphology Dependent Resonances of Microspherical Cavities Using Optical Fibers” *Optics & Photonics News* December, 21-22 (1995).

Griffel, G., Arnold, S., Taskent, D. Serpenguezel, A., Connolly, J., Morris, N. “Morphology dependent resonances of a microsphere, optical fiber system” *Optics Letters* **25**, 695-697 (1996).

Gorodetsky, M.L., Savchenkov, A.A., Ilchenko, V.S. “Ultimate Q of optical Microsphere Resonators”, *Optics Letters* **21**, 453-455 (1996).

Graham, C.R., Leslie, D., Squirrell, D.J. “Gene probe assays on a fibre-optic evanescent wave biosensor” *Biosensors & Bioelectronics* **7**, 487-493 (1992).

Gregorius, K., Mouritsen, S., Elsner, H.I. “Hydrocoating: a new method for coupling biomolecules to solid phases” *Journal of Immunological Methods* **181**, 65-73 (1995).

Healey, B.G., Matson, R.S., Walt, D.R. “Fiberoptic DNA Sensor Array Capable of Detecting Point Mutations” *Analytical Biochemistry* **251**, 270-279 (1997).

Henke, L., Piunno, P.A.E., McClure, A.C., Krull, U.J. “Covalent immobilization of single-stranded DNA onto optical fibers using various linkers” *Analytica Chimica Acta* **344**, 201-213 (1997).

Huygens, C. “Horologium Oscillatorium” (1673).

Ilchenko, V.S. et.al. “Strain Tunable High-Q Optical Microsphere Resonator”, *Opt. Commun.***145**, 86 (1998).

Ilchenko, V.S., Yao, X.S., Maleki, L. “Pigtailing the High-Q Microsphere Cavity: A Simple Fiber Coupler for Optical Whispering-Gallery Modes” *Opt. Lett.* **24**, 723 (1999).

Iler, R.K. “The Colloid Chemistry of Silica and Silicates” Cornell University Press (1955).

Jenison, R., Yang, S., Haeberli, A., Polisky, B. “Interference-based detection of nucleic acid targets on optically coated silicon” *Nature Biotechnology* **19**, 62-65 (2001).

Joos, B., Kuster, H., Cone, R. “Covalent Attachment of Hybridizable Oligonucleotides to Glass Support” *Analytical Biochemistry* **247**, 96-101 (1997).

Junhui, Z., Hong, C., Ruifu, Y. “DNA based biosensors” *Biotechnology Advances* **15**, 43-58 (1997).

Kaestner, E., Lemke, H.”Die Schildbuerger” Atrium Verlag, Zuerich (2004).

Knight, J.C., Cheung, G., Jacques, F., Birks, T.A. “Phase-matched excitation of whispering-gallery mode resonances by a fiber taper” *Optics Letters* **22**, 1129-1131 (1997).

Krioukov, E., Klunder, D.J.W., Driessen, A., Greve, J., Otto, C. “Sensor based on an integrated optical microcavity” *Optics Letters* **27**, 512-514 (2002).

Kuehner, M., Sackmann, E. “Ultrathin Hydrated Dextran Films Grafted on Glass: Preparation and Characterization of Structural, Viscous and Elastic Properties by Quantitative Microinterferometry” *Langmuir* **12**, 4866-4876 (1996).

Kumar, A., Larsson, O., Parodi, D., Liang, Z. “Silanized nucleic acids: a general platform for DNA immobilization” *Nucleic Acids Research* **28**, e71 (2000).

Kumar, A., Liang, Z. “Chemical nanoprinting: a novel method for fabricating DNA microchips” *Nucleic Acids Research***29**, e2 (2001).

Lai, H.M., Lam, C.C., Leung, P.T., Young, K. “Effect of perturbations on the widths of narrow, morphology-dependent resonances in Mie scattering” *JOSAB* **8**, 1962-1973 (1991).

Lai, H.M., Leung, P.T., Young, K. “Time-Independent Perturbation for Leaking Electromagnetic Modes in Open Systems with Application to Resonances in Microdroplets” *Phys. Rev. A* **41**, 5187-5191 (1990).

Laine, J.-P., Little, B.E., Lim, D.R., Tapalian, H.C., Kimerling, L.C., Haus, H.A. “Planar integrate wavelength-drop device based on pedestal antiresonant reflecting waveguides and high-Q silica microspheres” *Optics Letters* **25**, 1636-1638 (2000).

Lam, C.C., Leung, P.T., Young, K. “Explicit Asymptotic Formulas for the Positions, Widths, and Strengths of Resonances in Mie Scattering” *J.Opt.Soc.Am.B* **9**, 1585 (1992).

Lefevre-Seguin, V. “Whispering-gallery mode lasers with doped silica microspheres” *Optical Materials* **11**, 153-165 (1999).

Levsky, J.M., Shenoy, S.M., Pezo, R.C., Singer, R.H. “Single-Cell Gene Expression Profiling” *Science* **297**, 836-840 (2002).

Lin, V.S.-Y., Motesharei, K., Dancil, K.-P.S., Sailor, M.J., Ghadiri, M.R. “A Porous Silicon-Based Optical Interferometric Biosensor” *Science* **278**, 840-843 (1997).

Li, Y.Y., Cunin, F., Link, J.R., Gao, T., Betts, R.E., Reiver, S.H., Chin, V., Bhatia, S.N., Sailor, M.J. “Polymer Replicas of Photonic Porous Silicon for Sensing and Drug Delivery Applications” *Science* **299**, 2045-2047 (2003).

Lin, H.B., Eversole, J.D., Campillo, A.J. “Excitation localization principle for spherical microcavities” *Optics Letters* **23**, 1051-1053 (1998).

Lindroos, K., Liljedahl, U., Raito, M., Syvaenen, A.-C. “Minisequencing on oligonucleotide microarrays: comparison of immobilization chemistries” *Nucleic Acids Research* **29**, e69 (2001).

Little, B.E., Chu, S.T., Haus, H.A. “Track changing by use of the phase response of microspheres and resonators” *Optics Letters* **23**, 894-896 (1998).

Little, B.E., Laine, J.-P., Haus, H.A. “Analytic Theory of Coupling from Tapered Fibers and Half-Blocks into Microsphere Resonators” *Journal of Lightwave Technology* **17**, 704-715 (1999).

Liu, X., Tan, W. “A Fiber-Optic Evanescent Wave DNA Biosensor Based on Novel Molecular Beacons” *Anal. Chem.* **71**, 5054-5059 (1999).

Love, J.D., Henry, W.M., Stewart, W.J., Black, R.J., Lacroix, S. Gonthier, F. “Tapered Single-Mode Fibers and Devices: Part 1: Adiabaticity Criteria”, *IEEE Proceedings J.* **138**, 355-364 (1991).

Luong, J.H.T., Bouvrette, P., Male, K.B. “Developments and applications of biosensors in food analysis” *TIBTECH* **15** 369-377 (1997).

Maesawa, C., Inaba, T., Sato, H., Lijima, S., Ishida, K., Terashima, M., Sato, R., Suzuki, M. Yashima, A., Ogasawara, S., Oikawa, H., Sato, N., Saito, K., Masuda, T. “A rapid biosensor chip

assay for measuring of telomerase activity using surface plasmon resonance" *Nucleic Acids Research* **31** e4 (2003).

Nilsson, P., Persson, B., Uhlen, M., Nygren, P.-A. "Real-Time Monitoring of DNA Manipulations Using Biosensor Technology" *Anal. Biochem.* **224**, 400-408 (1995).

Noto, M, Khoshsima, M, Chang, D., Teraoka, I., Arnold, S. "Molecular Weight Sensitivity of a Photonic Atom Sensor" to be submitted to *Optics Letters* (2004).

Ozawa, T., Fukuda, M., Nara, M., Nakamura, A., Komine, Y., Kohama, K., Umezawa, Y. "How Can Ca^{2+} Selectively Activate Recoverin in the Presence of Mg^{2+}? Surface Plasmon Resonance and FT-IR Spectroscopic Studies" *Biochemistry* **39**, 14495-14503 (2000).

Paynter, S., Russell, D.A. "Surface plasmon resonance measurement of pH-induced responses of immobilized biomolecules: conformational change or electrostatic interaction effects?" *Analytical Biochemistry* **309** 86-95 (2002).

Peterson, A.W, Heaton, R.J., Georgiadis, R.M. "The effect of surface probe density on DNA hybridization" *Nucleic Acids Research* **29**, 5163-5168 (2001).

Pilevar S., Davis C.C., Portugal, F. "Tapered Optical Fiber Sensor Using Near-Infrared Fluorophores To Assay Hybridization" *Analytical Chemistry* **70**, 2031-2037 (1998).

Piunno, P.A.E., Krull, U.., Hudson, R.H.E., Damha, M.J., Cohen, H. "Fiber-Optic DNA Sensor for Fluorimetric Nucleic Acid Determination" *Analytical Chemistry* **67**, 2635-2643 (1995).

Purcell, E.M. "Electricity and Magnetism", McGraw-Hill (1985).

Ramsay, G. "DNA chips: state-of-the-art" *Nature Biotechnoloy* **16**, 40-44 (1998).

Rich, R.L, Myszka, D.G. "Survey of the year 2001 commercial optical biosensor literature" *Journal of Molecular Recognition* **15**, 352-376 (2002).

Richtmyer, R.D. "Dielectric Resonators" *Journal of Applied Physics* **10**, 391-398 (1939).

Rogers, Y.-H., Jiang-Baucom, P., Huang, Z.-J., Bogdanov, V., Anderson, S., Boyce-Jacino, M.T. "Immobilization of Oligonucleotides onto a Glass Support via Disulfide Bonds: A Method for Preparation of DNA Microarrays" *Analytical Biochemistry* **266**, 23-30 (1999).

Rosenberger, A.T., Rezac, J.P. "Evanescent-Wave Sensor Using Microsphere Whispering-Gallery Modes" *Proc. SPIE* **3930**, 186 (2000).

Sabanayagam, C.R., Smith, C.L., Cantor, C.R. "Oligonucleotide immobilization on miropatterned streptavidin surfaces" *Nucleic Acids Research* **28**, e33 (2000).

Sengupta, K., Schilling, J., Marx, S., Fischer, M., Bacher, A., Sackmann, E. “Mimicking Tissue Surfaces by Supported Membrane Coupled Ultrathin Layer of Hyaluronic Acid” *Langmuir* **19**, 1775-1781 (2003).

Serpenguezel, A., Arnold, S., Griffel, G. “Excitation of resonances of microspheres on an optical fiber” *Optics Letters* **20**, 654-656 (1995).

Serpenguezel, A., Arnold, S., Griffel, G. “Efficient Coupling of Guided Waves to Microsphere Resonances Using an Optical Fiber” *J.Opt.Soc.B* **14**, 790-794 (1997).

Song, F., Zhou, F., Wang, J., Tao, N., Lin, J., Vellanoweth, R.L., Morquecho, Y., Wheeler-Laidman, J. “Detection of oligonucleotide hybridization at femotomolar level and sequence-specific gene analysis of the *Arabidopsis thaliana* leaf extract with an ultrasensitive surface plasmon resonance spectrometer” *Nucleic Acids Research* **30**, e72-e83 (2002).

Sota, H., Hasegawa, Y. “Detection of Conformational Changes in an Immobilized Protein Using Surface Plasmon Resonance” *Anal. Chem.* **70**, 2019-2024 (1998).

Steemers, F.J., Ferguson, J.A., Walt, D.R. “Screening unlabeled DNA targets with randomly ordered fiber-optic gene arrays” *Nature Biotechnology* **18**, 91-94 (2000).

Stokka, A.J., Flatmark, T. “Substrate-induced conformational transition in human phenylalanine hydroxylase as studied by surface plasmon resonance analyses: the effect of terminal deletions, substrate analogues and phosphorylation” *Biochem.J.* **369**, 509-518 (2003).

Suzuki, M., Ozawa, F., Sugimoto, W., Aso, S. “Miniaturization of SPR Immunosensors” *Analytical Sciences* **17**, i265-i267 (2001).

Symes, R., Sayer, R.M., Reid, J.P. “Cavity enhanced droplet spectroscopy: Principles, perspectives and prospects” *Phys.Chem.Chem.Phys.* **6**, 474-487 (2004).

Teraoka, I., Arnold, S., Vollmer, F. “Perturbation Approach to Shift of Whispering-Gallery Modes in Microspheres by Protein Adsorption” *Journal of the Optical Society of America B* **20**, 1937-1946 (2003).

Thompson, J.E., Smith, B.W., Winefordner, J.D. “Monitoring Atmospheric Particulate Matter through Cavity Ring-Down Spectroscopy” *Analytical Chemistry* **74**, 1962-1967 (2002).

Tong, L., Gattass, R.R., Aschom, J.B., He, S., Lou, J., Shen, M., Maxwell, I., Mazur, E. “Subwavelength-diameter silica wires for low-loss optical wave guiding” *Nature* **426**, 816-819 (2003).

Vollmer, F., Braun, D., Libchaber, A., Khoshsima, M., Teraoka, I., Arnold, S. “Protein Detection by Optical Shift of a Resonant Microcavity” *Applied Physics Letters* **80**, 4057-4059 (2002).

Vollmer, F., Arnold, S., Braun, D., Teraoka, I., Libchaber, A. “Multiplexed DNA Quantification by Spectroscopic Shift of Two Microsphere Cavities” *Biophysical Journal* **85**, 1974-1979 (2003).

Vollmer, F., Ren, H.-C., Arnold, S., Libchaber, A. “Pairing effect of Mie particles Interacting with Cavity Resonances” to be submitted to *PRL* (2004).

Wang, J. “From DNA biosensors to gene chips” *Nucleic Acids Research* **28**, 3011-3016 (2000).

Walsh, M.K., Wang, X., Weimer, B.C. “Optimizing the immobilization of single-stranded DNA onto glass beads” *J.Biochem.Biophys.Methods* **47**, 221-231 (2001).

Watts, S.J., Yeung, D., Parkes, H. “Real-Time Detection and Quantification of DNA Hybridization by an Optical Biosensor” *Anal. Chem.* **67**, 4283-4289 (1995).

Weiss, D.S., Sandoghdar, V., Hare, J., Lefevre-Seguin, V., Raimond, J.M., Haroche, S. “Splitting of high Q Mie modes induced by light backscattering in silica microspheres” *Optics Letters* **20** (1995)

Yariv, A. “Optical Electronics in Modern Communications” New York, Oxford University Press, 1997.

Zako, T., Harada, K., Mannen, T., Yamaguchi, S., Kitayama, A., Ueda, H., Nagamune, T. “Monitoring of the Refolding Process for Immobilized Firefly Luciferase with a Biosensor Based on Surface Plasmon Resonance” *J.Biochem.* **129**, 1-4 (2001).

Zammatteo, N., Jeanmart, L., Hamels, S., Courtois, S., Louette, P., Hevesi, L., Remacle, J. “Comparison between Different Strategies of Covalent Attachment of DNA to Glass Surfaces to Build DNA Microarrays” *Analytical Biochemistry* **280**, 143-150 (2000).